



Modelling of Stable Tearing in Aircraft Structures

Q. Liu, P. Hamel, W. Hu, P.K. Sharp, A. Lahousse and G. Clark

Air Vehicles Division
Platforms Sciences Laboratory

DSTO-TR-1657

ABSTRACT

This report summarises the cooperative research program on stable tearing between DSTO and CEAT. The main objective was to study the conditions under which aircraft materials fracture by stable tearing and to develop a predictive capability for the process under operational conditions. The experiments on both CCT and CT specimens were to assist in validation of numerical modelling. Tear bands were successfully reproduced on CCT specimens with different specimen thickness by experiments at CEAT. The results were used to assess empirical models - Schijve's and Forsyth's models, and R-curve methods as well. Stable tearing feature was successfully simulated by a commercial finite element package ZENCRACK. Due to lack of local failure criteria, ZENCRACK cannot be used to predict whether stable tearing would occur or arrest under cyclic loading. But it appears to be useful for modeling such phenomena for indicative purpose only. A new 3D numerical model was proposed using a cohesive zone approach. This model can predict features similar to stable tearing and agrees well with the published experimental data. However, more research work needs to be done.

RELEASE LIMITATION

Approved for public release

Published by

*DSTO Platforms Sciences Laboratory
506 Lorimer St
Fishermans Bend, Victoria 3207 Australia*

*Telephone: (03) 9626 7000
Fax: (03) 9626 7999*

*© Commonwealth of Australia 2005
AR-013-350
March 2005*

APPROVED FOR PUBLIC RELEASE

Modelling of Stable Tearing in Aircraft Structures

Executive Summary

Fatigue crack growth in metallic structures remains one of the main threats to aircraft structural integrity, and is the subject of extensive research worldwide in an attempt to assess existing fatigue cracks, and predict their future growth under operational conditions. Most of this research has focussed on crack growth, which occurs at a rate of less than one micrometre for each application of loading. However, the prediction of such growth rates is often complicated by the presence of tearing fracture ("crack jumping" or "stable tearing"), in which cracks can extend by millimetres under the influence of a single high load. These tearing fracture bands are commonly seen on aircraft fracture surfaces.

This tearing fracture is caused by parts of the crack front becoming unstable, and advancing rapidly, thus changing the crack front shape. This change of shape can provide increased resistance to crack extension and in many cases can cause the crack to revert to the more usual slow fatigue growth. Therefore in order to improve aircraft structural integrity and safety it is important to develop an understanding of the stable tearing process, and to have access to useful engineering models which allow analysis and, if possible, prediction of the event. The process of stable tearing is a complicated phenomenon, which occurs during fatigue loading, and at present no fatigue crack growth models address the occurrence of tearing, despite the fact that it may make up half of the fracture surface.

DSTO and CEAT have been collaborating on a possible predictive capability for tearing, involving testing specimens to produce tearing, and assessing various models. This report presents the summary of the modelling and experimental work on stable tearing.

Experimental work at DSTO and CEAT has proven that the simple tearing models formulated by Schijve and Forsyth are good predictors of the stress intensity factor (SIF), which causes tearing. But both models are only valid for post fracture analysis as they rely on measurements taken from the fracture surface. R-curve analysis is an alternative, but relies on performing time-consuming R-curve tests using material of the appropriate thickness. The use of simple crack-front stress intensity analysis offers another possibility, and a simple approach based on elastic FEA is assessed against the experimental results.

Contents

1. INTRODUCTION	1
1.1 Background	1
1.2 Objectives of Collaborative Work	5
2. MATERIAL AND EXPERIMENTAL PROCEDURES.....	6
2.1 Material and Specimen Geometry.....	6
2.1.1 Materials	6
2.1.2 Test Specimen Geometry and Dimensions	7
2.2 Loading Conditions and Experimental Set-ups	9
2.2.1 Load Spectra for a CCT Specimen.....	9
2.2.2 Spectrum Loading for CT specimens	11
2.3 Observation of Fracture Morphologies	11
3. FRACTURE MORPHOLOGIES OF CCT AND CT SPECIMENS	11
3.1 CEAT Experimental Results	11
3.1.1 Under a Special Loading Spectrum	11
3.1.2 Under FALSTAFF Spectrum.....	12
3.2 DSTO Experimental Results (previous experience).....	13
4. INFLUENCE OF PARAMETERS ON STABLE TEARING	17
4.1 Influence of K_{max} on Δa	17
4.2 Influence of K_{eff} on Δa	19
5. INFLUENCE OF STABLE TEARING ON FATIGUE LIFE	21
6. R-CURVE, FORSYTH'S AND SCHIJVE'S MODELS	22
6.1 R-Curve Method.....	22
6.1.1 Procedure used for the Prediction of Tear Bands	24
6.1.2 Procedure for Calculation of Post Fracture Stress Intensity	24
6.1.3 Predicted Results	25
6.2 Forsyth and Schijve's Models.....	27
6.2.1 Forsyth's Model – A Geometrical Approach.....	27
6.2.2 Schijve's Model – A Fracture Mechanics Approach.....	28
6.3 Comparison of Forsyth's, Schijve's and R-curve results	30
7. A THREE-DIMENSIONAL FINITE ELEMENT MODEL USING ZENCRACK PACKAGE	32
7.1 ZENCRACK Package	32
7.1.1 Principle	32
7.1.2 Crack-Blocks.....	33
7.1.3 Procedure of ZENCRACK Modelling	35
7.2 Calculations of Stress Intensity Factors (SIFs)	36
7.2.1 Using ZENCRACK.....	36
7.2.2 Using ABAQUS Code	36
7.3 Fatigue Crack Growth in ZENCRACK	37
7.4 Modelling for Compact Tension (CT).....	39
7.5 Modelling for Centre-Cracked Tension (CCT)	40
7.6 A Curved Crack Tip Front.....	41

7.6.1	Definition of a Curved Crack Tip Front	41
7.6.2	Creation of a Curved Crack Tip Front.....	42
8.	A 3D FE MODEL USING COHESIVE ZONE APPROACH	43
8.1	Cohesive Zone Approach	44
8.1.1	Basic Principle	44
8.1.2	Mathematical Formulation.....	45
8.2	A Finite Element Model Using Cohesive Zone Approach.....	47
9.	RESULTS OF NUMERICAL ANALYSIS	50
9.1	Simulation of Stable Tearing by ZENCRACK.....	50
9.1.1	Basic Model	51
9.1.2	Simulations of Crack Profiles.....	52
	Fig. 9-3 Fatigue crack growth data for compact tension (CT) test specimen of 7050 Al	53
9.1.3	Simulation of Stable Tearing.....	55
9.2	Stress Distribution in a CT Specimen by ZENCRACK.....	56
9.2.1	A CT Specimen with 6 mm Thickness.....	57
9.2.2	A CT Specimen with 12 mm Thickness.....	57
9.2.3	A CT Specimen with 24 mm Thickness.....	59
9.3	Stress Distributions in a CCT Specimen by ZENCRACK.....	62
9.3.1	A CCT Specimen with 3 mm Thickness	62
9.3.2	A CCT Specimen with 6 mm Thick.....	63
9.3.3	A CCT Specimen with 9 mm Thickness.....	65
9.4	Effect of Crack Tip Front Shape by ZENCRACK.....	67
9.4.1	Under Elastic Condition	67
9.4.2	Under Elastic-Plastic Condition	71
9.5	Preliminary Numerical Results by CZM.....	72
10.	DISCUSSIONS	76
10.1	Simulation of Stable Tearing	76
10.2	Effect of Crack Front Shape	77
10.3	Stress Distributions Along Crack Tip Front.....	79
10.4	Applications of Cohesive Zone Model (CZM).....	79
10.5	Experiments from CCT Specimen Testing.....	79
11.	CONCLUDING REMARKS AND RECOMMENDATIONS	80
12.	ACKNOWLEDGMENTS	82
13.	REFERENCES.....	82

Nomenclature

a	- crack length
a_v	- averaged crack length
Δa	- change in crack length after tearing
B	- specimen thickness
C	- material constant
C_r	- crack curvature (percentage)
CCT	- centre-cracked tension
CT	- compact tension
CZM	- cohesive zone model
DSTO	- Defence Science and Technology Organisation
E	- Young's modulus
FE	- finite element
G	- energy release rate
h	- difference between surface crack and central crack heights
J	- J-integral
J_{Ic}	- critical value of J-integral
K	- stress intensity factor (SIF)
$K(a_{max})$	- maximum applied stress intensity
K_{Ic}	- plane strain fracture toughness
ΔK	- stress intensity factor range ($=K_{max} - K_{min}$)
m	- material constant
n	- material constant
R	- stress ratio (ratio of minimum to maximum applied stress)
SEM	- scanning electron microscope
SEN	- single edge notched
t	- work-conjugate effective traction in CZM
V	- crack opening displacement
α	- constant: 1 for plane strain and 0 for plane stress
β	- material parameter: $1-\nu^2$ for plane strain and 1 for plane stress
δ	- displacement jump across the cohesive surface
δ_{Ic}	- critical value of crack opening displacement
Γ_c	- cohesive energy
θ	- angle subtended between the tear band and specimen surface
σ_{coh}	- cohesive strength ($= 3\sigma_y$)
σ_y	- yield strength
σ_{max}	- maximum applied stress
ν	- Poisson's ratio
da/dN	- fatigue crack growth rate

1. Introduction

Fatigue crack growth in metallic structure remains the principal threat to aircraft structural integrity, and is the subject of extensive research worldwide in an attempt to assess existing fatigue cracks, and predict their growth under operational conditions. Most of this research has focused on crack growth, which occurs at a rate of less than one micrometre per loading cycle. However, the prediction of such growth rates is often complicated by the presence of stable tearing fracture (sometimes called “crack jumping”) in which cracks can extend by millimetres under the application of a single high load. This tearing fracture is caused by the loss of stability in crack growth on portions of the crack front. The rapid crack growth on these portions then lead to a change in the shape of crack front. This change in shape in turn provides increased resistance to further crack extension. The main feature of stable tearing is that the loss of local stability interacts with change of the shape of crack front, leading to regaining local stability.

1.1 Background

Stable tearing during fatigue crack growth has been observed in a number of aircraft structures involving aluminium as well as steel. This problem was highlighted during a detailed investigation of fatigue failure in the main spar of an AerMacchi trainer which lost a wing during flight in 1990, as reported in (Barter, et al, 1991; Goldsmith, et al, 1996; Athiniotis, et al, 1999). An example of a fracture surface with substantial stable tearing is shown in Fig.1-1, where the crack initiated from the bottom of one of the forward-flange fastener holes. The fractography of the fractured lower spar boom showed multiple tear bands associated with the fatigue crack growth into the thick section of the spar boom, presumably because of the periodic high tensile overloads in the spectrum.

Each of these bands occurs as a result of a single high load application, and represents a sudden extension of the crack, as shown in Fig.1-2. The crack extends more in the central region of the specimen than at the edges, so there is a marked shape change during the formation of the band; this shape change is associated with a change in the stress distribution at the crack tip. After the tear, the crack will usually continue to grow by fatigue, followed by more stable tearing and fatigue. When the crack reaches a critical length, a tear occurs which grows in a globally *unstable* manner to failure.

Substantial tearing is observed in many of the fatigue fractures examined at Defence Science Technology and Organisation (DSTO) in Australia, including those in thick sections where low toughness is normally observed, for example, in the Macchi wing spar (Fig. 1-1). Examples from Royal Australian Air Force (RAAF) aircraft include the teardown of F-111 longerons and fatigue-tested F/A-18 bulkheads. In these cases, the fracture surfaces were being assessed to determine the growth rate of the fatigue crack, and the presence of the tearing made the assessment particularly complicated. The

experimental results show that stable tearing certainly influences the fatigue life because it changes crack front shape and increases crack length.



Fig. 1-1 *Fracture surface of a failed Macchi MB326H wing spar showing alternating bands of fatigue and tearing. The tear bands are the darker grey areas, which occur within a single fatigue cycle and fatigue (light grey) (Barter, et al, 1991).*

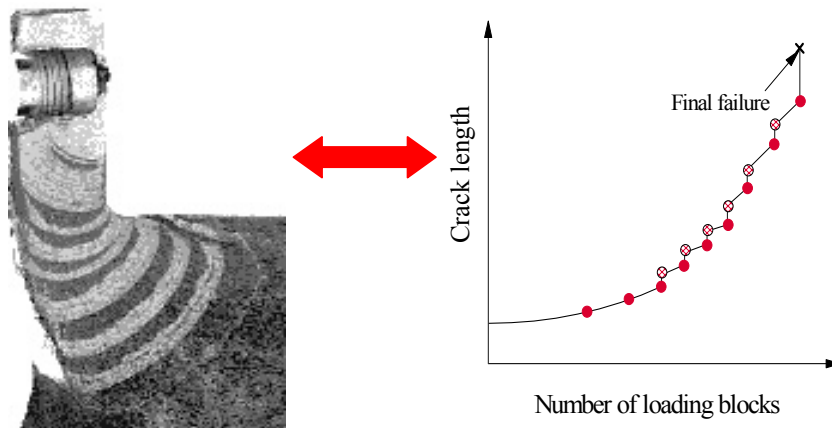


Fig.1-2 *Tear bands in the failed Macchi MB326H wing spar and corresponding crack growth as a function of number of loading blocks.*

One particular example which led to heightened interest was the observation of tearing in a high strength steel component from an F-111 aircraft; this low-toughness material would not normally be expected to show much stable tearing, but an example was seen where tearing occurred with the fatigue crack at only one-third of its final service depth. Fig.1-3 shows an example with larger tear bands from a D6ac coupon test.

Taking the conventional view that tearing in low-toughness materials is a sign of near-failure would imply that the aircraft had experienced a near-critical loading condition when the crack was at that point (a surprising result, since it suggests that a similar load that occurs at any time after the tear would cause failure, i.e. the safety of the aircraft was in doubt). An alternative explanation is that the local tearing may occur at much lower stress intensities than normally expected for this relatively brittle material. For example, in a longeron of F-111, clear tear bands were observed from the fracture surface, as shown in Fig.1-4. Examples of tear bands were also observed on the fracture surface of the upper duct flange in an F/A-18 bulkhead, see Fig.1-5. Similar stable tearing was also found in the wing panel of TRANSALL in France, as shown in Fig.1-6.

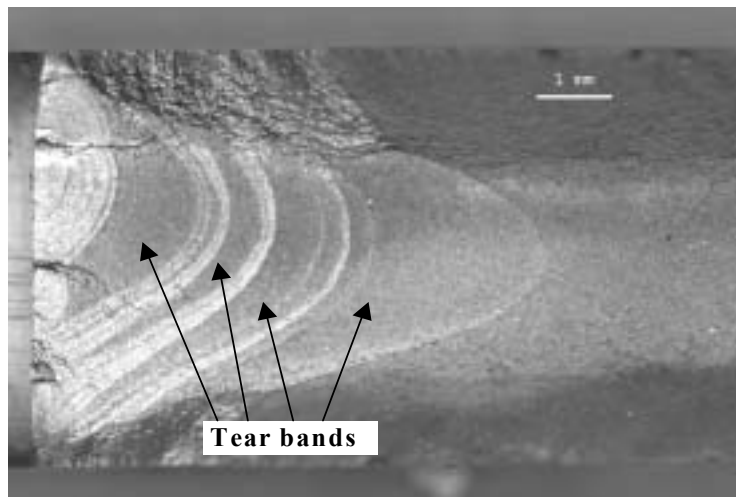


Fig.1-3 Large tear bands (darker grey areas-indicated by arrows) from a fracture surface of a D6ac steel coupon test, which is a material used in F-111.

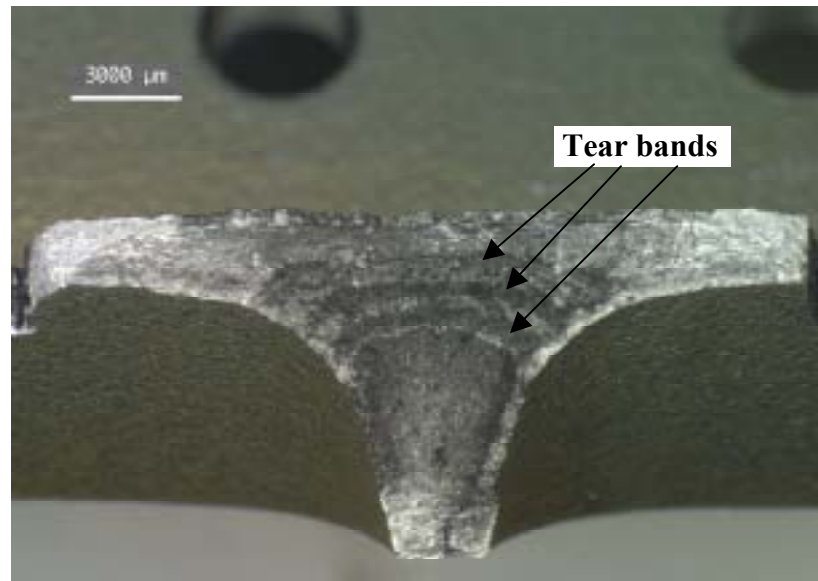


Fig.1-4 Fracture surface of longeron (left-hand side-LHS) in F-111 showing several tear bands.

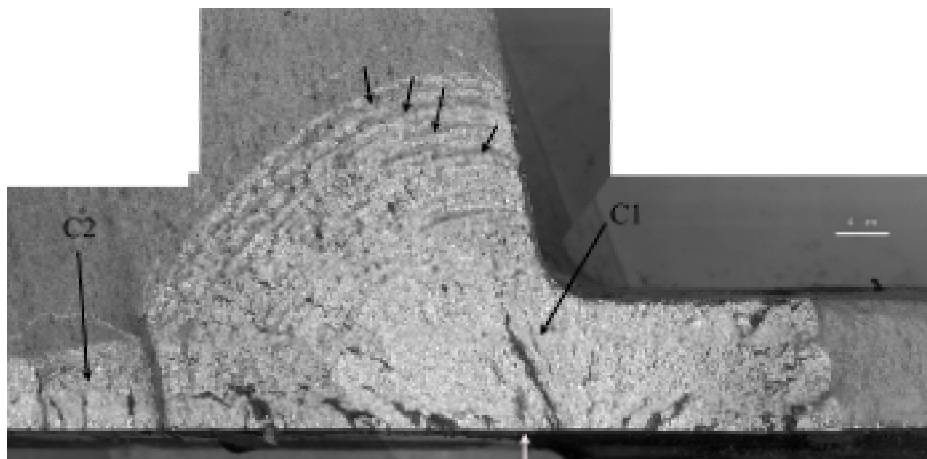


Fig.1-5 Fracture surface of the upper duct flange (right-hand side-RHS) in an F/A-18 bulkhead showing several tear bands (indicated by black arrows) and the crack origin was indicated by a white arrow at the bottom.

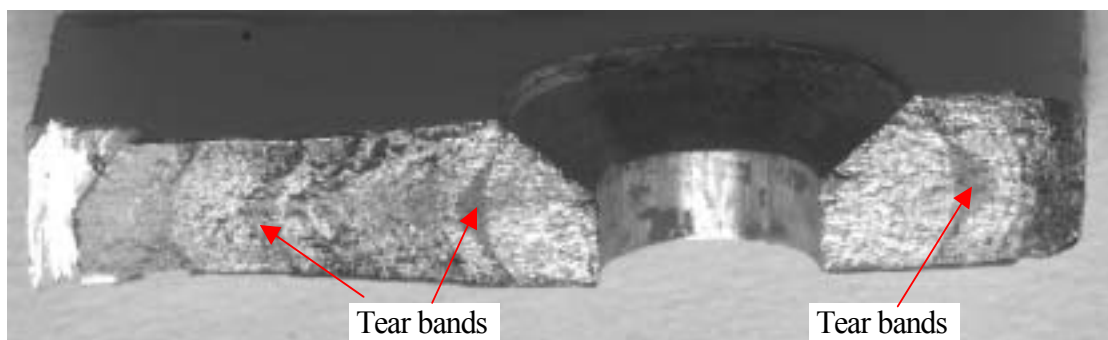


Fig.1-6 Fracture surface of a cracked part of the wing panel of TRANSALL showing the tear bands.

The existence of intermittent tearing fracture has significant implications for the management of components through the methodology of durability and damage tolerance, as unexpected failure may arise due to the occurrence of a single excessive load. Most currently available crack growth models are based on the concept of damage accumulation, represented through the crack growth curve. For a given stress intensity range, if the fatigue load is applied by dN cycles, the crack is assumed to grow by a length of da . This idea is closely related to the traditional strain-life approach, as demonstrated by Fühling and Seeger (1979). Within the framework of such models, tearing fracture cannot be allowed: if the stress intensity reaches the critical value, then the specimen would be considered to have failed, whereas the experimental evidence shows that even after the first occurrence of tear fracture the material may still be able to sustain a considerable amount of service life. Clearly, disallowing stable tearing would lead to overly conservative prediction, but whether this potential can be safely exploited depends on how well we understand the conditions under which stable tearing occurs and how accurately we can predict it. It is therefore of practical importance to investigate stable tearing in fatigue crack growth using experimental and numerical methods.

1.2 Objectives of Collaborative Work

As mentioned above, under some circumstances a stable tearing could occur, leading to increase the length of the crack well beyond that which would be normally predicted. This behaviour is obviously a major issue that needs to be understood and quantified. Therefore, a cooperative research program was established between Defence Science and Technology Organisation (DSTO) in Australia and Aeronautical Testing Centre (CEAT) in France. The main objective of this program was to study the conditions under which aircraft materials fracture by stable tearing and to develop a predictive capability for the process under operational conditions. Further testing and analysis were proposed to assist in development of that capability.

In Phase I of the research program, two Work Packages (WPs) were planned:

(1) WP1: Study of stable tearing under controlled laboratory conditions

- Study stable tearing under controlled laboratory conditions using different specimen geometry to that previously tested at DSTO (e.g. compact tension-CT specimen). The proposed geometry was centre-cracked tension (CCT) specimens, which were tested in CEAT.
- Identify a suitable alloy for fatigue testing. DSTO recommended aluminium alloy 7050, as this alloy has wide application in modern military aircraft such as F/A-18. Fatigue tests were conducted on CCT specimens using constant amplitude loading, with occasional overloads to generate stable tearing. The aim was to produce a tear band, which starts naturally under the high load and progresses significantly before arresting.

(2) WP 2: Model of stable tearing using incremental crack growth/finite element (FE) models

- Assess a FE model (using software packages such as Zencrack and BEASY) to establish a capability to “grow” crack fronts, making allowances for the plane stress/plane strain differences along the front.
- Use the results from WP1 (in particular crack front shape and position just prior to the commencement of stable tearing), attempt to predict the extent of crack front shape change and growth during the tearing using the FE model.
- By comparing the prediction with experimental data, plane stress growth correction factors were investigated to provide empirical corrections, and to improve the correlation.
- The applicability of predictive modelling to specimens tested under a fighter aircraft load sequence will be assessed.

In this joint technical report, all the experimental and modelling work is summarised. Additionally, recommendations for future, for example, Phase II, work are made.

2. Material and Experimental Procedures

2.1 Material and Specimen Geometry

2.1.1 Materials

Three types of materials used for the experimental testing were 7050-T7451 (new), 7050-T73651 (old) and 7075-T6 aluminium alloys. The new 7050 (i.e. 7050-T7451) Al

alloy, which was a 150 mm thick plate, was used for manufacturing both CCT and CT specimens. The old 7050 (i.e. 7050-T73651) Al alloy, which was 12.5 mm thick, was used for CT specimens only. The 7075-T6 aluminium alloy was used for verification of both Schijve and Forsyth's empirical models. Their chemical compositions and mechanical properties are presented in Tables 2-1 and 2-2, respectively.

Table 2-1 Chemical composition of 7050 and 7075 aluminium alloys in weight percent (ASM, 2002; MIL-HDBK-5J, 2003)

Materials	Al	Cu	Mn	Si	Mg	Zn	Cr	Fe	Ti	Zr
7050-T7451	Bal	1.9-2.5	Max 0.1	Max 0.12	2.0 - 2.7	5.6 - 6.9	Max 0.04	Max 0.15	Max 0.06	0.08-0.15
7075-T6	Bal	1.50	0.30	0.08	2.55	5.65	0.2	0.50	0.06	-

Table 2-2 Mechanical properties of 7050 and 7075 aluminium alloys (ASM, 2002; MIL-HDBK-5J, 2003)

Material	Yield stress ¹ (MPa)	Tensile Stress (MPa)	Young's Modulus (GPa)	Fracture Toughness ² (MPa-m ^{1/2})	Elongation (%)	Poisson ratio
7050-T7451 (7050-T73651)	413	482	72.0	32	11	0.33
7075-T6	476	538	72.0	29	11	0.33

¹ the yield stress is $\sigma_{0.2}$.

² Fracture toughness (K_{IC}) is in L-T direction.

2.1.2 Test Specimen Geometry and Dimensions

In this program, two types of fatigue test specimens were used: (a) CCT specimen and (2) CT specimen. The former was tested by CEAT while the latter was tested by DSTO. The geometry and dimensions of both types of specimens are shown in Fig.2-1 and Fig.2-2, respectively.

Three thicknesses (B), i.e., 3, 6 and 9 mm, were selected for CCT specimens. A small hole with a diameter of 3 mm was drilled in the centre of the CCT specimen (Fig.2-1). A crack was generated from an initial electric discharge machined (EDM) notch, in accordance with ASTM Standard E399-90. Fracture toughness measurements were carried out for all three thicknesses according to the standard. A total of 30 specimens were machined from a 150 mm thick sheet. An anti-buckling system was used for the 3 mm thickness specimens. Three thicknesses (B), i.e., 6, 12 and 24 mm, were used for CT specimens. The width of the CT specimens (W) was 50.8 mm.

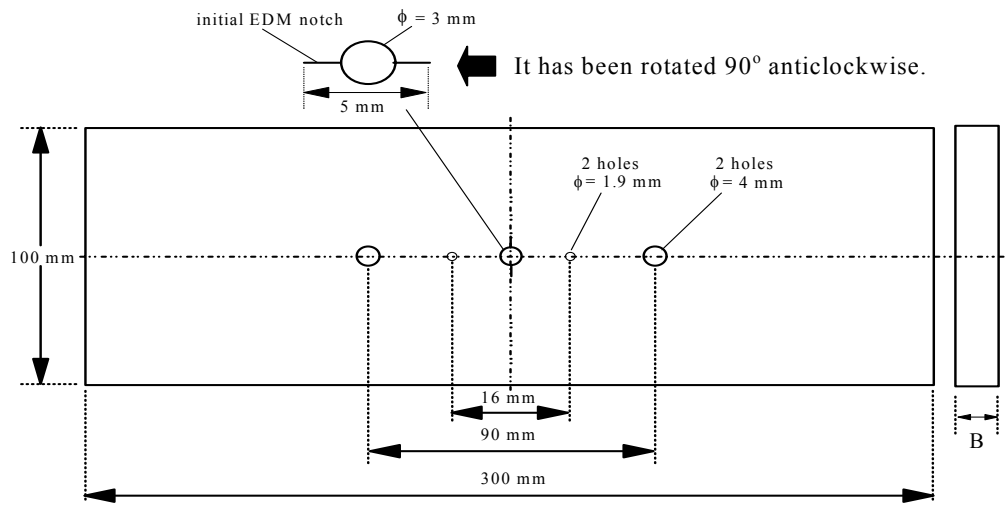


Fig. 2-1 Dimensions of CCT specimen for experiments and FE Modelling (not to scale), where the specimen thickness varies from 3 to 9 mm.

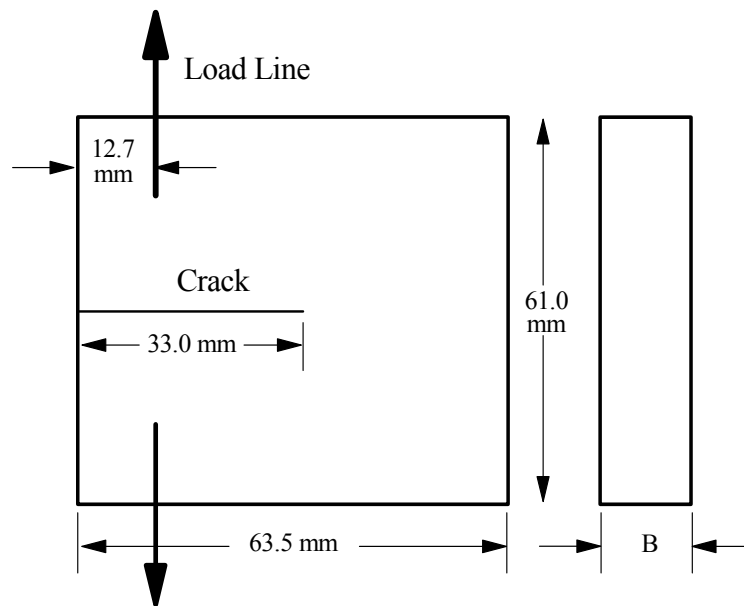


Fig. 2-2 Dimensions of CT specimen for FE Modelling (not to scale), where the specimen thickness varies from 6 to 24 mm.

2.2 Loading Conditions and Experimental Set-ups

2.2.1 Load Spectra for a CCT Specimen

In order to study their effects on stable tearing, the following parameters have been modified during the test campaign:

- The amplitude of the background fatigue spectra.
- The load control: displacement- or load-controlled.
- The loading rate during the overload (0.001, 0.1, 1 mm/minute and 2000 daN¹/min).
- The tear threshold, Δa , which triggers the end of the overload.

The experimental set-up for fatigue testing of the CCT specimens is shown in Fig.2-3. In order to easily obtain exploitable stable tearing bands, CEAT developed a special loading sequence, as shown in Fig.2-4. A background fatigue load of constant amplitude fatigue at a ratio R of 0.1 was applied, with periodic overloads at given crack lengths to produce the tearing. The amplitude of the constant amplitude load was chosen to reduce the time required for the crack to go through the plastic zone generated by the overload. The constant amplitude load was stopped once the crack propagated outside the theoretical plastic zone, to assure the separation between two successive tearing bands. The overload was applied, as in a static test, with a controlled displacement rate and was automatically stopped after a programmed variation of the crack length (measured via the potential method). 17 CCT specimens were tested using this load spectrum.

Additionally, in order to produce tearing bands in a more realistic way, six fatigue tests of CCT specimens (two for each thickness) were conducted under FALSTAFF spectra with different amplitudes.

¹ 2000 daN/min is the loading rate when the overload is applied (load-controlled mode).

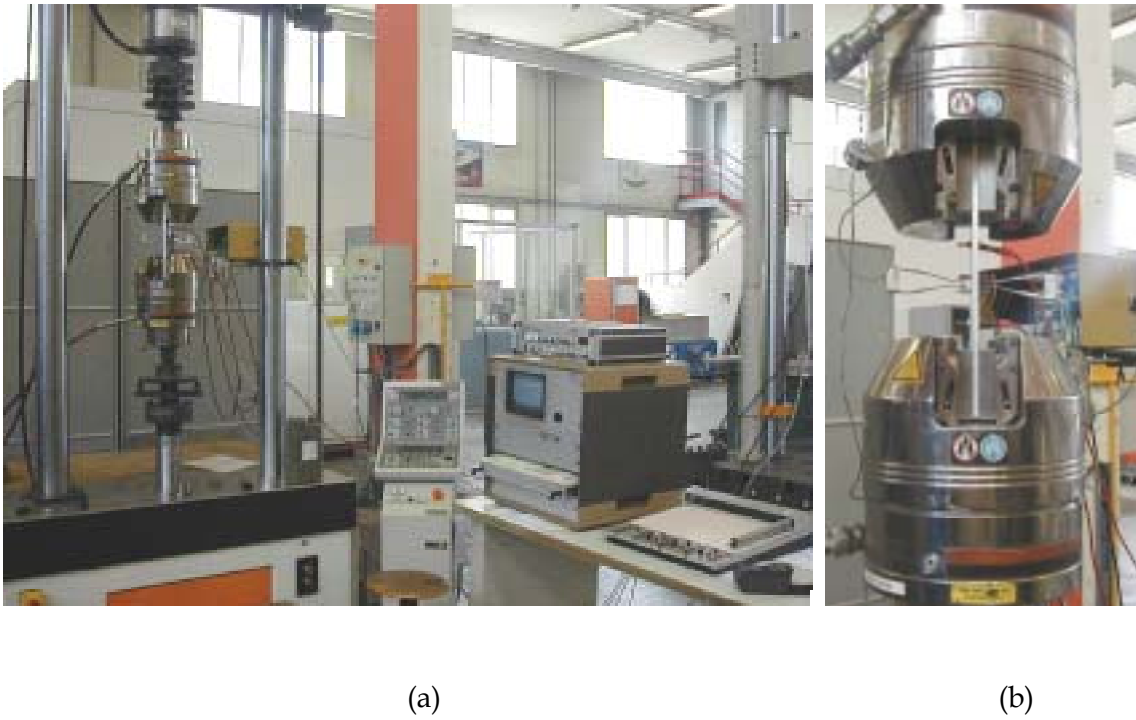


Fig. 2-3 (a) photographs of whole experimental set-up and (b) enlargement of the loading arrangement with a specimen inserted.

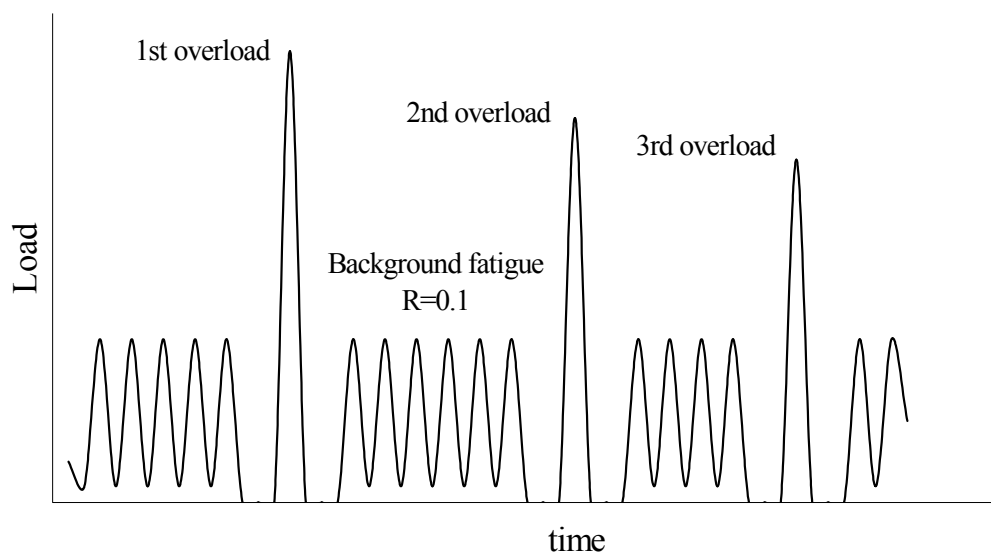


Fig. 2-4 Schematic of the loading sequence used for CCT specimens.

2.2.2 Spectrum Loading for CT specimens

The tearing experiments on CT specimens were carried out at DSTO in a computer-controlled servo-hydraulic Instron fatigue test machine using a 25kN load cell. A background of constant amplitude fatigue load at a stress ratio (R) of 0.1 was applied with periodic overloads at a set of crack lengths to produce tearing, as illustrated schematically in Fig.2-5. Some of the older 7050 specimens were tested with a constant background ΔK (of around $22.5 \text{ MPa}\sqrt{\text{m}}$), with appropriate periodic overloads. The details can be seen in a DSTO report (Byrnes, et al., 2000).

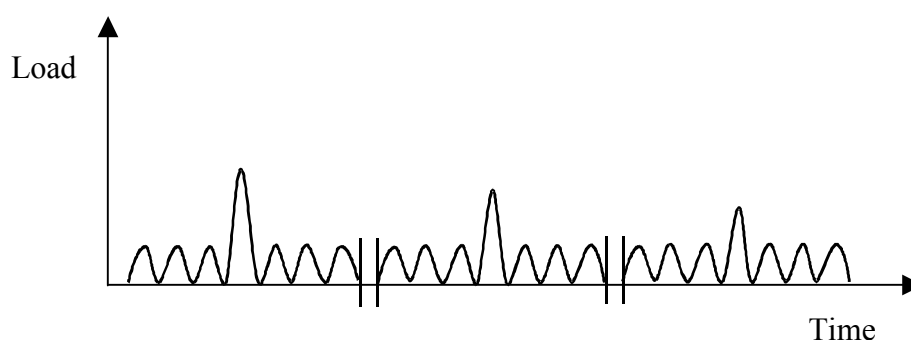


Fig.2-5 Schematic of the loading sequence used in the tearing tests of CT specimens (DSTO).

2.3 Observation of Fracture Morphologies

In order to further understand the behaviour of tear bands, a series of examinations on fracture surfaces were performed on selected CCT specimens. The fracture morphologies on CCT were observed by an optical microscope (Polyvar) with a digital image capturing system.

3. Fracture Morphologies of CCT and CT Specimens

3.1 CEAT Experimental Results

3.1.1 Under a Special Loading Spectrum

A total of 17 CCT specimens were tested with 11 of them successfully producing tear bands and the remaining 6 broke at the first overload. Some fracture surfaces are shown in Fig.3-1, where the dark area represents the tear bands and light zone represents fatigue crack growth. A total of 98 tear bands were measured to get the data for modelling.

From Fig. 3-1, it can be seen that multiple tear bands were successfully produced. It can be seen that the width of the tear bands depends on the specimen thickness. With increasing specimen thickness, the average width of the tear bands also increased and the size of the fatigue zone between adjacent tear bands became smaller.

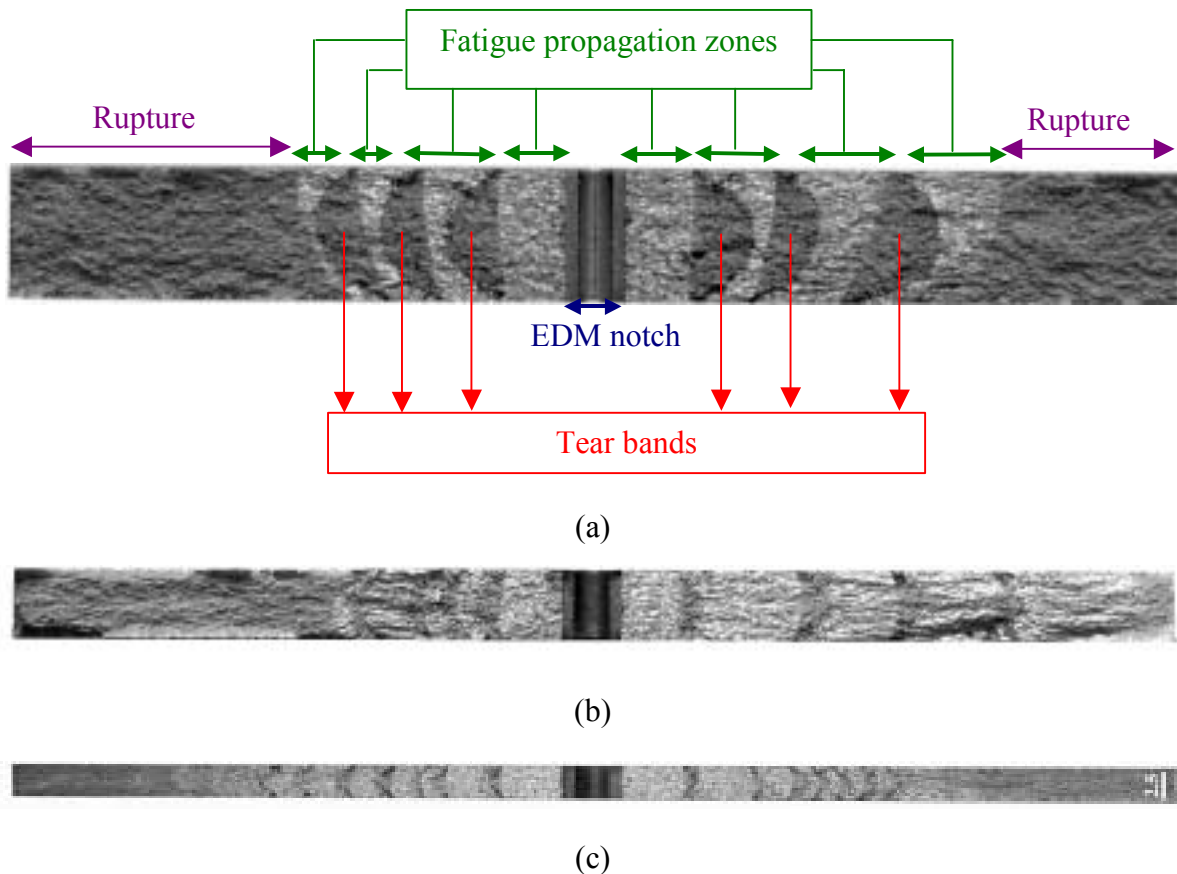


Fig. 3-1 Micrographs of CCT specimens showing large tear bands (darker bands) on fracture surface. (a) $t = 9 \text{ mm}$ (KWST-96); (b) $t = 6 \text{ mm}$ (KWST-66) and (c) $t = 3 \text{ mm}$ (KWST-34), where 2.5mm is the scale marker shown at the right hand end of the photograph.

3.1.2 Under FALSTAFF Spectrum

The FALSTAFF spectrum (Fighter Aircraft Loading STandard For Fatigue evaluation) represents 200 flight hours. It was truncated at $0.145g^2$ to avoid the destruction of the fracture surfaces by compression.

² Gravitational acceleration (9.81 m/s^2)

A total of six fatigue tests were conducted on CCT specimens (two specimens for each thickness) under FALSTAFF spectrum. After the first tests (1 of each thickness), the maximum load amplitude was modified for the 3 and 6 mm thick specimens to increase the length of the fracture surfaces except for the two 9 mm thick specimens. An example of a fracture surface from the 9 mm thick CCT specimen is shown in Fig. 3-2. A total of 128 tear bands were measured, but they were not successfully correlated to the loading sequence. Consequently, these data were not used in the modelling study at CEAT.

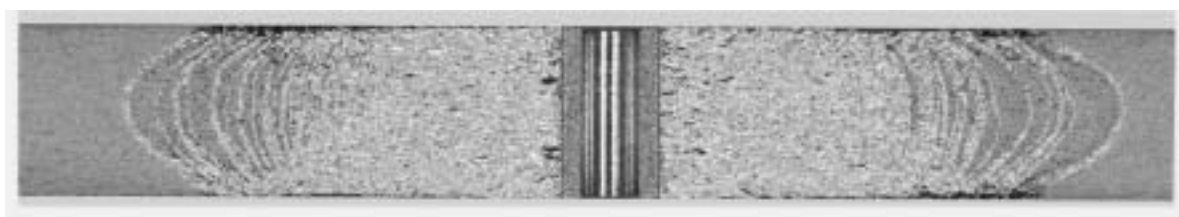
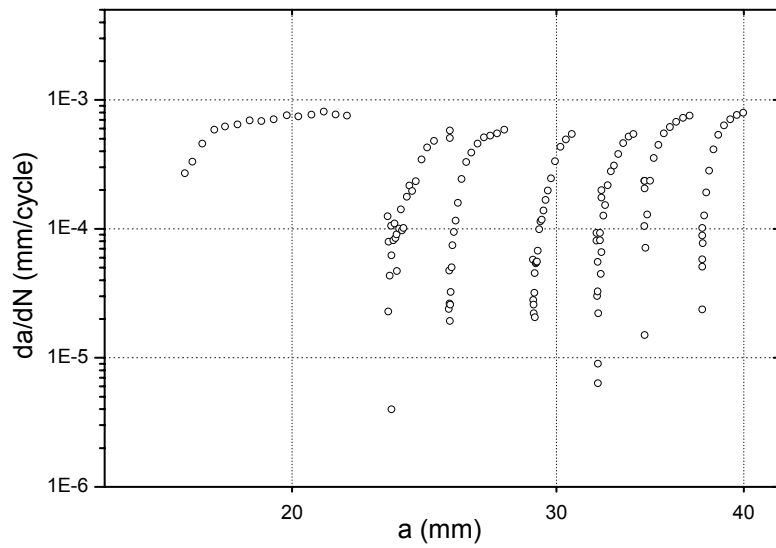


Fig. 3-2 Micrograph showing tear bands in a CCT specimen with $t = 9$ mm (KWST-92) under the FALSTAFF spectrum.

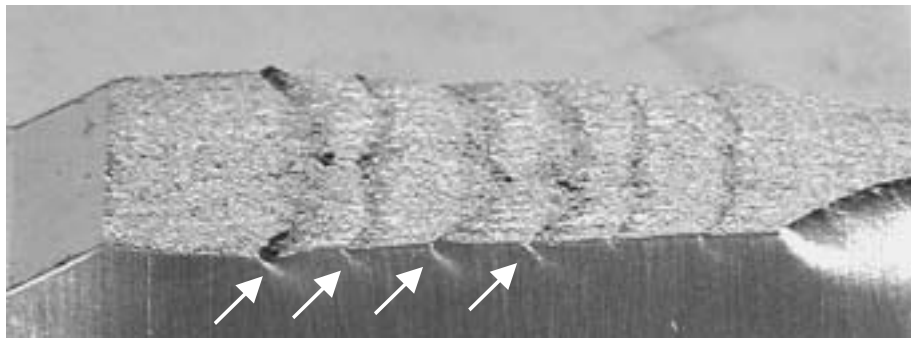
3.2 DSTO Experimental Results (previous experience)

As indicated in Sec.2.2.2, a background of constant amplitude fatigue load at a stress ratio (R) of 0.1 was applied with periodic overloads at set crack lengths to produce tearing, see Fig.2-5. After each overload, a significant plastic deformation was generated, which in turn produced a compressive residual stress field around the crack tip. This residual stress field temporarily reduces the crack growth rate, and acts as a shield to further growth. In order to maintain a reasonable growth rate, the background loading was raised for a short time. It turned the initial level after approximately 0.5 mm of crack growth. The crack was then grown for approximately 5 mm at the initial load level. This retardation of crack growth is illustrated for specimen No 50-86 in Fig.3-3 (a), while Fig. 3-3 (b) shows the deformation observed on the specimen surface due to the applied overloads.

DSTO successfully reproduced the tear bands on laboratory coupons with different thicknesses using CT geometry (Byrnes, et al, 2000). Table 3-1 is a summary of the conditions and overloads applied to each specimen and Fig. 3-4 shows the resulting fracture surfaces and tear bands for different thickness specimens. Clearly, each specimen had multiple tear bands with each successive tear band, except for KSIE12-10 specimen. The single tear band produced on KSIE12-10 extended out of the plane of fracture and the specimen nearly failed catastrophically. Specimen 50-126 was sourced from the older T73651 plate while the KSIE specimens were all sourced from the newer T7451 material. The experimental results also show that the crack front becomes more curved after multiple tear bands (Fig.3-4).



(a)



(b)

Fig.3-3 (a) Crack growth retardation in specimen No 50-86 and (b) deformation on surface resulting from applied overloads (arrowed).

KSIE24-1 and KSIE24-2 were 24 mm thick specimens from the 7050-T7351, while specimen 75-141 was a 25 mm thick specimen of 7075-T6. In each case a background constant amplitude fatigue loading of 0.9 to 9.0 kN was used with overloads applied at stress intensity levels approximately equal to K_{Ic} . Specimens, KSIE24-1 and 24-2 failed catastrophically. With specimen 75-141, three very narrow “tear bands” were produced at stress intensities of 31 $\text{MPa}\sqrt{\text{m}}$, but at 32 $\text{MPa}\sqrt{\text{m}}$ the specimen failed catastrophically. Table 3-2 is a summary of the loading conditions for these specimens while Fig. 3-5 shows the fracture surfaces of specimens KSIE24-2 and 75-141.

Table 3-1 Summary of loading conditions applied to specimens 50-126, KSIE12-1, KSIE6-6, KSIE6-5 and KSIE12-10

		Specimens				
		50-126	KSIE12-1	KSIE6-6	KSIE6-5	KSIE12-10
Thickness, t		12.5 mm	12 mm	6 mm	6 mm	12 mm
Background (R=0.1)		Constant $\Delta K=22.5$ MPa \sqrt{m}	Constant $\Delta P=4.5$ kN	Constant $\Delta P=1.8$ kN	Constant $\Delta P=1.8$ kN	Constant $\Delta P=4.5$ kN
Overload	1	16.7 kN @ a=20.7 mm	15.07 kN @ a=22.2 mm	7.52 kN @ a=21.8 mm	8.52 kN @ a=20.9 mm	15.45 kN @ a=21.9 mm
	2	13.32 kN @ a=24.0 mm	11.29 kN @ a=26.9 mm	5.77 kN @ a=26.4 mm	6.90 kN @ a=24.7 mm	-
	3	11.14 kN @ a=27.1 mm	8.17 kN @ a=31.1 mm	4.31 kN @ a=30.8 mm	5.58 kN @ a=27.9 mm	-
	4	8.56 kN @ a=30.3 mm	-	-	4.38 kN @ a=30.8 mm	-

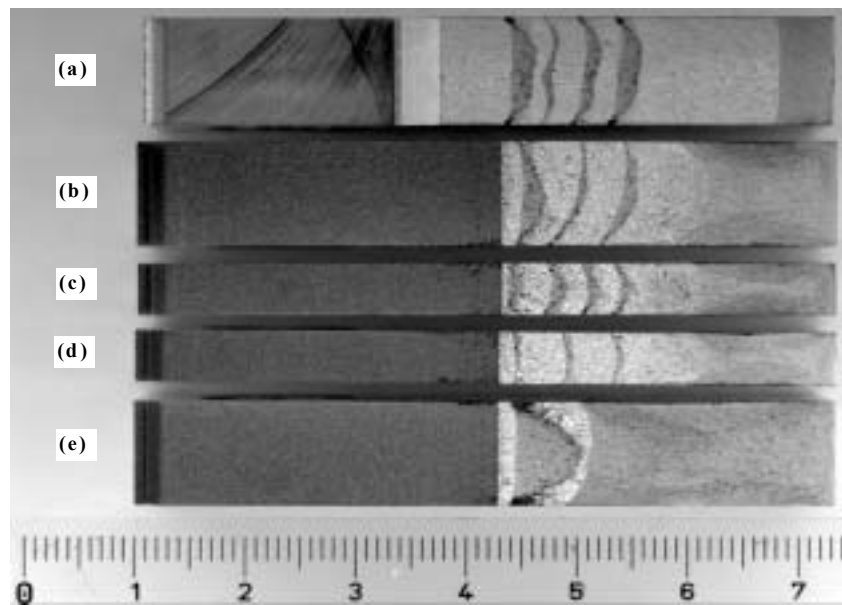


Fig. 3-4 Micrograph showing stable tearing features (dark bands). (a) $t = 12$ mm (Specimen: 50-126); (b) $t = 12$ mm (KSIE12-1); (c) $t = 6$ mm (KSIE6-6), (d) $t = 6$ mm (KSIE6-5) and (e) $t = 12$ mm (KSIE12-10).

From the laboratory tests, it is clear that the tear bands are caused by parts of the crack front becoming unstable, and advancing rapidly, thus changing the crack front shape. This change of shape can provide increasing resistance to the crack extension, and in many cases can cause the crack to revert to the more usual slow fatigue growth. The DSTO experimental results have proven that the empirical tearing models formulated

by Forsyth (1976, 1981) and Schijve (1979) are good predictors of the stress intensity, which causes tearing (Byrnes, et al., 2000). But both Schijve and Forsyth's models are only valid at the post fracture analysis since measurements of the various shapes of the crack front are required. Both models were also applied to the CCT specimens. The details can be seen in Chapter 6.

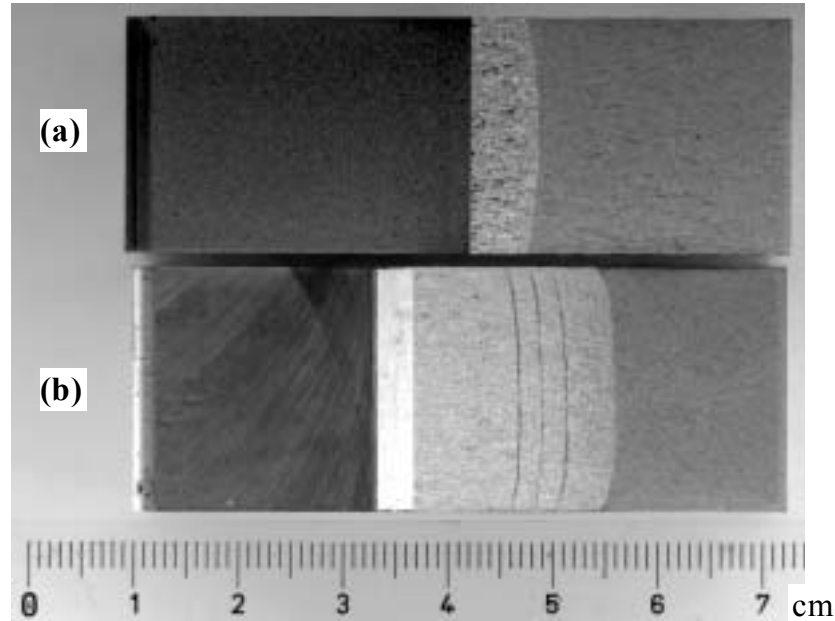


Fig.3-5 Micrographs showing stable tearing features on specimens. (a) KSIE24-2 and (b) 75-141. Both specimens failed catastrophically at a stress intensity factor approximately equal to K_{Ic} , with little or no tear band formation.

Table 3-2: Summary of loading conditions applied to specimens 75-141, KSIE24-1 and KSIE24-2

		Specimens		
		75-141	KSIE24-1	KSIE24-2
Thickness, t		25 mm	24 mm	24 mm
Background (R=0.1)		Constant $\Delta P=7.2$ kN	Constant $\Delta P=8.1$ kN	Constant $\Delta P=7.2$ kN
Overload	1	17.34 kN@ a=24.89 mm	21.91 kN@ a=26.91 mm	24.33 kN@ a=26.99 mm
	2	15.26 kN@ a=26.89 mm	-	-
	3	13.43 kN@ a=28.72 mm	-	-
	4	11.19 kN@ a=31.05 mm	-	-

4. Influence of Parameters on Stable Tearing

As seen in Sec.3.1, several testing parameters have been modified with the aim of studying their influence on stable tearing. The main parameters studied were the stress intensity factor at the maximum load of the overload, K_{\max} , and the effective stress intensity factor, K_{eff} (or $\Delta K_{\text{eff}} = K_{\max} - K_{\text{op}}$), for CCT specimens (see Fig.4-1). K_{op} is the SIF at crack tip opening or closure. K_{sp} is the SIF at the maximum load of the constant background fatigue load and the crack length preceding the overload. Assume K_{sp} is equal to the K opening (K_{op}) of the overload. K_{\min} is the SIF at the minimum load. Assume K_{\min} is equal to zero at the beginning of the overload, i.e., $K_{\min} = 0$, then $\Delta K = K_{\max}$.

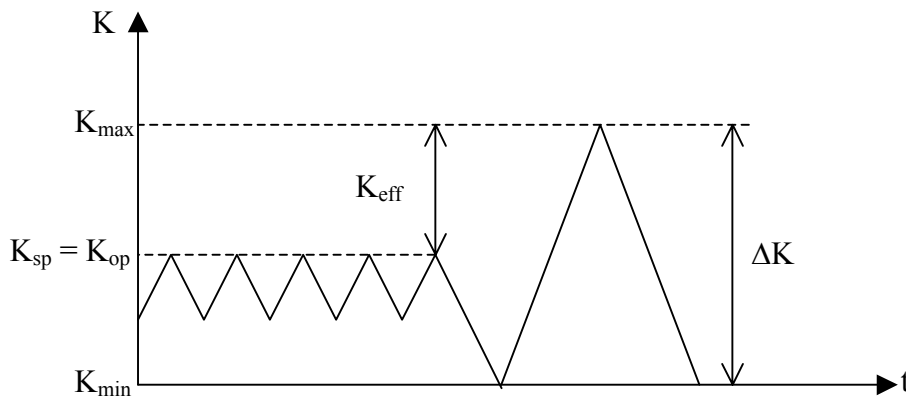


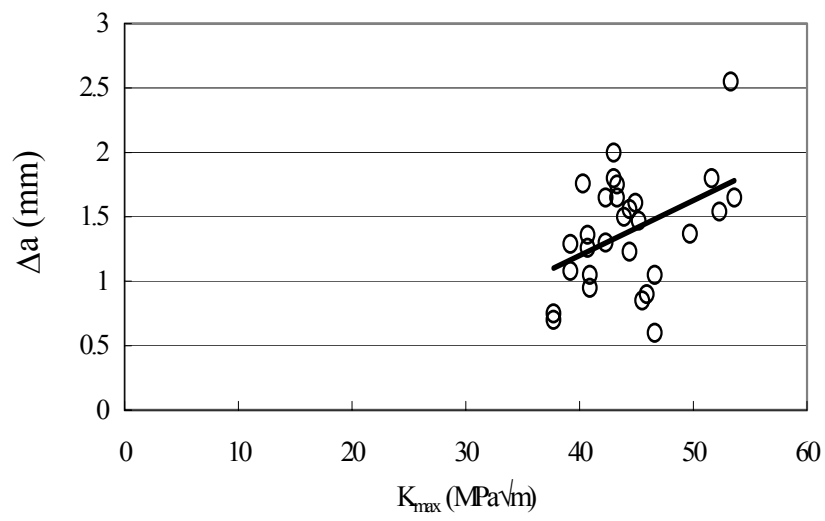
Fig. 4-1 Definition of the parameters studied for an overload.

4.1 Influence of K_{\max} on Δa

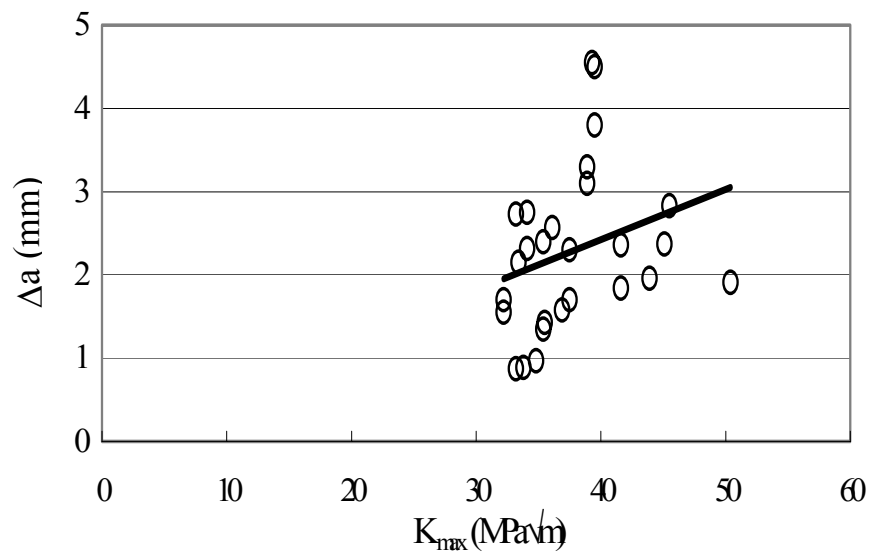
The plots of the fatigue crack extension (Δa) versus the maximum stress intensity factor (K_{\max}) for each thickness are shown in Fig.4-2. Each plot represents a tear band. Only 85 tear bands (among 98), with a distance³ of at least $2r_y = \frac{1}{\pi} \left(\frac{K}{\sigma_{0.2}} \right)^2$, have been selected⁴. The least square line has also been drawn.

³ Separation width between adjacent tear bands.

⁴ This is the plane stress plastic zone size. If the plane strain plastic zone size was used then more bands would qualify.



(a)



(b)

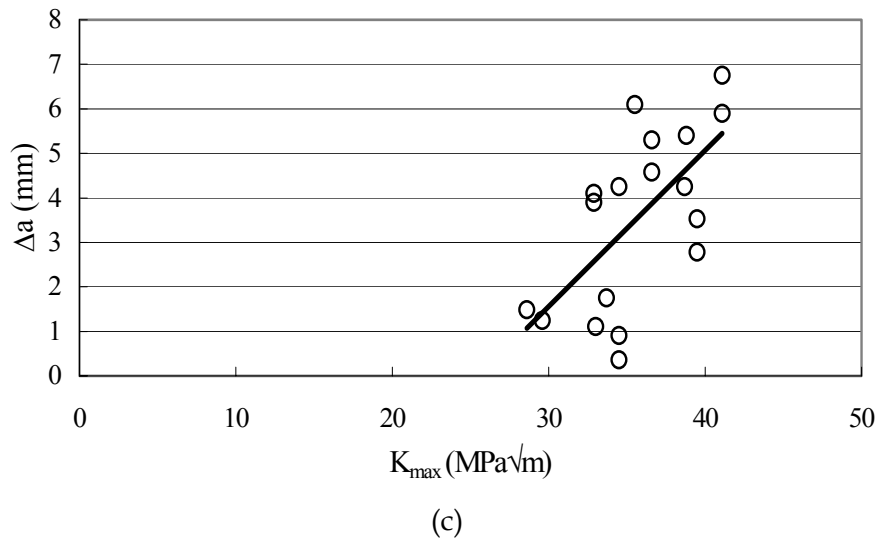
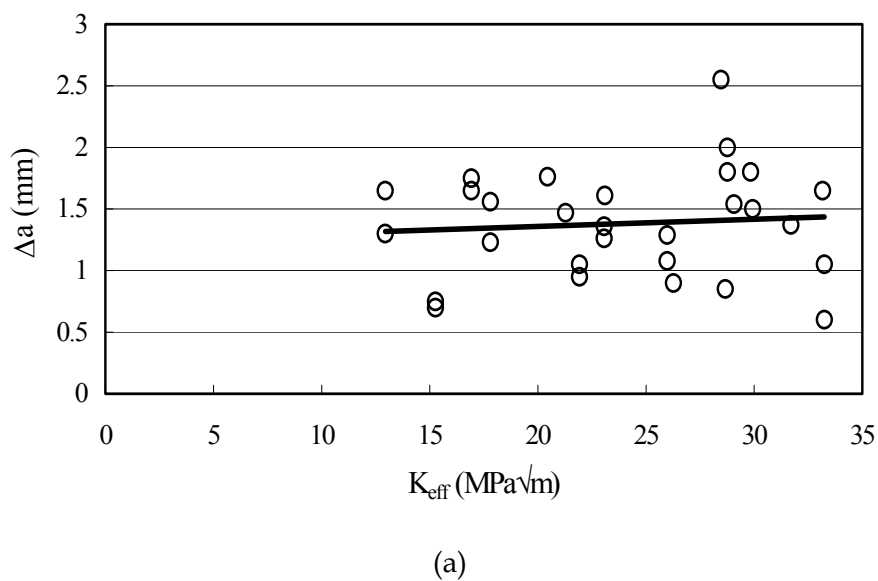
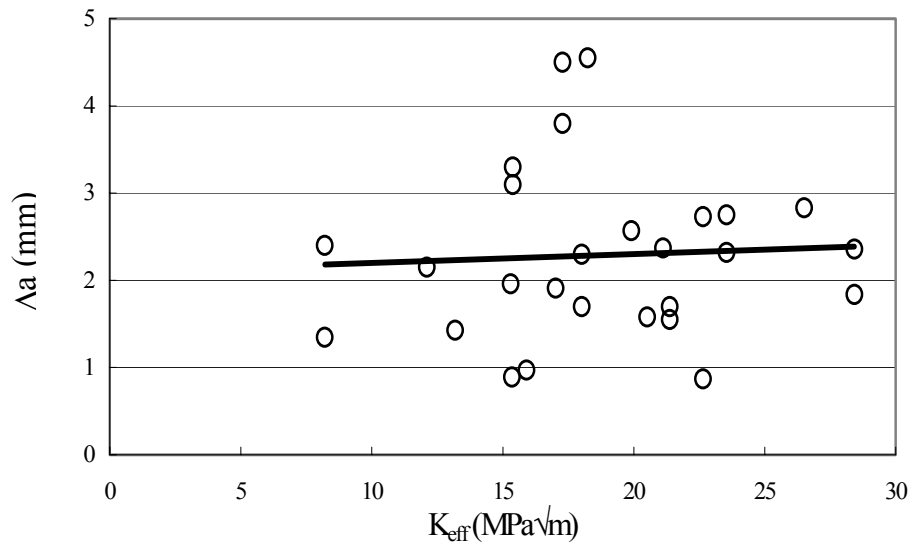


Fig. 4-2 Plots of fatigue crack extension (Δa) as a function of maximum intensity factor (K_{max}) for different thickness CCT specimens. (a) 3 mm; (b) 6 mm and (c) 9 mm.

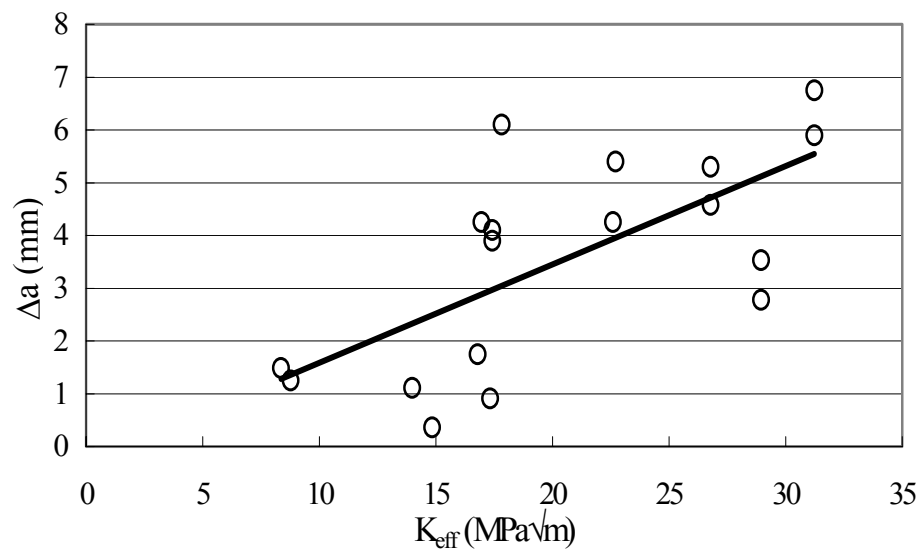
4.2 Influence of K_{eff} on Δa

The plots of the fatigue crack extension (Δa) versus the effective stress intensity factor (K_{eff}) for each thickness are shown in Fig.4-3. Assuming the stress intensity factor (SIF) at the crack tip opening K_{op} is equal to the SIF at the small peak load, K_{sp} , (refer to Fig.4-1). From the results, it can be seen that no obvious correlation can be found between Δa and K_{eff} .





(b)



(c)

Fig. 4-3 Fatigue crack extension (Δa) as a function of effective stress intensity factor (K_{eff}) for different thickness CCT specimens. (a) 3 mm; (b) 6 mm and (c) 9 mm.

5. Influence of Stable Tearing on Fatigue Life

The presence of stable tearing complicates the prediction of crack growth rate. On one hand, the crack can extend by millimetres under the influence of a single high load (refer to Figs. 1-1 and 3-1). On other hand, the crack growth rate decreases significantly after the overload. Thousands of load cycles may be necessary to regain the initial growth rate due to growth retardation. The question is what effect stable tearing has on the overall fatigue crack growth rate.

The results of eight CCT specimens were examined at CEAT. The proposed procedure and hypothesis are shown in Fig.5-1, where the dot line curve represents a crack growth rate without tearing and the solid line curve is a crack growth rate with tearing. In this figure, assume both the crack growth rates are same during normal fatigue growth (see the arrows). The number of cycles measured during the test (ΔN_{test}) is required to retrieve the crack propagation rate obtained before the overload. The theoretical impact due to the overload on crack propagation is represented by ΔN . That the theoretical impact is larger than zero (i.e., $\Delta N > 0$) implies a delay (a longer propagation life) and $\Delta N < 0$ is crack growth (i.e. Δa predominant on overload effect). Because of the lack of the propagation curve ($a=f(N)$) without overload, so assume that $\Delta N \approx \Delta N_{\text{test}}$. The influence of stable tearing is shown in Table 5-1, where $\Delta N > 0$.

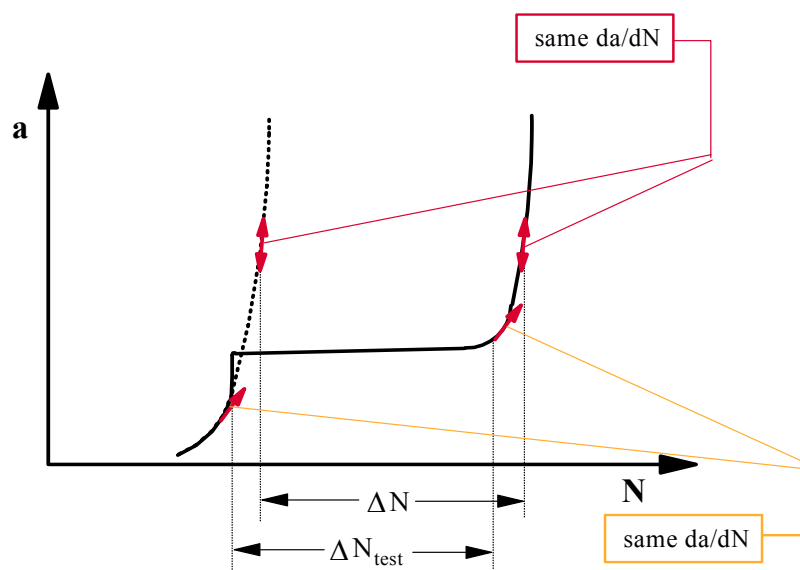


Fig. 5-1 The proposed procedure and the corresponding hypothesis $\Delta N \approx \Delta N_{\text{test}}$.

The results (ΔN) show that the presence of stable tearing leads to a longer propagation life for 7050 Al CCT specimen. In other words, the prediction of the model may remain conservative in the presence of stable tearing.

Table 5-1 Influence of stable tearing on the fatigue propagation life (number of cycles), ΔN , at different specimen thicknesses

Specimen/tear band	1	2	3	4	5	6
KWST-34	N.R.	+28 100	+20 100	+8 400	+2 700	+900
KWST-35	N.R.	+238 400	+27 400	+10 900	+200	N.R.
KWST-36	+26 300	+9 200	+3 300	+3 800	+2 600	+500
KWST-38	+446 500	+394 400	+85 600	+54 300	+23 600	N.R.
KWST-62	0	+113 700	+26 700	N.R.	N.R.	N.R.
KWST-66	N.R.	+3 300	+63 400	N.R.	N.R.	N.R.
KWST-67	0	+10 000	+20 000	+520 000	N.R.	N.R.
KWST-94	N.R.	+48 900	+5 600	+200	+300	N.R.

N.R. : No Result due to an increase of the load

6. R-Curve, Forsyth's and Schijve's Models

There are several empirical models available for analysis of tear band behaviour such as Schijve's and Forsyth's models. Previous DSTO experience has shown that these models work reasonably well on predictions for CT specimens but only for the post-failure analysis (Byrnes, et al, 2000). An alternative way is to apply the R-Curve concept to examine the prediction capability.

In this chapter, these models are used to examine CCT specimen data as predictive models for stable tearing. The limitations of these models are also briefly discussed.

6.1 R-Curve Method

For materials in an elastic condition, the crack driving force (i.e. G) defines the change of potential energy (U_e) per unit crack growth, i.e. dU_e/da . The crack propagates in a stable fashion when the following condition are satisfied,

$$G = R \quad (6-1)$$

and

$$\frac{dG}{da} \leq \frac{dR}{da} \quad (6-2)$$

whereas for unstable crack extension,

$$\frac{dG}{da} > \frac{dR}{da} \quad (6-3)$$

where R is the fracture resistance.

For a cracked specimen, made of a ductile material, in plane stress or intermediate plane stress/strain conditions, the R-curve depicts the increasing resistance of the material for an increasing stress. This rising of the R-curve (after the beginning of the crack extension) is mainly due to slow stable crack growth preceding instability, linked to the development of the crack tip plastic zone.

The R-curve concept is illustrated in Fig.6-1. Instability of crack propagation can be determined graphically by comparing the calculated crack driving force (G or K) curve with the measured crack resistance curve (R curve). For example, for a crack length of a and a remote stress of σ_0 , the K -curve cuts the R -curve at the point o . The crack driving force (G or K) curve is below R -curve, so stable crack growth happens. When the remote stress is increased to a critical point c , unstable crack propagation will occur, because the crack driving force is higher than the crack resistance curve ($dK/da > dR/da$).

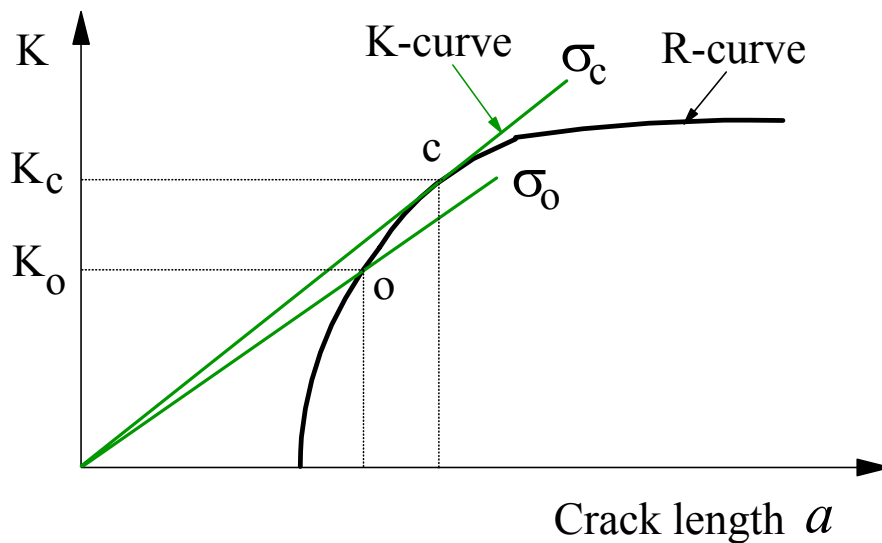


Fig.6-1 Schematic of R-curve Concept. K_c is the critical SIF at a critical stress σ_c (i.e. $G = P$ in Eq.(6-1)); K_0 is the SIF at a stress σ_0 below R-curve (i.e. $G < R$).

Due to the similitude of the phenomenon encountered in R-curve test and stable tearing test (during the overload), CEAT tried to assess the R-curve concept as a predictive model for stable tearing.

6.1.1 Procedure used for the Prediction of Tear Bands

The procedure for the prediction of stable tearing is shown in Fig.6-2. The R-curve is drawn in the $(\Delta K_{\text{eff}}; \Delta a_{\text{eff}})$ coordinate system. For each overload, the loading path (K curve) was calculated in the plane $(\Delta K_{\text{phys}}; \Delta a_{\text{phys}})$. Theoretically, the tear band would appear once the K curve cuts the R-curve.

The prediction of the crack tearing propagation Δa_{phys} was calculated by $\Delta a_{\text{phys}} = \Delta a_{\text{eff}} - r_y$ with r_y the plane stress Irwin's correction factor equal to $(1/2\pi)(K_{\text{eff}}/R_c)^2$; $R_c = 0.5(R_m + R_{0.2})$; R_m and $R_{0.2}$, the ultimate and elastic strength of the material, respectively.

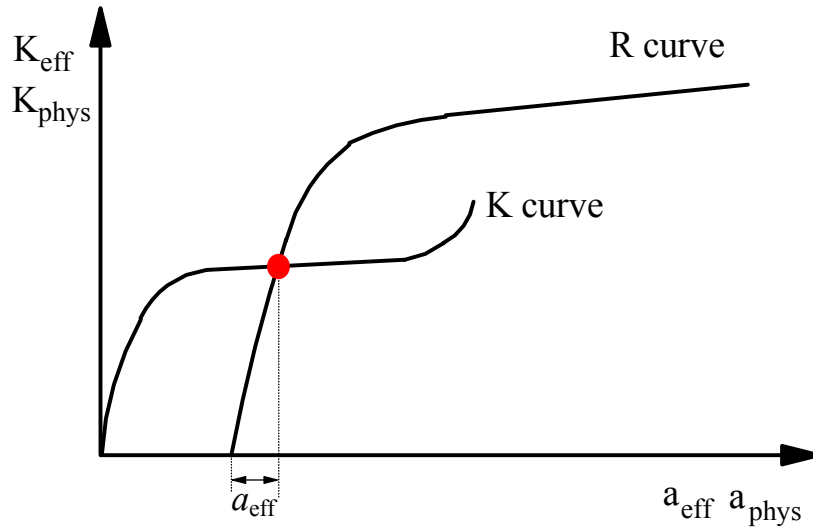


Fig.6-2 Procedure used for the prediction of tear bands.

6.1.2 Procedure for Calculation of Post Fracture Stress Intensity

This procedure is shown in Fig.6-3. The aim is to calculate the stress intensity K_{final} , which causes tearing from the data, Δa_{phys} , measured by the post failure analysis of the specimen.

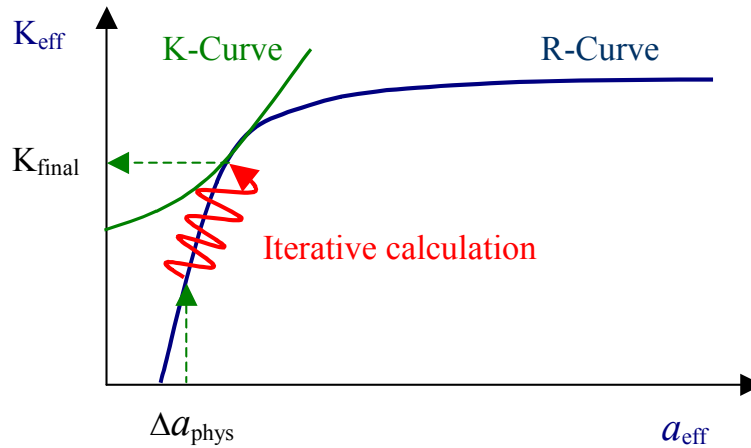


Fig.6-3 Procedure used for the calculation of K_{final}

The equation of the R-curve $K_{eff} = f(\Delta a_{eff})$ is expressed in the plane $(K_{eff}; a_{eff})$ and the following iterative calculation is necessary to calculate K_{eff} from Δa_{phys} . The plane stress Irwin's correction factor (r_y) is used (see Sec 6.1.1).



The K_{eff} calculated on the R-curve is theoretically at the cutting point of the K-curve of the specimen loaded, so that $K_{final} = K_{eff}$ (refer to Fig.6-2).

6.1.3 Predicted Results

The R-curve is obtained by the compliance method, which assumes a straight crack front only (ASTM E647). In fact, tear bands have curved crack fronts, which imply the experimental crack propagation (Δa_{exp}) greater than the length (Δa_R) of an equivalent straight band (same surface). Therefore, a correction factor was introduced for each thickness, which was defined as a ratio of Δa_R to Δa_{exp} , in the determination of Δa_{phys} and K_{final} . The Δa_{phys} and K_{final} values are determined by $\Delta a_{phys} = \Delta a_{calculated} / k$ and $K_{final} = \beta \sigma^\infty (\pi a)^{0.5}$ with $a = a_{initial} + \Delta a_{phy}$ and $\Delta a_{phy} = \Delta a_{exp} * k$. For each thickness, the Δa_R and the correction factor were calculated for each tear band. The correction factors (see Table 6-1) are the average values of these ratios.

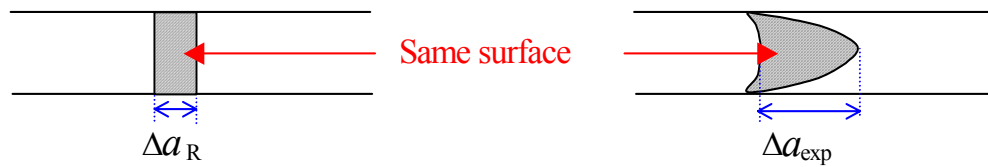


Table 6-1 Correction factor

Thickness	Correction factor $\Delta a_R / \Delta a_{exp}$
3 mm	0.5
6 mm	0.29
9 mm	0.99

The average results calculated by each procedure, with and without correction factor, are respectively shown in Tables 6-2 and 6-3. They are expressed in relative percentage by: $((\Delta a_{phys} - \Delta a_{exp}) / \Delta a_{exp}) * 100$.

Table 6-2 Results Δa_{phys} without and with correction

Thickness Number of tear bands	Criteria	Relative % on Δa_{phys}	
		Without correction	With correction
3 mm 24	Average Standard deviation	-40 % 21 %	20 % 43 %
6 mm 16	Average Standard deviation	-72 % 13 %	-5 % 46 %
9 mm 14		No result	

Table 6-3 Results K_{final} without and with correction

Thickness Number of tear bands	Criteria	Relative % on K_{final}	
		Without correction	With correction
3 mm 24	Average Standard deviation	20 % 8 %	-1,5 % 8 %
6 mm 16	Average Standard deviation	37 % 12 %	0,5 % 11 %
9 mm 14	Average Standard deviation	-9 % 10 %	-9 % 9 %

The results obtained by the R-curve concept show that:

- The prediction of the crack tearing propagation Δa_{phys} is not always possible (thick specimen) and the results are relatively good with the correction with some scatter.
- Post fracture calculation of the stress intensity, K_{final} , gives good results.

6.2 Forsyth and Schijve's Models

For convenience, two empirical models those of Forsyth and Schijve are briefly described here.

6.2.1 Forsyth's Model – A Geometrical Approach

Forsyth's model is a geometry-based approach (Forsyth, 1976; Bowen & Forsyth, 1981). A crack front length, l , incorporated with a maximum crack length at the centre of a specimen thickness (a_{max}), as shown in Fig. 6-4, is used for predicting stress intensity factor $K(a_{max})$.

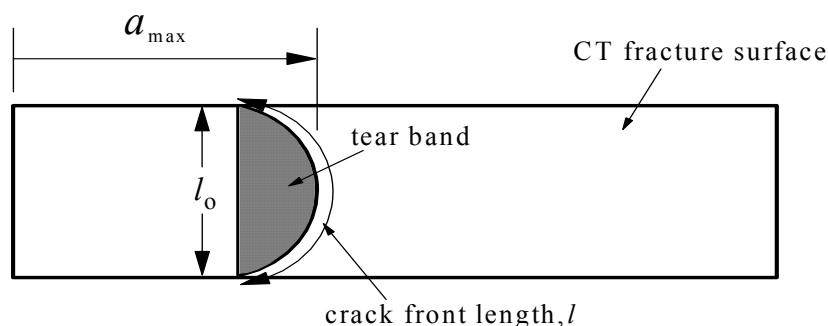


Fig.6-4 Geometrical parameters for Forsyth's model

When the crack front length is smaller than an equilibrium length, the crack can jump to an equilibrium position by brittle fracture. Here, the initial crack shape is assumed to be straight. When the crack front length is larger than an equilibrium length the crack will grow by fatigue. Therefore, at a equilibrium position, a basic relationship among critical stress intensity factor, K_{Ic} , maximum crack length, a_{max} , and crack front length, l , is given by

$$\frac{\sqrt{a_{max}}}{l} = \frac{K_{Ic}}{l_0 \sigma_{max} \sqrt{\pi}} \quad (6-4)$$

where σ_{max} is the maximum applied stress and l_0 the minimum crack front length, i.e., the specimen thickness. In this case, assume that the initial crack front shape is straight. In fact, the fatigue crack front is not straight, causing some errors in Forsyth's model. Equation (6-4) can be re-written in a simple form,

$$\frac{K(a_{max})}{K_{Ic}} = \frac{l}{l_0} \quad (6-5)$$

At the onset of tearing, when $l = l_0$ (i.e. the crack front is effectively straight = specimen thickness), Equation (6-5) states that $K(a_{max})$ is equal to K_{Ic} . Equation (6-5) implies that the K -value based on a_{max} can exceed K_{Ic} provided the crack front is larger than the thickness (i.e. a curved crack front).

As the loading increases, the stress intensity at the crack tip also increases above K_{Ic} until it reaches its maximum, $K(a_{max})$. However, at this point the crack front length has been increased and the *effective* stress intensity factor at the crack tip reduced by the ratio of l_0/l . The crack therefore remains stable and continues to grow by fatigue, during which the crack front straightens up eventually, the point is reached at which the crack tip stress intensity factor again exceeds K_{Ic} and another tear band is formed (Byrnes, et al, 2000).

6.2.2 Schijve's Model – A Fracture Mechanics Approach

Schijve's model considered the effect on a tear band due to different stress states along a specimen thickness (Vlasveld & Schijve, 1979). As a tear band is growing under increasing load the central part of the crack front will remain under predominantly plane strain conditions. The stress intensity along the central part is then expected to remain constant and approximately equal to the stress intensity at the initiation of the tear, which in turn is approximately equal to K_{Ic} .

The tear band phenomenon could be reduced to a two-dimensional problem model, which is illustrated in Fig. 6-5. Assume that the untorn ligament (AD_1D and $A'D_1'D'$)

By measuring the slope of the untorn ligament, the slope factor α may be calculated. Therefore, the stress intensity factor can be predicted by

$$K_I = -\frac{4\sigma_{0.2}\sqrt{\pi a_i}}{\pi t} \left[\frac{1}{\pi} \left(\frac{K_{Ic}}{\sigma_{0.2}} \right)^2 + \alpha \Delta a \right] \left[\sqrt{1 + 2 \frac{a_i}{\Delta a}} - \frac{a_i}{\Delta a} \operatorname{arc sec} \left(1 + \frac{\Delta a}{a_i} \right) \right] \sqrt{1 + \frac{\Delta a}{a_i}} \quad (6-10)$$

where t is the specimen thickness, a_i is the initial crack length and Δa is the crack length extension (note that the ligament stress intensity is negative). This ligament stress intensity acts against the applied loading such that at the conclusion of tearing:

$$K_{D_1 D_1'} = K(a_{\max}) + K_I = K_{Ic}. \quad (6-11)$$

At maximum applied load, the SIF at the crack front $D_1 D_1'$ remains equal to the plane strain fracture toughness, while the excess stress intensity is taken up by the untorn ligaments.

However, Schijve's model requires measurements of crack depth, a , increment in crack depth after tearing, Δa , and the slope of the tear band ligament, β . Generally, β can be determined by averaging β_1 and β_2 from the measurements on the fracture surface, i.e., $\beta_{av} = (\beta_1 + \beta_2) / 2$, as shown in Fig.6-6.

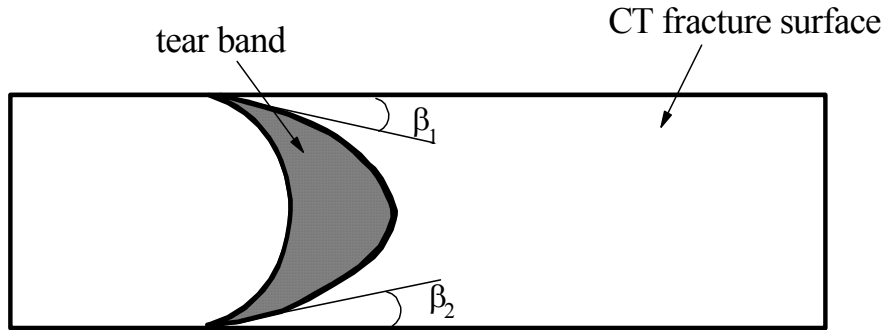


Fig.6-6 Determination of the slope of tear band ligament from the fracture surface.

6.3 Comparison of Forsyth's, Schijve's and R-curve results

The results on CCT specimens obtained by the three models are compared in Tables 6-4 and 6-5.

Table 6-4 Schijve's and R-Curve results Δa_{phys}

Thickness Number of tear bands	Criteria	Relative % on Δa_{phys}	
		Schijve's model	R-curve concept with correction
3 mm 24	Average Standard deviation	52 %	20 %
		42 %	41 %
6 mm 16	Average Standard deviation	14 %	1 %
		36 %	46 %
9 mm 14	Average Standard deviation	11 %	No result
		128 %	

Table 6-5 Forsyth's, Schijve's and R-Curve results K_{final}

Thickness Number of tear bands	Criteria	Relative % on K_{final}		
		Forsyth's	Schijve's	R-curve concept with correction
3 mm 24	Average Standard deviation	13 %	-14 %	-2 %
		22 %	7 %	8 %
6 mm 16	Average Standard deviation	11 %	1 %	-1 %
		17 %	14 %	11 %
9 mm 14	Average Standard deviation	21 %	13 %	-9 %
		17 %	15 %	9 %

The comparison of these results shows that the R-curve concept:

- Gives better Δa_{phys} prediction than Schijve's model but is limited to thin specimen.
- Gives slightly better results K_{final} than Forsyth's and Schijve's models.

This study has shown the capability of the R-curve concept to predict crack tearing propagation Δa_{phys} and the stress intensity (K_{final}), which causes the stable tearing. But the accuracy relies on R-curve (same material and thickness) and a specific correction dependent on the thickness and the material. So, this model cannot be used as a predictive model but is shown to be efficient for post fracture analyses. Therefore, the R-Curve method is an alternative to Schijve's model for post failure analyses only. However, the difficulty also arises for stable tearing because we need to compare the

local K , and the local R at each point on the crack front rather than overall K and R , as shown in Fig.6-1.

Furthermore, the experimental results, obtained by the tearing models of Forsyth and Schijve on CCT specimens, further confirm previous DSTO results on CT specimens (Byrnes, et al, 2000), i.e., they are good predictors of the stress intensity factor, K_{final} but only useful for post fracture analysis. Therefore, an appropriate numerical modelling capability needs to be developed for enhancing the prediction of tearing behaviour.

7. A Three-Dimensional Finite Element Model Using ZENCRACK Package

As stated previously, in both CCT and CT specimen tests, one of the most noticeable physical changes to the fracture surface before and after tearing fracture is the change in curvature of the crack tip front. This change is dependent on specimen geometry, particularly thickness, material properties (i.e. fracture resistance) and stress distribution. The change of the crack tip front shape could alter the values of stress intensity factor (SIF) around the crack tip front under elastic condition or other fracture parameters under elastic-plastic conditions.

The ZENCRACK[®] 3D FE package (1998, 2002) combined with ABAQUS[®] was adopted to develop FE models of the CT and CCT geometries under elastic conditions, which can be used to determine the SIF along crack tip fronts of different curvatures. The numerical results calculated using ABAQUS[®] only under the elastic-plastic condition are also included in this report. Additionally, a new three-dimensional model using cohesive zone approach and corresponding preliminary results is discussed in Chapters 8 and 9.

7.1 ZENCRACK Package

The evaluation of crack growth has generally been limited to planar cracks in 3D structures, usually under mode I loading only. ZENCRACK[®] is used to solve 3D crack problems by providing a meshing and crack growth capability (Zentech, 1998, 2002).

7.1.1 Principle

ZENCRACK[®] uses the finite element method via interfaces to ABAQUS[®] to provide a versatile and powerful analysis tool. Users have at their disposal all of the capabilities within these finite element programs and may, if desired, include any number of non-linear features in an analysis in addition to being able to carry out a "standard" linear elastic fracture mechanics analysis.

ZENCRACK[®] uses a so-called "crack-block" approach to quickly and easily generate 3D finite element models of cracked components from user supplied uncracked meshes. The cracked mesh is submitted for analysis to ABAQUS[®] with subsequent crack growth calculations carried out automatically if required. The crack growth scheme caters for full 3D crack growth of arbitrary 3D crack fronts under mixed mode loading. The program incorporates an adaptive meshing scheme to generate and update finite element meshes to simulate crack growth. The basic flow chart for using ZENCRACK[®] is illustrated in Fig.7-1.

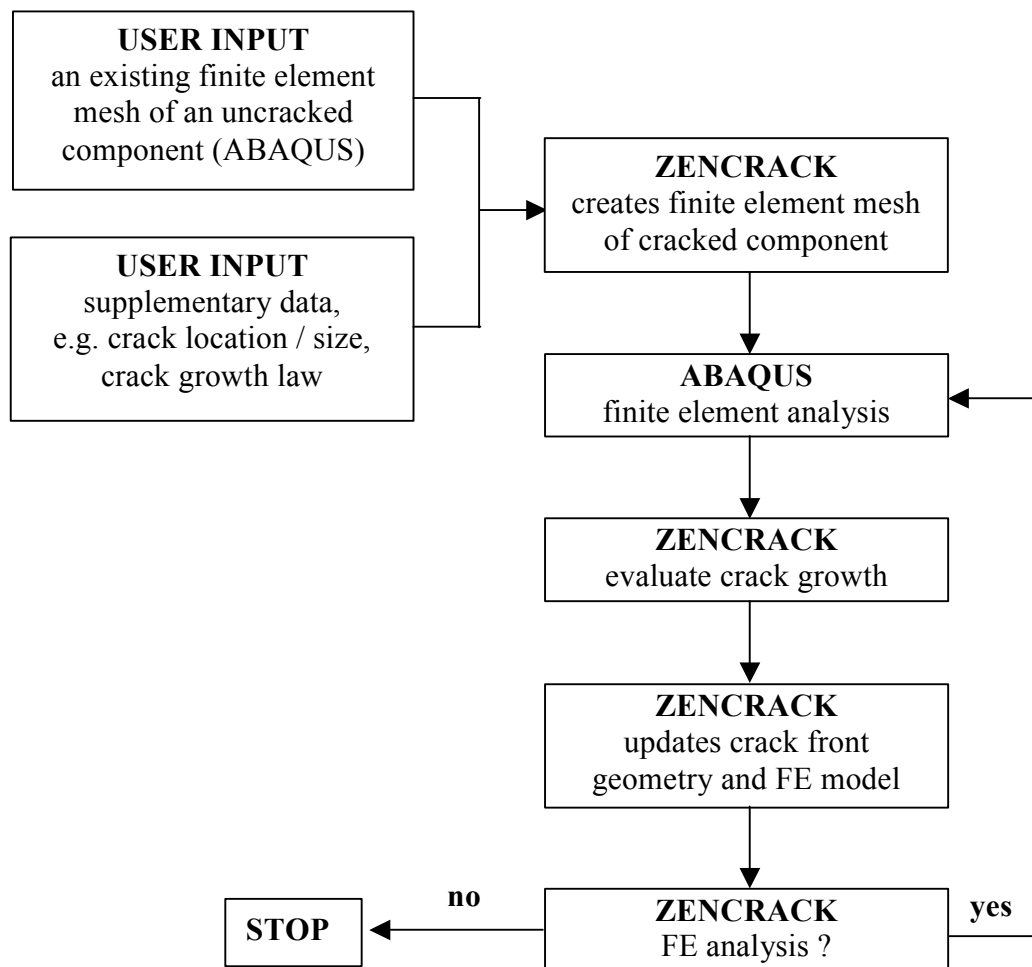


Fig.7-1 Simplified flow chart for crack growth prediction analysis in ZENCRACK.

7.1.2 Crack-Blocks

One of the main features of ZENCRACK[®] is to use the crack-blocks. The crack-block approach is used to generate 3D meshes containing one or more crack fronts. The crack block is a mesh defined by a series of brick elements that are arranged specifically to

model a crack front. The term crack-block refers to a collection of 20-node brick element stored as a unit cube. The arrangement of these crack-blocks is such that they contain either a quarter circular or through crack front on one face. Part of this face is allowed to open up under loading giving the opening crack face within the crack-block. Examples of unit cube crack-blocks are shown in Fig.7-2 and Fig.7-3 with their opening crack faces shaded for clarity (Zentech, 1998).

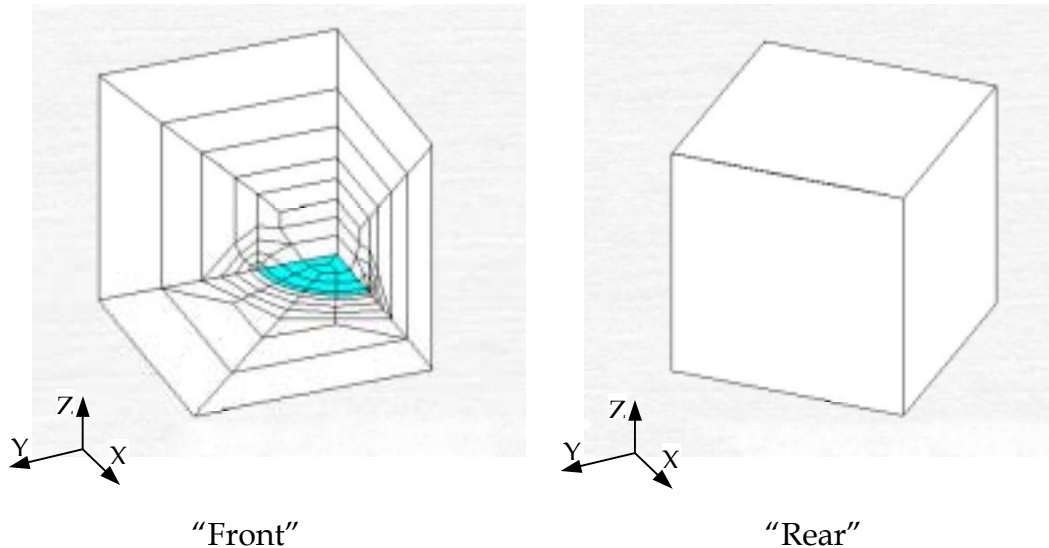


Fig. 7-2 Example of a quarter circular crack-block (Zentech, 1998, 2002)

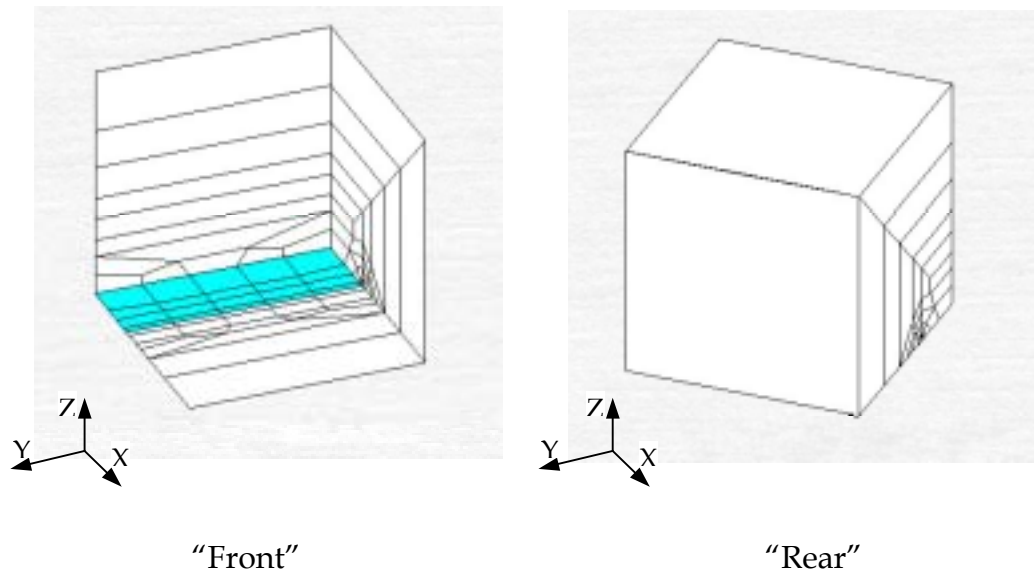


Fig. 7-3 Example of a through crack-block (Zentech, 1998, 2002)

About 25 different 3D crack-blocks are available in the crack-block library of ZENCRACK[®] package. According to the problem to be analysed, suitable crack-blocks can be selected from the library to form a desired crack front. The details can be seen in ZENCRACK[®] Manuals (Zentch, 1998, 2002).

7.1.3 Procedure of ZENCRACK Modelling

To begin the process of analysis the FE model needs to be generated for calculation by ABAQUS. The specimen can be represented by a fairly straightforward FE model. Then the crack-blocks are used to replace some of existing 3D elements around the crack tip in the FE model. For example, Fig.7-4 illustrates an example of modelling a single edge notched (SEN) specimen consisting of 16×3D elements, where normal 3D elements 7 and 11 (Fig.7-4 (a)) are replaced by the crack-blocks (Fig.7-4 (b)). The elements 8 and 12 are split in order to create a crack.

Once appropriate boundary and loading conditions as well as material properties are given, the modified input file can be generated and then sent to ABAQUS for the calculation. One of the shortcomings of ZENCRACK is that the input file must be manually rewritten, including all details such as the name of the crack-block. The input file, which is generated by PATRAN, with uncracked meshes must be written into the ZENCRACK input file.

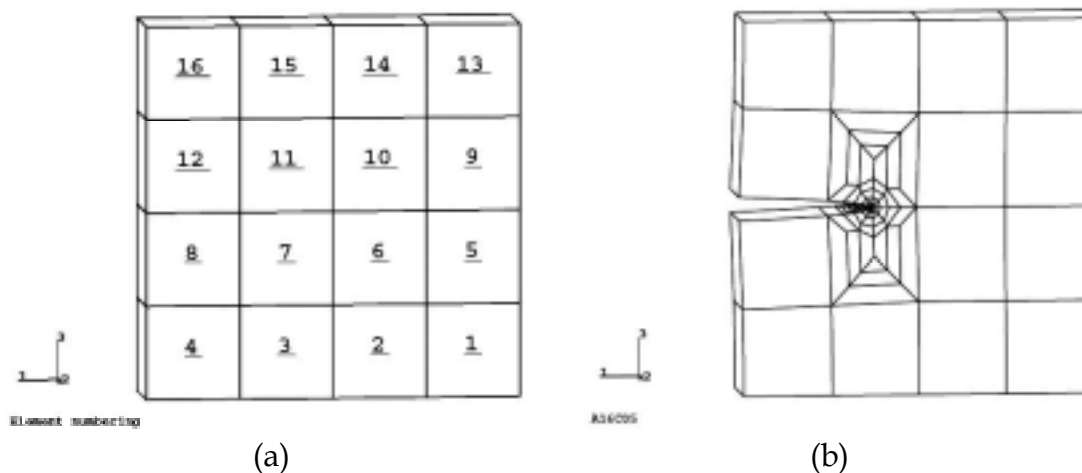


Fig.7-4 Procedure of modelling a SEN specimen using ZENCRACK. (a) a standard FE model by ABAQUS and (b) a modified FE model by ZENCRACK (Zentech, 2002).

7.2 Calculations of Stress Intensity Factors (SIFs)

7.2.1 Using ZENCRACK

ZENCRACK calculates the SIF along the crack front using two methods, crack tip opening displacement and the energy release rate along the crack front. In this report the SIF from the crack tip opening displacement is presented for all specimens except the 3 mm CCT specimen where it was found that the SIF from energy release rate provided a better match to the theoretical SIF and gave a better SIF distribution.

The equation used in ZENCRACK for calculation of the SIF from crack tip displacement is given in Equation (7-1),

$$K = \frac{EV}{4(1-\nu^2)} \sqrt{\frac{2\pi}{r}} \quad (7-1)$$

where K is stress intensity factor; E is Young's modulus; V is crack opening displacement; r is the distance from the crack front to point of displacement measurement and ν is Poisson's ratio.

The equation used by ZENCRACK for calculation of the SIF from the maximum energy release rate is given in Equation 7-2,

$$K = \left[\frac{EG}{1-(\alpha_k \nu)^2} \right]^{\frac{1}{2}} \quad (7-2)$$

where G is the energy release rate and $\alpha_k = 0$ for plane stress and 1 for plane strain, intermediate values are acceptable. The remaining symbols in Equation (7-2) are the same as in Equation (7-1).

The SIFs along a crack front presented in this report are given for the plane strain condition. For simulation of stable tearing the plane strain, plane stress and combinations are examined. The numerical results by FEA are given in Chapter 9 and discussed in Chapter 10.

7.2.2 Using ABAQUS Code

In ABAQUS, the SIF is calculated from the energy release rate (J-integral), based on the following relationship,

$$J = \frac{1}{8\pi} \mathbf{K}^T \cdot \mathbf{B}^{-1} \cdot \mathbf{K} \quad (7-3)$$

where $\mathbf{K} = [K_I, K_{II}, K_{III}]^T$ are stress intensity factors in modes I, II, II, respectively and \mathbf{B} is called the pre-logarithmic energy factor matrix. For homogeneous, isotropic material and Mode I, \mathbf{B} is a diagonal matrix, so the above equation can be simplified to

$$J = \frac{1}{E^*} K_I^2 \quad (7-4)$$

where $E^* = E$ for plane stress and $E^* = E/(1-\nu^2)$ for plane strain.

7.3 Fatigue Crack Growth in ZENCRACK

For simulation of fatigue crack growth, ZENCRACK calculates the fatigue crack growth based on the assumption that the direction of crack growth at any point on the crack front is given by the direction of maximum energy release rate normal to the crack front (Zentech, 2002). ZENCRACK uses the finite element code - ABAQUS, as a tool for generating the required energy release rates at the crack front.

ABAQUS employs the contour integral approach to evaluate the energy release rates required by ZENCRACK. By calculating the contour integral, the J-integral can characterise energy release associated with crack growth behaviour. ABAQUS can provide ZENCRACK with the required input from crack front node sets and direction vectors.

To predict fatigue crack growth rates ZENCRACK can incorporate experimental crack growth data via implementation of the Paris equation. Sections of the curves generated through specimen testing can be approximated by this standard formulation (Paris equation), given in Equation (7-5) as follows,

$$\frac{da}{dN} = C(\Delta K)^m \quad (7-5)$$

where C and m are material constants; a is crack length, N is number of fatigue cycles and ΔK is stress intensity factor range $= K_{\max} - K_{\min}$. The user can input two or more points of the experimental data or the Paris equation parameters. Experimental data must be supplied for the same stress ratio as that is being used for the analysis. ZENCRACK employs a reformulated version of the Paris equation for mixed mode cases where the maximum and minimum energy release rates along a crack front must be in the same direction. In this reformulation the maximum and minimum stress intensity factors are converted directly into energy release rates to give the following equation (Zentech, 2002),

$$\frac{da}{dN} = C \left(\frac{E}{1 - (\alpha_k \nu)^2} \right) (G_{\max}^{1/2} - G_{\min}^{1/2})^m \quad (7-6)$$

where G is the energy release rate, E is Young's modulus, ν is Poisson ratio, α_k is constant between 0 and 1 depending on the state of stress in the experimental specimen averaged over the crack front ($\alpha_k = 0$ for plane stress and $\alpha_k = 1$ for plane strain).

ZENCRACK then employs one of two schemes, based on the energy release rates in equation (7-6), to predict crack growth. The first is a constant G scheme where the energy release rate distribution for an obtained crack front shape is held constant and is used to predict crack growth for a given increment in the number of cycles. This is not always reliable, particularly when G increases with increasing crack growth where the energy release rate at the end of the crack growth stage is higher than the beginning. In such a case the constant G scheme will underestimate the crack growth for a given increment.

The second and more reliable method is the forward predictor scheme whereby the variation in energy release rate is estimated over the next crack growth step. This is then used to predict the crack growth. The G variation from the previous increment can be used over the next increment so the crack growth rate in equation (7-6) can be integrated to give the crack growth. In this study, this second method was adopted.

In this study, the Walker equation was used for calculating crack growth rates, when the effect of R ratio was included. The Walker equation is presented by

$$\frac{da}{dN} = C_o (\Delta K_o)^n \quad (7-7)$$

$$\Delta K = \Delta K_o (1 - R)^{(1-m)}. \quad (7-8)$$

Substituting Equation 7-8 into Equation 7-7, gives

$$\frac{da}{dN} = C_o [\Delta K (1 - R)^{(m-1)}]^n \quad (7-9)$$

where R is stress ratio; C_o , n and m are material constants. The subscript o refers to C value at $R=0$. In this study, C_o is $7.74000E-13$, n is 3.2 and m is 0.5, based on experimental data and open literature. When an overload was applied, a higher ΔK can be expected. As a result, a larger crack extension or the "crack jump" (i.e. stable tearing) occurred.

7.4 Modelling for Compact Tension (CT)

A FE model was created for each of the three specimen dimensions. The FE models for the 12 and 24 mm (thickness) models contained 32 hexagonal 20-noded elements in total with two elements through the thickness of the specimen. The 6 mm model contained 16 hexagonal 20-noded elements in total with one element through the thickness of the specimen. An example of the 24 mm model is shown in Fig.7-5. Specimen symmetry was not utilized for the models because the ZENCRACK crack blocks are located along the line of symmetry. Constraint was provided on the crack plane opposite the crack initiation points and additional soft springs were added to the bottom of the model to prevent numerical singularities in the analysis without over-constraining the model.

The applied loads on the CT model are located at the point representative of the load pins on the CT specimen. For the model with two elements through the thickness the loads are divided so that half the load is applied to the middle node and a quarter of the load is applied to the nodes at the surface. For the 6 mm model that had one element through the thickness half the load was applied at the nodes at the surface of the specimen. The details of FE models using ZENCRACK can be seen in the reports from Aerostructure Technologies Ltd Australia (Goldstraw, 1999 and Stoessiger, 2002). The crack-block chosen to represent the crack tip was the **st151x5** block, which was from the ZENCRACK crack-block library. The **st151x5** crack-block has 6 nodes along the crack tip front. As ZENCRACK calculates the SIF at the ends of each node along the crack tip, this crack-block provides enough SIF data. The **st151x5** crack-block can be seen in Fig.7-6.

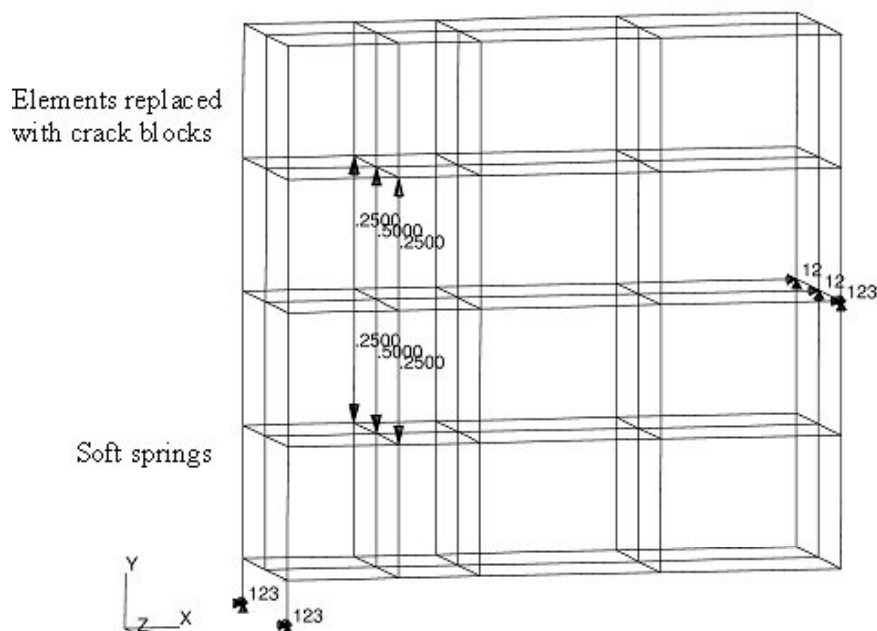


Fig.7-5 A 24 mm CT FE model with 32 elements for ZENCRACK

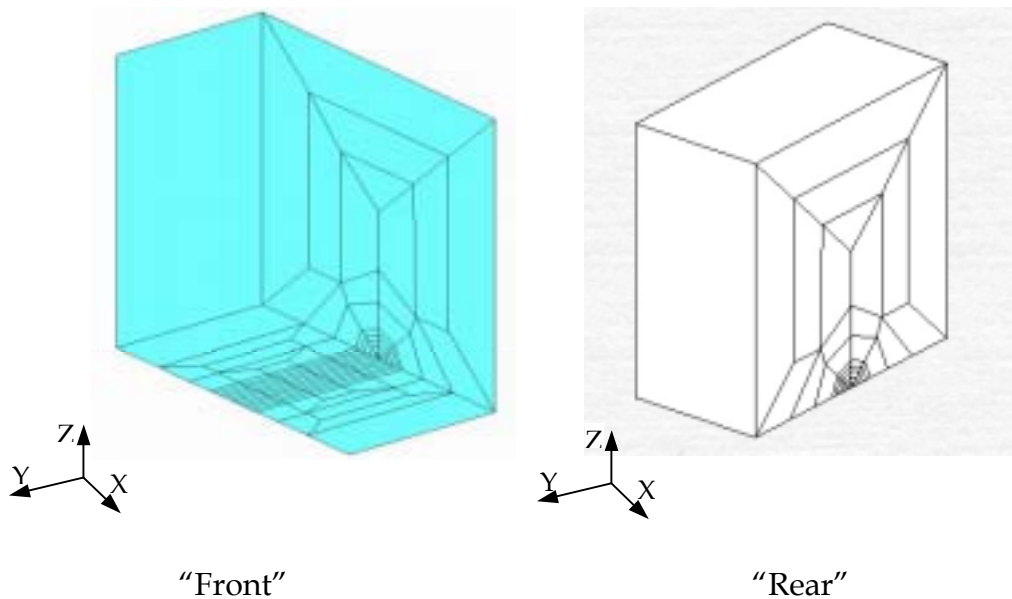


Fig. 7-6 Crack-block *st151x5* (Zentech, 1998, 2002)

7.5 Modelling for Centre-Cracked Tension (CCT)

The finite element model of the CCT specimen simplified the geometry to a panel with a centre crack. The requirements of ZENCRACK in terms of element shape and size would not have been able to be met if the central hole was modelled. This simplification is a relatively minor one because as the crack grows larger the effect of the hole diminishes, and the stress distribution is solely influenced by the geometry of the crack.

Constraint was provided on the crack plane at one end of the model. Soft springs were added to the opposite bottom corner to prevent numerical singularities without over constraining the model. An example of the 9 mm thick CCT model is shown in Fig.7-7. Note that the FE model is rotated 90 degrees with respect to Fig.2-1. All of the CCT models contained one element through thickness. The total number of elements were 20, where 4 of these elements were crack-block.

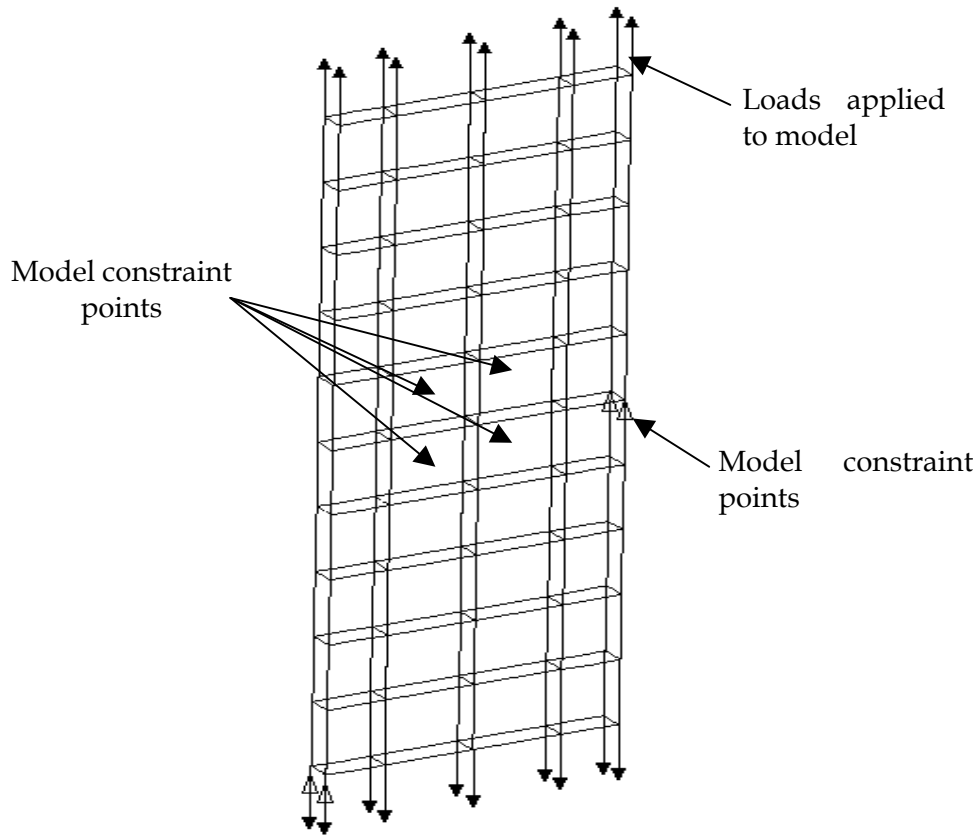


Fig.7-7 A 9 mm CCT FE model for ZENCRACK code

7.6 A Curved Crack Tip Front

7.6.1 Definition of a Curved Crack Tip Front

In order to investigate the effect of the shape of a crack front on stress distribution, two types of crack profile were used: (i) a straight crack front and (ii) a curved crack front with different curvatures, which was defined by the height at the mid-thickness (interior), normalized by the thickness (Fig.7-8), which can be calculated (in percent) by the following formula. This definition was applied to both the CT and CCT specimens,

$$C_r = \frac{h}{B} \times 100\% . \quad (7-10)$$

In Fig.7-8, a_v is the average crack length of 11 points along the crack front, B is specimen thickness and h is the difference in length between the surface crack and the central crack.

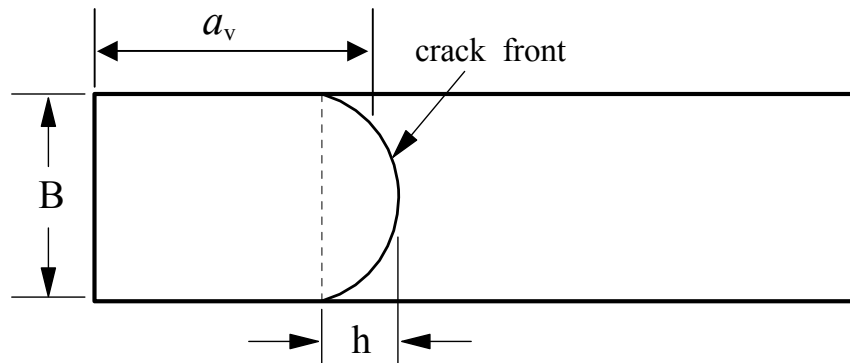


Fig.7-8 Definition of a curvature at a crack tip front

7.6.2 Creation of a Curved Crack Tip Front

In this study of effect of a curved crack front on stress distribution, a curved crack front was produced by ZENCRACK. However, it is not possible to specify a specific crack front shape beforehand due to the limitations of ZENCRACK. In order to produce a curved front shape, a straight crack front was utilised by setting a high fracture toughness value for the models to prevent specimen failure. Then a higher initial load (i.e. overload) was applied, causing crack growth jumping several millimetres. A curved crack front can thus be obtained, depending on the amount of overload and specimen thickness.

The crack growth of one to two millimetres in one cycle produced a highly curved crack front. In this study, a constant amplitude load of 13,533 N ($R = 0$) was applied (Stoessiger, 2002). The same constant amplitude load was applied to each specimen, which led to a variation in the applied stress on each specimen due to the change in specimen thickness (i.e. 6, 12 and 24 mm). To generate a crack curvature, different loads, which were several times of the constant amplitude load, were applied to a model geometry and different thicknesses of CT and CCT specimens. Table 7-1 gives an example of the initial applied loads for the CT specimens. It should be noted that all the SIF data presented for the CT specimens is for a load of 13,533 N.

The same method was used to create large crack front curvatures for the CCT model. A single large load was initially applied to the specimen to create crack growth of approximately one to two millimetres, and the large load was then followed by constant amplitude loading of 20,000 N with $R=0$. The same constant amplitude load was applied to each specimen, which led to a variation in the applied stress on each specimen due to the change in specimen thickness. A summary of the loads applied to the CCT specimen is shown in Table 7-2. All SIF data presented in this report for the CCT specimens is for a load of 20,000 N.

Table 7-1 CT specimen initial loads (overloads)

Specimen Thickness (mm)	Initial Load (N)	Initial Load as a Factor of Constant Amplitude Load	Crack Curvature Generated (%)
24	270,660	20	8.55
24	338,325	25	17.47
12	135,330	10	15.45
12	162,396	12	27.69
6	67,665	5	24.02
6	81,198	6	43.66

Table 7-2 CCT specimen initial loads (overloads)

Specimen Thickness (mm)	Initial Load (N)	Initial Load as a Factor of Constant Amplitude Load	Crack Curvature Generated (%)
9	1,200,000	60	7.13
9	1,400,000	70	11.5
6	600,000	30	4.86
6	800,000	40	12.04
3	300,000	15	10.67
3	400,000	20	27.44

8. A 3D FE Model Using Cohesive Zone Approach

The stable tearing during fatigue is by nature a three-dimensional problem involving large plasticity. In this Chapter, we intend to explore the capability of cohesive zone modelling on the prediction of the parameters governing the stable tearing mechanism of crack growth. The aim is to develop a dual crack growth model based on the cohesive zone approach and the plasticity induced crack closure approach, to capture the events of rapid tearing during otherwise stable fatigue crack growth. For this

purpose, it is important to have the crack growth resistance behaviour for a given crack configuration.

8.1 Cohesive Zone Approach

8.1.1 Basic Principle

The cohesive zone model originated from the Dugdale model (1960) and the Barenblatt model (1962), which described the non-linear crack behaviour by means of cohesive forces in the process zone (Fig.8-1). Later, the model was modified by Needleman (1987, 1990), Tvergaard and Hutchinson (1992), Schwable & Cornec (1994), Ortiz & Pandofi (1999) and others.

Compared to the Gurson (1977)-Tvergaard (1990) model, there are no damage continuum elements in the cohesive zone model. Cohesive interface elements are instead introduced between the continuum elements (Needleman, 1987). When damage occurs, the interface elements open and lose their stiffness at failure. Therefore, the continuum elements are disconnected and the crack can propagate along the element boundaries. In other words, if the material behaviour at the crack tip is represented by a traction-separation law, with increasing interfacial separation, the traction across the interface first increases to a maximum, then decreases, and eventually vanishes, leading to complete separation of the material. Fig.8-2 illustrates different types of traction-separation laws.

The main problem for modelling the stable tearing is the lack of an appropriate local criterion for the “crack jump” and “arrest”. The advantage of the cohesive zone approach is that it does not require a failure criterion. Therefore, the difficulty in finding an appropriate criterion can be avoided.

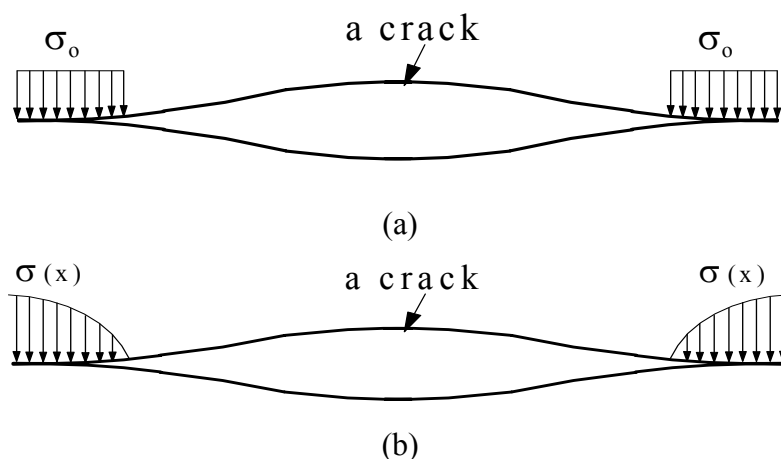


Fig. 8-1 (a) Dugdale model and (b) Barenblatt Model.

8.1.2 Mathematical Formulation

The cohesive zone model used in this study was primarily based on the work of Needleman (1987, 1990) and Ortiz and Pandolfi (1999). The 3D finite element implementation (WARP 3D) is from the University of Illinois (Gullerud, et al, 2002).

The local traction, \mathbf{t} , between the cohesive faces can be derived from a free energy density function per unit area, based on the first and second laws of thermodynamics (Needleman 1987; Gullerud et al. 2002),

$$\mathbf{t} = \frac{\partial \phi(\boldsymbol{\delta}, \mathbf{q})}{\partial \boldsymbol{\delta}} \quad (8-1)$$

where $\boldsymbol{\delta}$ represents the displacement jump across the cohesive surfaces, and \mathbf{q} denotes a set of internal variables that describe the inelastic processes of decohesion.

In three-dimensional problems, the local separation between the interfaces has three components, a normal component δ_n and two mutually perpendicular sliding components δ_{s1} and δ_{s2} . The sliding components may be combined to give $\delta_s = \sqrt{\delta_{s1}^2 + \delta_{s2}^2}$, so that the total traction can also be resolved into two components along the corresponding directions,

$$\mathbf{t} = \mathbf{t}_n + \mathbf{t}_s. \quad (8-2)$$

The normal and sliding components are further combined into an effective separation (Camacho and Ortiz 1996),

$$\delta = \sqrt{\delta_n^2 + \beta^2 \delta_s^2} \quad (8-3)$$

where β is a scale factor specifying the weight of sliding separation. Following this treatment, the cohesive traction can be expressed as

$$t = \frac{t}{\delta} (\beta^2 \delta_s + \delta_n n) \quad (8-4)$$

where \mathbf{n} is the unit normal to the interface, see Fig.8-3, and \mathbf{n} is chosen so that $\boldsymbol{\delta} \cdot \mathbf{n} > 0$ for opening separation, and t is the work-conjugate effective traction

$$t = \frac{\partial \phi(\boldsymbol{\delta}, \mathbf{q})}{\partial \delta}. \quad (8-5)$$

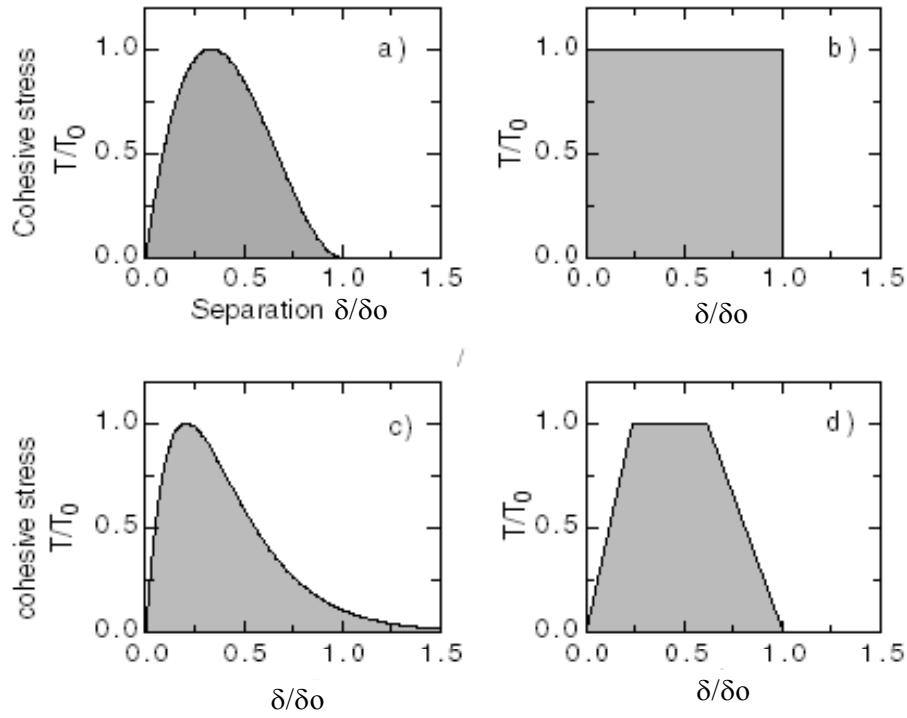


Fig.8-2 Types of traction-separation laws used in the cohesive zone model. (a) Cubic form (Needleman, 1987); (b) Constant form (Schwable & Cornec, 1994); (c) Exponential form (Needleman, 1990) and (d) Tri-linear form (Tvergaard & Hutchinson, 1992).

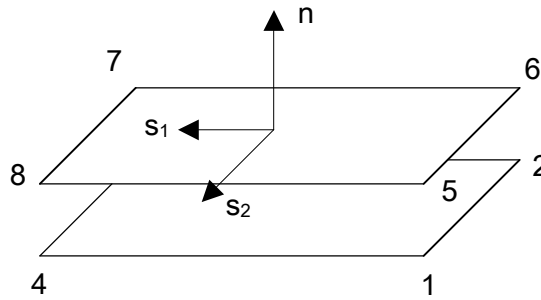


Fig.8-3 Topology for cohesive interface elements

The traction-separation law adopted for the cohesive element is described by

$$t = \frac{\partial \phi}{\partial \delta} = e \sigma_{\text{coh}} \frac{\delta}{\delta_c} \exp\left(-\frac{\delta}{\delta_c}\right) \quad (8-6)$$

where $e = \exp(1)$. The traction-separation law is graphically shown in Fig.8-2 (c) for the loading branch. The unloading and reloading path is assumed to be radial, until it meets the loading path again. The path will then follow the original loading path.

8.2 A Finite Element Model Using Cohesive Zone Approach

In this study, the FE package, called Warp3D, was selected. This FE package is designed for the solution of very large-scale, 3-D solid models subjected to static and dynamic loads, which was developed by the Computational Fracture Mechanics Research Group at the University of Illinois, USA. One of the advantages of this FE package is that it allows that a user access to the original code. The non-linear material models such as viscoplastic effects and the Gurson-Tvergaard dilatant plasticity model for void growth are included. Additionally, the crack-tip opening angle (CTOA) can be used to simulate the crack growth (Koppenhoefer, et al, 1994; Gullerud, et al, 2002). Since stable tearing by nature involves in a large plasticity, this FE package can be used for establishing a 3D modelling with large plasticity. This approach has been successfully applied in describing tearing behaviour under static loading (Hu & Liu, 2003).

Essentially, the potential crack plane is modelled by so-called interface cohesive zone elements, which purport to simulate the material behaviour at the crack tip. Under the applied external tensile load, the originally coinciding points on the interface start to separate, and the traction between them increases. A traction-separation law may be defined to describe the behaviour of the interface. Considering the physical process occurring at the crack tip, the traction-separation law may be specified as first increase to a maximum, then decrease to zero when the separation between the interface points reaches a critical value, mimicking the separation process of material particles. A schematic of cohesive zone model with cohesive stress-separation law is illustrated in Fig.8-4. In this study, nonlinear cohesive model in terms of effective traction – separation was used, as shown in Fig.8-5 (refer to Fig.8-2 (c)).

In this new model, the uniaxial stress-strain response of 7050 aluminium alloy is described by the von Mises material model in WARP3D, which uses the initial yield stress and the Young's modulus to define the linear elastic relation, and uses a power law to define the subsequent hardening behaviour, as shown in Fig. 8-6. The properties of the cohesive interface, σ_{coh} and δ_c , are determined based on the results of Tvergaard and Hutchinson (1992 & 1993), where it has been found that under a constrained stress state, the cohesive strength can be approximately three times the yield strength of the material. Therefore, $\sigma_{coh} = 3\sigma_y$ was taken as a first approximation. The value of δ_c is then determined by considering the energy balance at crack initiation. Ignoring the small amount of plastic energy dissipation at this stage, the cohesive energy can be related to the critical value of J-integral, i.e.

$$J_{lc} = \Gamma_c \quad (8-7)$$

where the cohesive energy may be obtained by integrating the traction given in Eq. (8-8) as follows,

$$\Gamma_c = \int_0^{\infty} t d\delta = \exp(1) \sigma_{coh} \delta_c \quad (8-8)$$

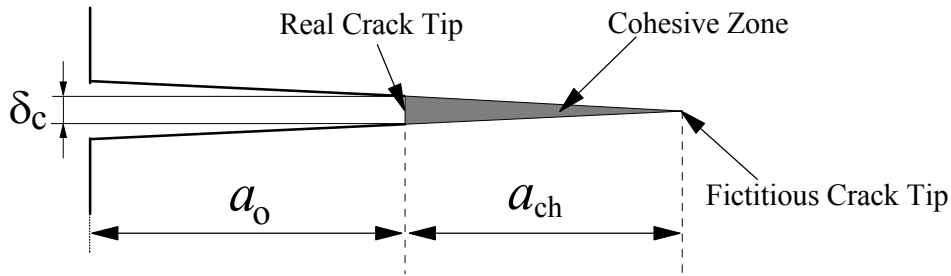


Fig.8-4 Schematic of a cohesive zone model. a_o is the original crack length; a_{ch} is the cohesive zone length and the δ_c is the separation or opening displacement at a physical crack tip.

On the other hand, the critical value of J-integral can be related to the plane strain stress intensity factor K_{lc} through

$$J_{lc} = \frac{1-\nu^2}{E} K_{lc}^2 \quad (8-9)$$

Substituting Eqs.(8-8) and (8-9) into Eq. (8-7), we get

$$\delta_c = \frac{K_{lc}^2 (1-\nu^2)^{1/2}}{3eE\sigma_y} \quad (8-10)$$

which gives a δ_c of 0.0037 mm. It should be noted that currently there is no analytical method for determining the cohesive parameters, and these parameters do not necessarily represent the fundamental material properties at the atomic level, as the size of the cohesive zone is in micrometres rather than nanometres. From the viewpoint of numerical modelling, it is sufficient if the parameters can capture the macroscopic deformation characteristics in the fracture zone, *i.e.*, the material response

can match the corresponding experimental data in terms of load, displacements and crack extension.

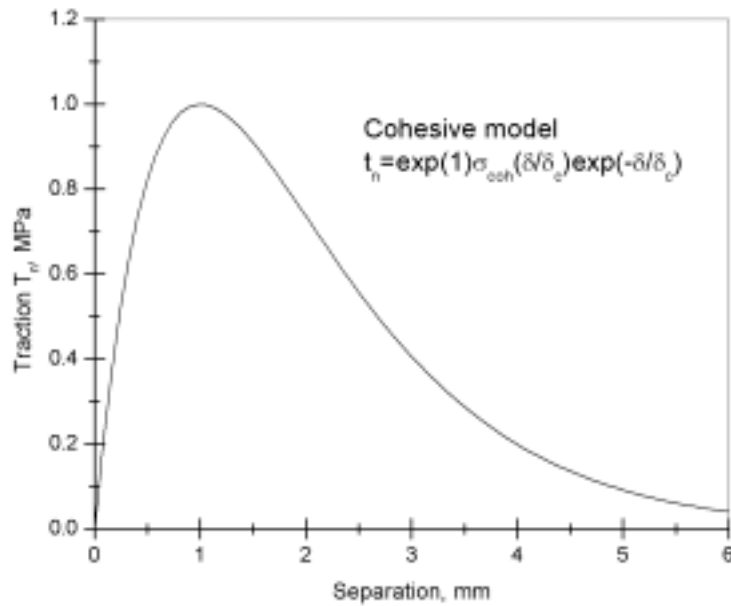


Fig. 8-5 Nonlinear cohesive model in terms of effective traction and effective separation.

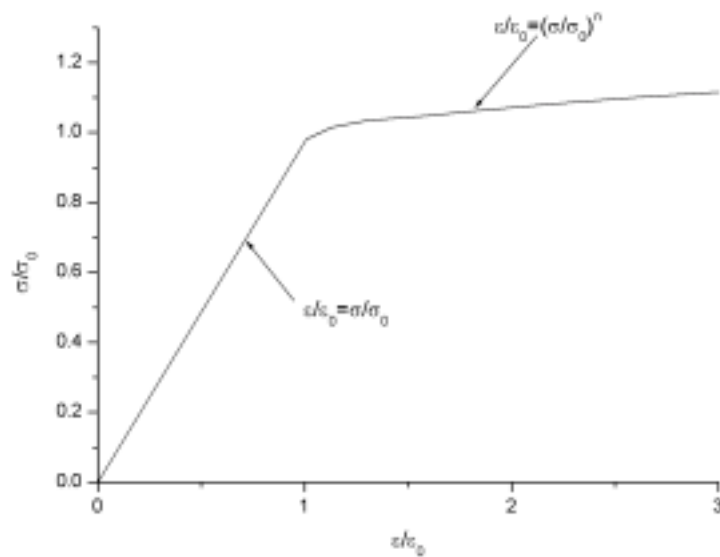


Fig. 8-6 Uniaxial stress strain behaviour of aluminium 7050

The bulk material of the specimens was modelled with 8-noded brick elements. By taking advantage of symmetry of geometry and loading about the crack plane and the through thickness mid-plane, only a quarter of the specimen was modelled with 15158 elements (with 14300 nodes), as shown in Fig. 8-7. There were six layers of elements in the thickness direction, and in the direction of crack path, the minimum element size was 0.4 mm. The cohesive interfaces were modelled by 870 eight-noded cohesive zone elements (refer to Fig.8-3), and they were manually inserted in the plane of anticipated crack growth, as indicated by the displacement constraint. The top nodes of the cohesive zone elements are the bottom nodes of the bulk elements, and the displacement constraints are applied to the bottom nodes of the cohesive elements. Prescribed displacement was applied along the plane of the pin (not modelled here) in the CT specimen, at the top surface, as indicated in Fig.8-7. CT specimens with two thicknesses, 6 mm and 12 mm, were considered, and these are denoted CT6 and CT12, respectively, in the following discussion.

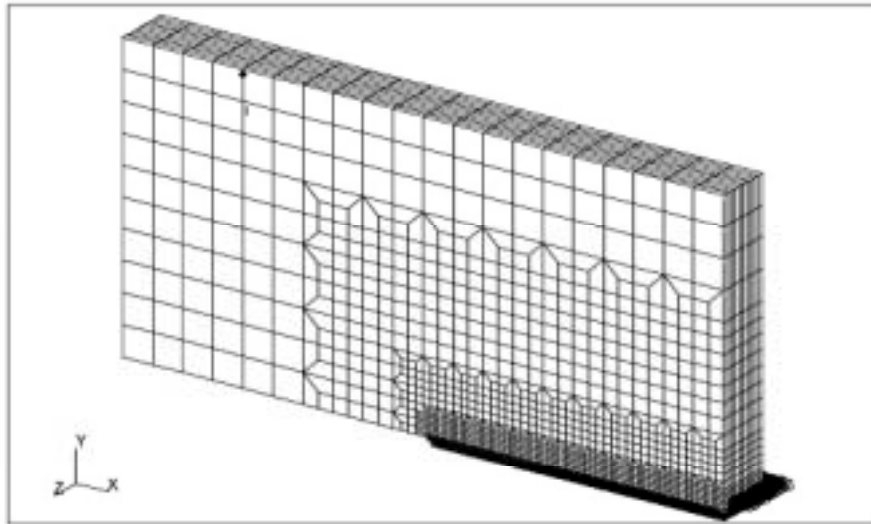


Fig. 8-7 Finite element mesh for CT specimen. The displacement constraint symbols indicate the location of the cohesive elements.

9. Results of Numerical Analysis

9.1 Simulation of Stable Tearing by ZENCRACK

At the initial stage of this study, ZENCRACK was used to simulate the behaviour of stable tearing during cyclic loading. The intention was to evaluate ZENCRACK's capability in modelling stable tearing or crack jumping. The numerical results were compared with the results generated by a standard compact tension (CT) specimen.

9.1.1 Basic Model

The basic finite element (FE) mesh developed to model the CT specimen is shown in Fig.9-1 for 24 mm thickness. The model was supported by constraining three degrees of freedom at the top and bottom edges as shown. These constraints allowed displacement of the model in the x-direction along the height of the specimen and represent a typical restraint set up for a standard test specimen. All elements for this case had identical material properties including those that were replaced by crack block elements. The resulting mesh after the crack-blocks was inserted is shown in Fig.9-2, where elements 21 and 22 were replaced by crack blocks. The material properties are given in Table 2-2. The CT specimen geometry is given in Fig.2-2. A single distributed load is applied to the outer face of the elements to represent the test conditions. The value of the applied load is varied depending on the requirements of the test case under investigation but its position remains constant.

In the initial study, different stress states, i.e. plane strain, plane stress and combinations of the two, were examined in order to capture the relevant behaviour. Different levels of applied loads were investigated. A linear static analysis and a simple elastic constitutive model for the material were used, whilst the third was solved using a non-linear static analysis with a perfect-plasticity constitutive model. The applied load was based on some of the work reported in a DSTO report (Hu et al, 1999). The load magnitude range was between 25 to 413 MPa.

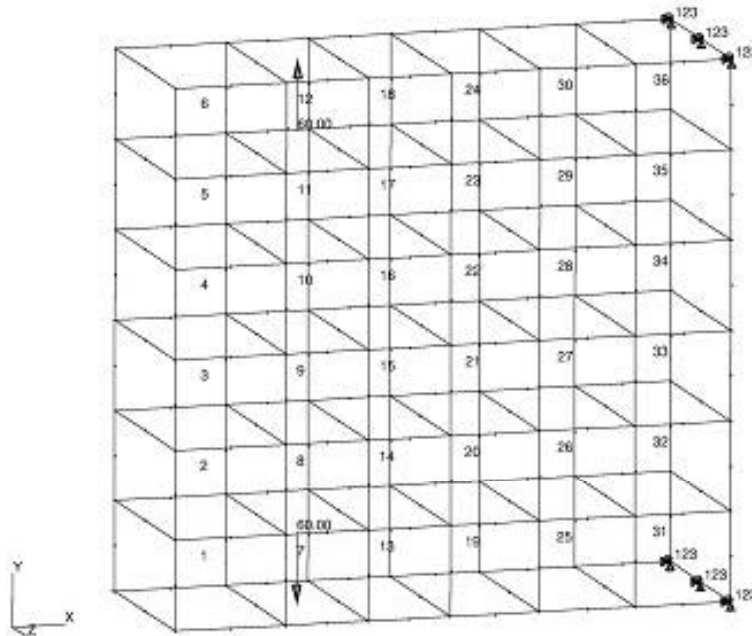


Fig.9-1 Basic finite element model for a CT specimen with 24 mm thickness.

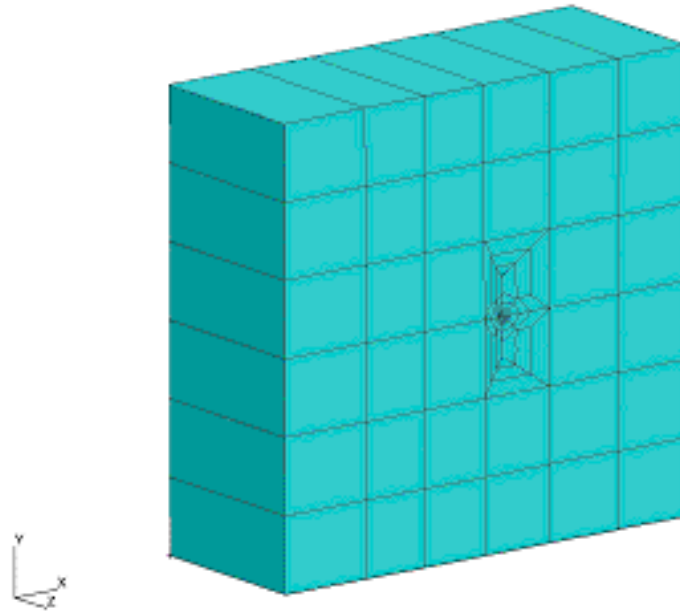


Fig.9-2 Schematic of a ZENCRACK 3D Model for simulating stable tearing in a 24 mm thick CT specimen.

9.1.2 Simulations of Crack Profiles

In this study, ZENCRACK was used in a standard fashion by implementing a known crack growth law, that is, the Paris law (refer to Eq. 7-5), from the experimental data of 7050Al CT specimens (Fig.9-3) in order to simulate tearing behaviour, applying a representative fatigue load spectrum (Fig.9-4). The curved crack front profiles were created and the stress intensity factors were calculated. The finite element solver used was ABAQUS. The numerical analysis was divided into several steps. Each step was performed by setting a desired number of load steps (in this case, one per step).

The numerical results of the test cases for plane strain conditions are plotted in Fig.9-5 and Fig.9-6. Fig. 9-5 shows the crack front profiles during fatigue crack growth under elastic conditions. Under an elastic-plastic condition, the crack growth was simulated until failure, as shown in Fig.9-6.

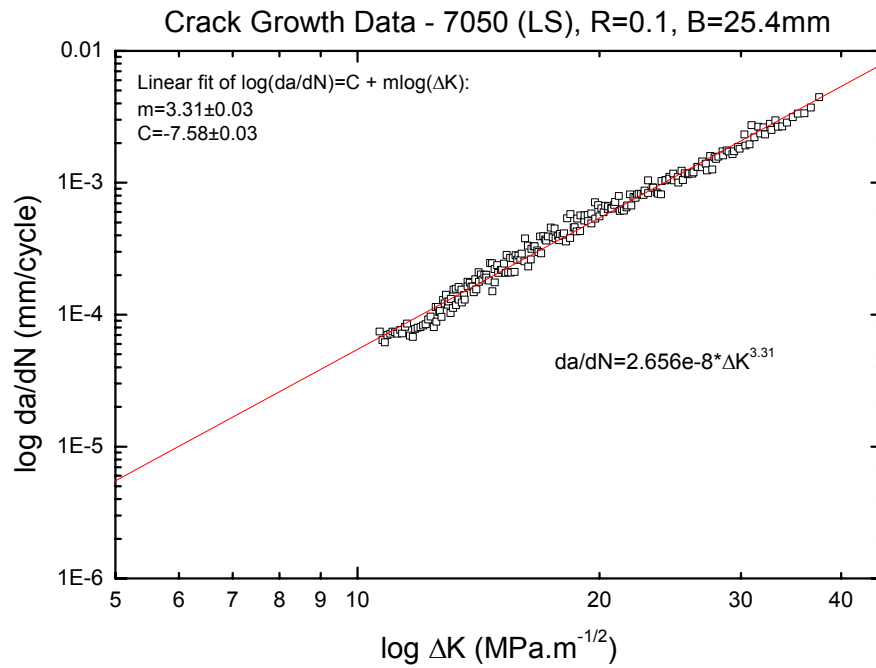


Fig. 9-3 Fatigue crack growth data for compact tension (CT) test specimen of 7050 Al

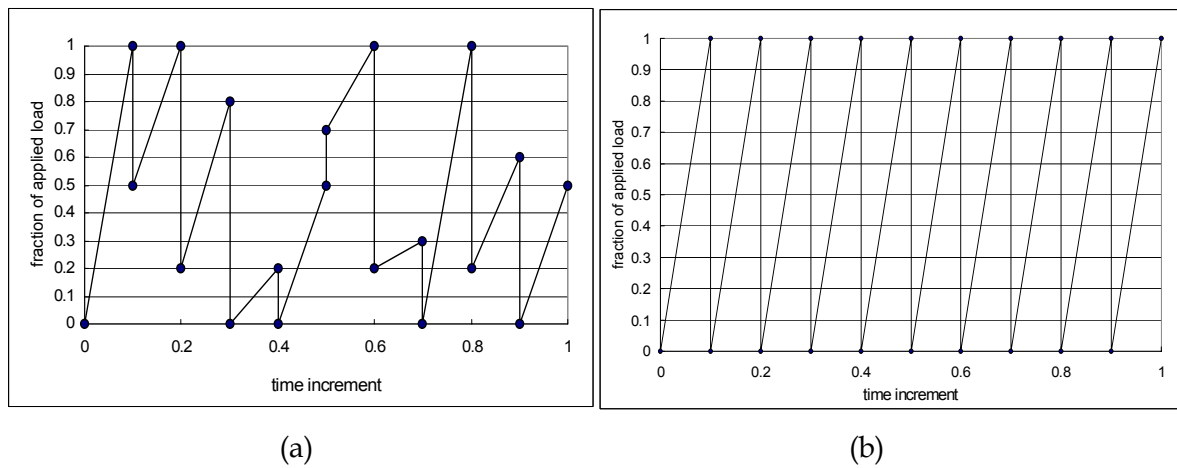


Fig.9-4 Applied load spectra for ZENCRACK evaluation. (a) Variable load amplitude and (b) Constant load amplitude.

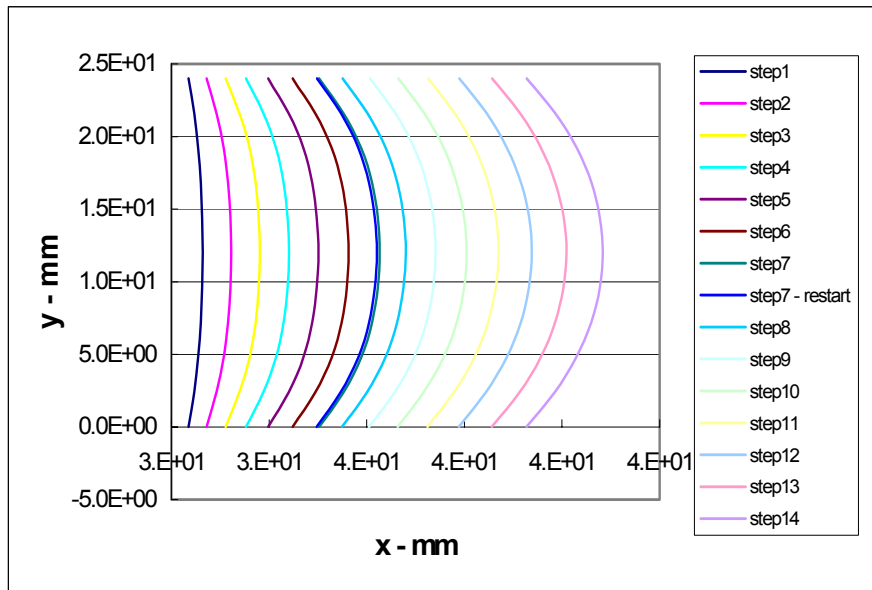


Fig.9-5 Simulated crack front profiles during fatigue crack growth under an applied load of 30 MPa (variable amplitude) for 24 mm CT specimen.

For plane stress and combination conditions, the 12 mm thick CT specimen was considered. Fig.9-7 and 9-8 give examples of crack front profiles during simulated crack growth under elastic and elastic-plastic conditions, respectively. Similar crack profiles were obtained for constant amplitude loading.

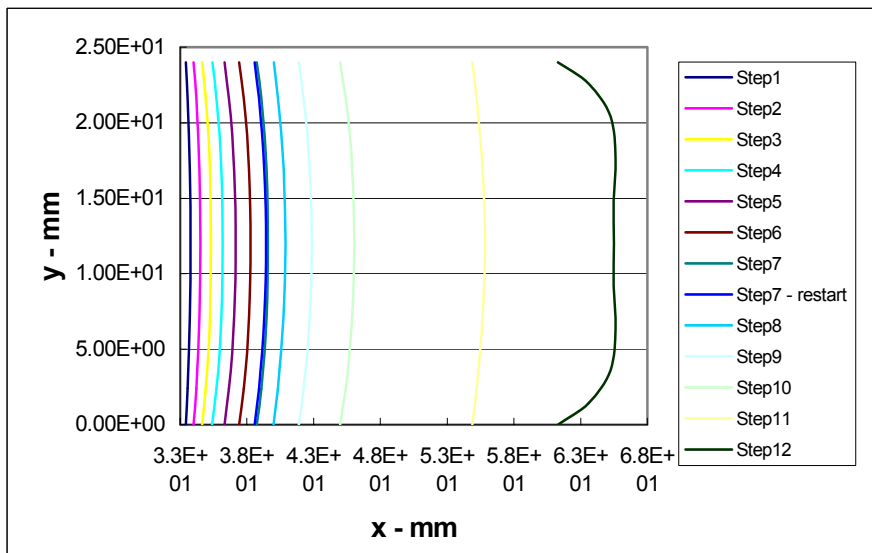


Fig.9-6 Simulated crack front profiles during fatigue crack growth under an applied load of 300 MPa (variable amplitude) for 24 mm CT specimen

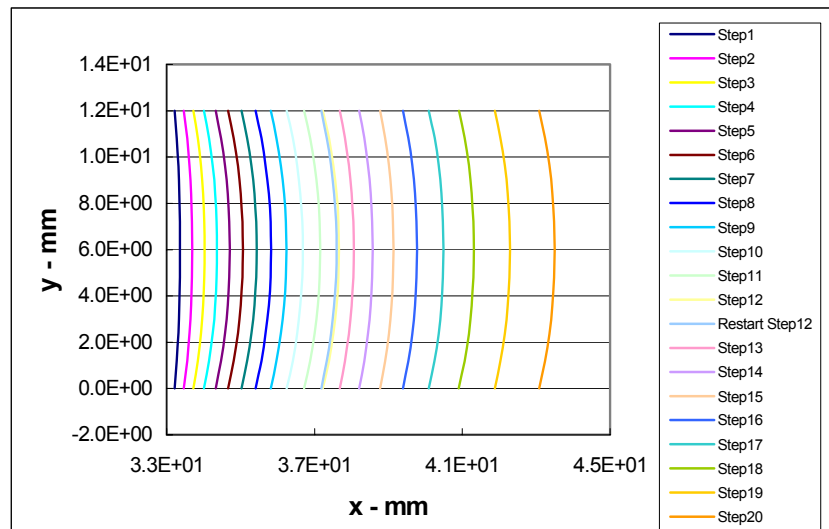


Fig.9-7 Simulated crack front profiles during fatigue crack growth under an applied load of 25 MPa (variable amplitude) for 12 mm CT specimen

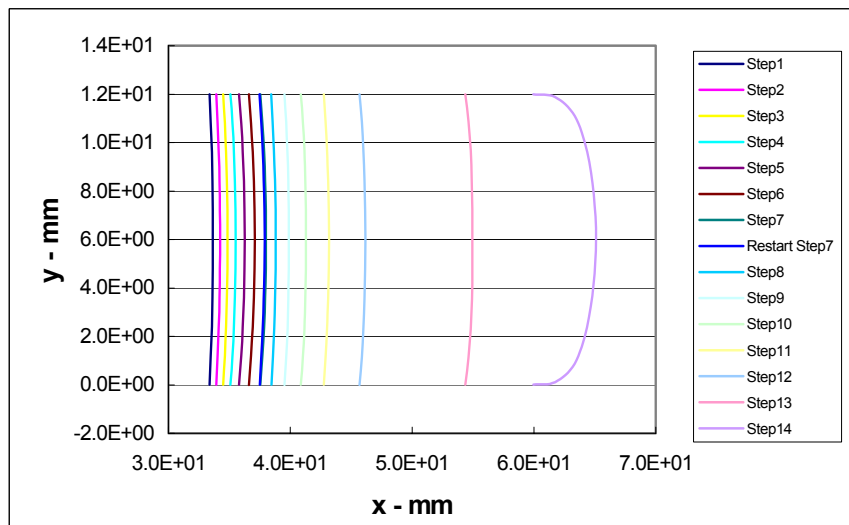


Fig.9-8 Simulated crack front profiles during fatigue crack growth under an applied load of 300 MPa (variable amplitude) for 12 mm CT specimen

9.1.3 Simulation of Stable Tearing

To assess the ability of ZENCRACK to model stable tearing, a model representative of the CT geometry was considered. The model, subjected to constant amplitude loading of 0.8 to 8.0 kN, was used as a reference case. The specimen experienced crack growth

to a total crack length of 27 mm. At this point a single overload of 24.33 kN was applied causing the specimen to fail. The resulting maximum stress intensity factor, K_{max} , was 48 MPa√m. This information is used to validate the ZENCRACK stable tearing model.

To simulate the CT specimen results the approach was to consider the ZENCRACK analysis as consisting of two major components – the first being fatigue crack growth up to the point of $a = 27$ mm, followed by the application of an overload using a non-linear analysis in ABAQUS. The fatigue crack growth stage was further broken down into growth from $a = 20.3$ mm to 26.3 mm (6mm growth) followed by growth from 26.3 mm to approximately 27 mm. This approach requires two restarts and two separate FE models. The models applied to the plane strain tests were used and all dimensions, properties, materials, etc., were identical.

The simulation of stable tearing was successful in that the general behaviour of the CT specimen was duplicated, as shown in Fig.9-9. However, the numerical results could not quantitatively reproduce the results, which were obtained from the experimental tests (Byrnes, et al, 2000).

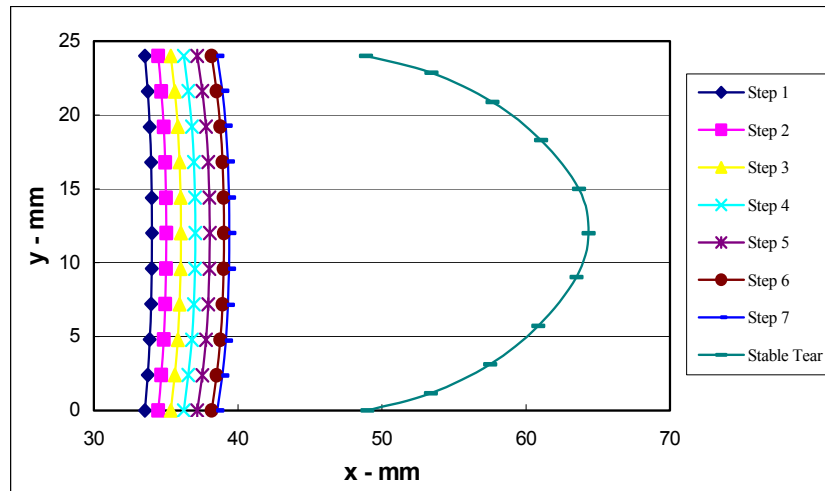


Fig. 9-9 Stable tearing case crack front profiles by ZENCRACK.

9.2 Stress Distribution in a CT Specimen by ZENCRACK

For comparison, in a plot of stress intensity factor (SIF), the SIF distribution in a straight crack front (i.e. the curvature is 0%- refer to Fig.7-8) was included as the baseline for each condition.

9.2.1 A CT Specimen with 6 mm Thickness

The 6 mm thickness model contained one element through the thickness, which allowed the SIF variation to be plotted at six locations through the thickness.

Two overload cases were run. Crack curvatures of 24.02% and 43.66% were generated. The SIF distribution through the thickness of the specimen for the 24.02% curvature case is shown in Fig.9-10. This result indicated that the SIF at the mid-section was more or less uniform and the highest value was at free specimen surfaces. However, with an increase in the curvature to 43.66%, the lowest SIF occurs at the centre and the SIF distribution was not uniform at the mid-section of a specimen, as shown in Fig.9-11.

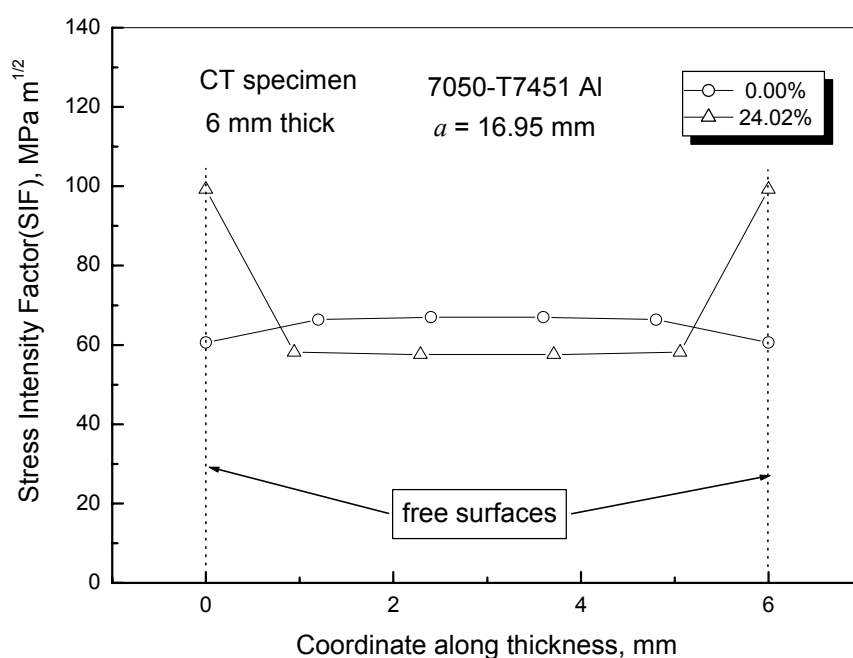


Fig.9-10 Distribution of stress intensity factor along the crack front in a 6 mm CT specimen for a given initial crack length, $a = 16.95$ mm. The curvature is 24.02%.

9.2.2 A CT Specimen with 12 mm Thickness

The 12 mm thickness model contained two through thickness elements. Two overload cases were run for this model. Crack curvatures of 15.45% and 27.69% were generated. The SIF variation for the 15.45% case is shown in Fig.9-12. ZENCRACK predicted the lowest SIF for the curved crack front would occur about 2 mm from the free surface of the specimen. The highest SIF occurred at the free surface of the specimen for the curved crack front. Similar results can be seen in Fig.9-13 for the 27.69% curvature case.

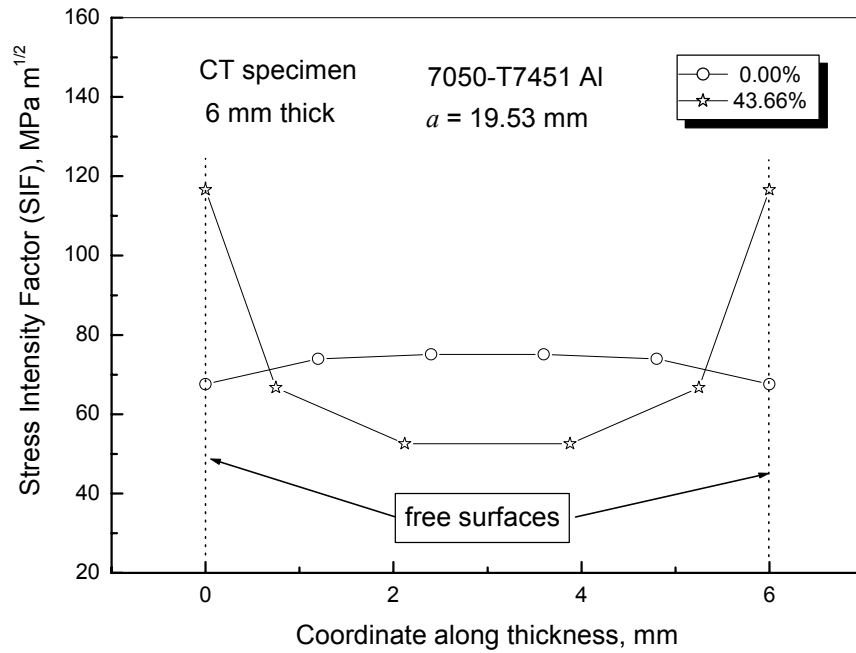


Fig.9-11 Distribution of stress intensity factor along the crack front in a 6 mm CT specimen for a given initial crack length, $a = 19.53$ mm. The curvature is 43.66%.

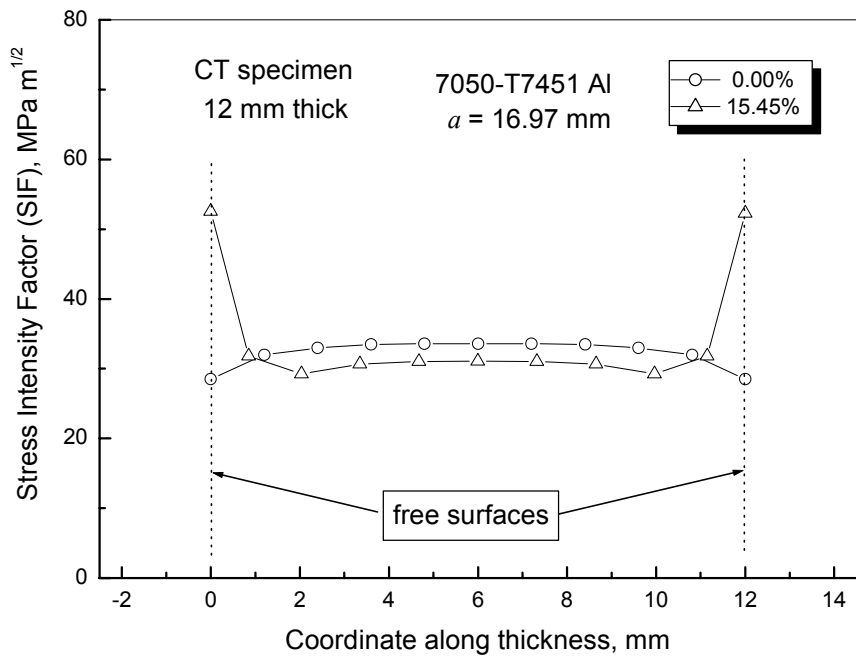


Fig.9-12 Distribution of stress intensity factor along the crack front in a 12 mm CT specimen for a given initial crack length, $a = 16.97$ mm. The curvature is 15.45%.

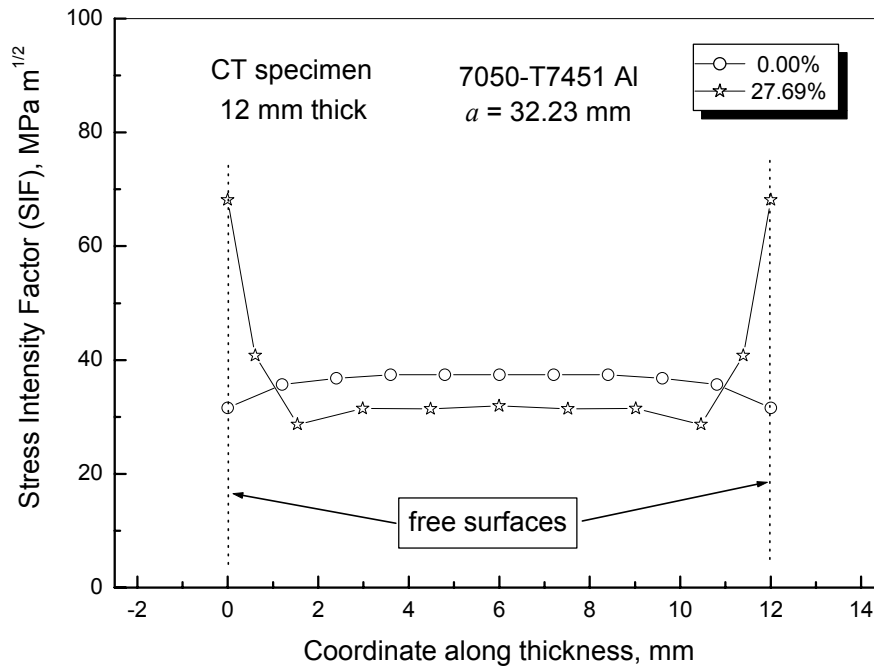


Fig.9-13 Distribution of stress intensity factor along the crack front in a 12 mm CT specimen for a given initial crack length, $a = 32.23$ mm. The curvature is 27.69%.

9.2.3 A CT Specimen with 24 mm Thickness

As mentioned in Sec.7.4, the 24-millimetre model contained two through thickness elements. These elements allowed the SIF variation to be plotted at 11 locations through the thickness. Two overload cases were run for this model. Crack curvatures of 8.55% and 17.47% were generated. The SIF variation for the 8.55% case is shown in Fig. 9-14. Due to the lower curvature, the predicted SIF profile is similar to that from a straight crack case (i.e. 0% curvature), except for SIFs near the free surfaces. At an increased curvature, e.g. 17.47%, the difference between the curved crack and the straight crack is increased. Also the SIF at the free surfaces is much higher at the free surface than those at the centre, as shown in Fig. 9-15.

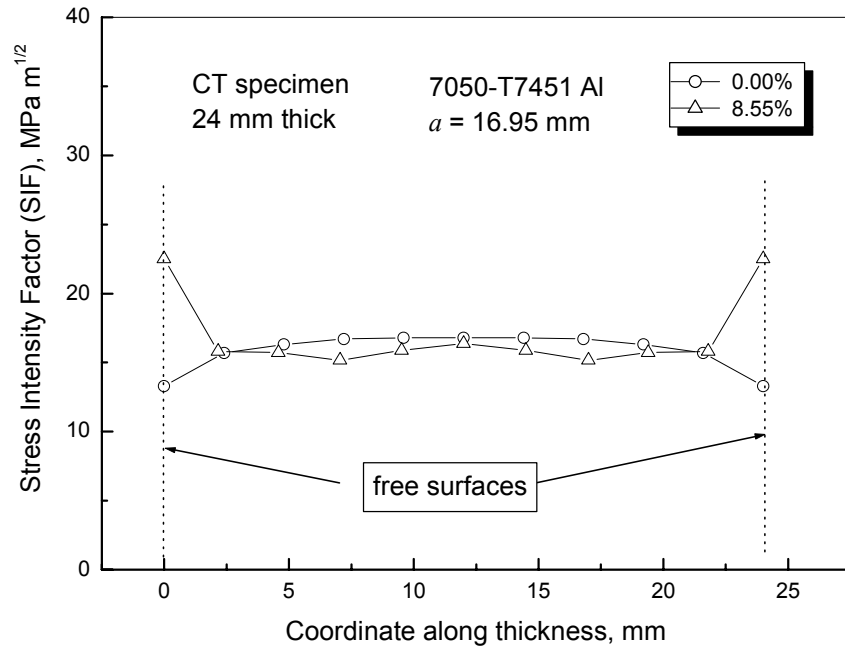


Fig.9-14 Distribution of stress intensity factor along the crack front in a 24 mm CT specimen for a given initial crack length, $a = 16.95$ mm. The curvature is 8.55%.

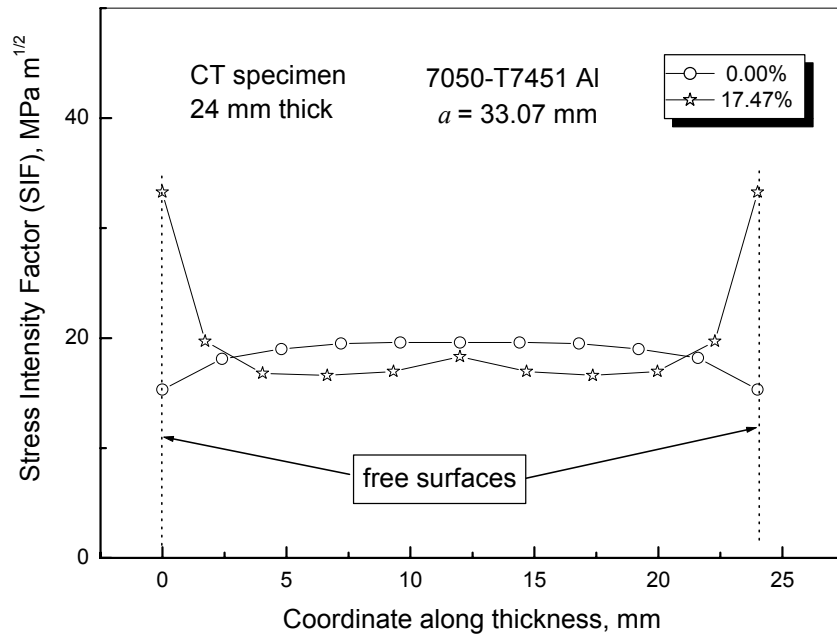


Fig.9-15 Distribution of stress intensity factor along the crack front in a 24 mm CT specimen for a given initial crack length, $a = 33.07$ mm. The curvature is 17.47%.

The SIF variations along the crack front during crack growth for different crack profiles are shown in Fig. 9-16. The trend in SIFs as the crack grows is indicated by the arrows. Fig. 9-16 clearly shows that the SIF on the surface of the specimen reduces as the crack grows. This occurs until the crack front at the surface has 'caught up' to the crack front at the centre, at which points the SIF at the surface and the centre increases due to the increasing crack length.

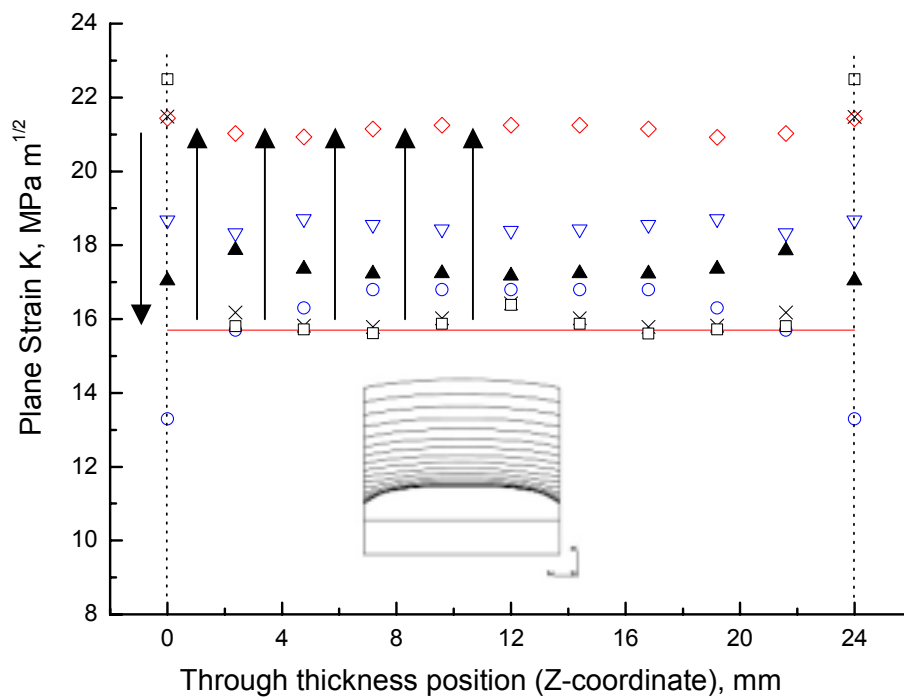


Fig.9-16 SIF variations in a 24 mm CT specimen started with 8.55% curvature during crack growth (0% curvature is for straight crack front case as reference). Symbol — is the theoretical K value; ◇ with 4.01%; ▽ with 4.10%; ▲ with 4.36%; × with 7.75%; □ with 8.55% and ○ with 0% curvature.

The SIF at the centre of the specimen showed very little change until the crack front at the surface has caught up and then SIF increased due to the increased crack length. It can also be seen for crack front positions 11 onwards that the stress intensity factor through the thickness is nearly uniform. This means that crack growth will be similar at all positions along the crack front and the current curvature value will be maintained during crack growth.

9.3 Stress Distributions in a CCT Specimen by ZENCRACK

In the CCT specimen, three thicknesses were modelled: 3, 6 and 9 mm. Two types of crack profiles were investigated: (i) Straight crack front and (ii) a curved crack front with different curvatures, where the result from the straight crack front was used as the baseline.

9.3.1 A CCT Specimen with 3 mm Thickness

For demonstration, two analyses were undertaken for the 3-millimetre model. Crack curvatures of 10.67% and 27.44% were generated. The SIF distribution for the curvature 10.67% is shown in Fig.9-17. The SIF was slightly higher at the mid-section than near the free surfaces but the highest SIF was at the free surfaces. With increased curvature (i.e from 10.67% to 27.44%), the SIF distribution at the mid-section was more uniform, as shown in Fig.9-18. The results indicate that a plane strain state was still dominant in a CT specimen, even for a thinner specimen. Compared to the straight crack front, the value of the SIF at the mid-section became lower with the increase in crack curvature. In other words, the absolute SIF difference between the mid-section and the free surface increased.

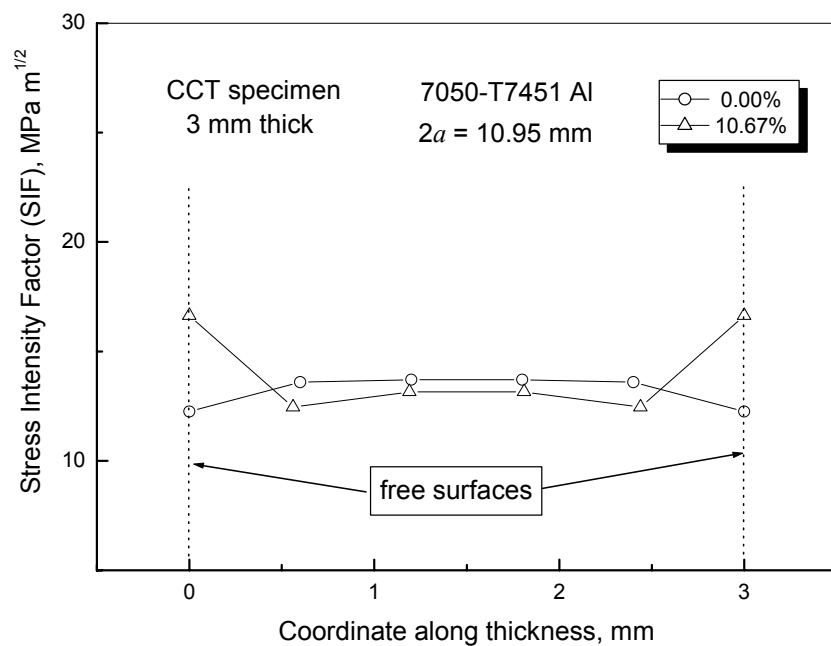


Fig.9-17 Distribution of stress intensity factor along the crack front in a 3 mm CCT specimen for a given initial crack length, $a = 10.95$ mm. The curvature is 10.67%.

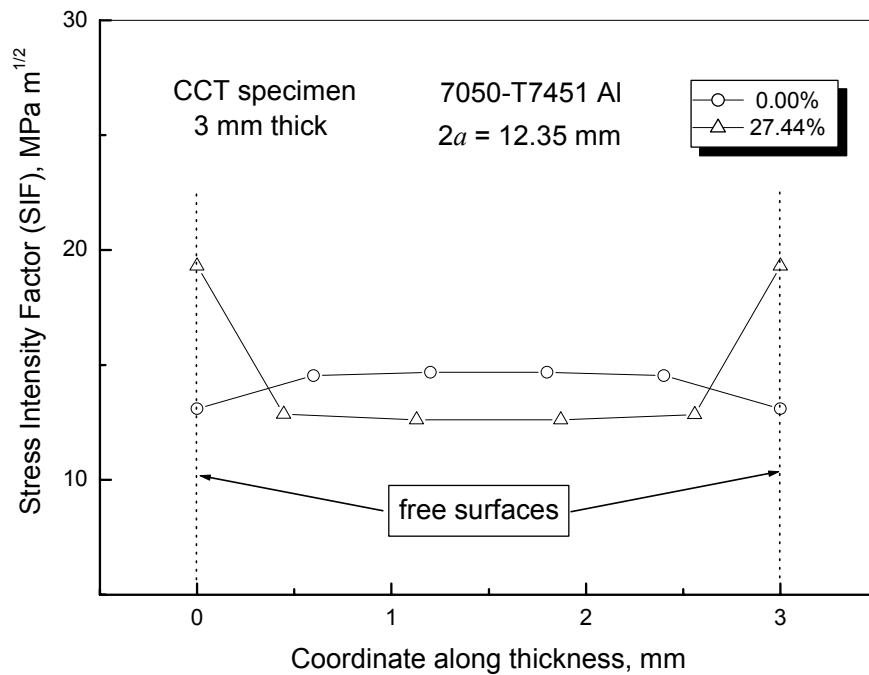


Fig.9-18 The distribution of stress intensity factor along the crack front in a 3 mm CCT specimen for a given initial crack length, $a = 12.35$ mm. The curvature is 27.44%.

9.3.2 A CCT Specimen with 6 mm Thick

Two analyses were performed for the 6 mm model. Crack curvatures of 4.86% and 12.04% were generated. The SIF factor distribution for the 4.86% curvature case is shown in Fig.9-19. This figure shows that the shape of the SIF distribution resembles the letter W. At a crack curvature of 12.04%, the letter “W” shape of the SIF distribution becomes more obvious (Fig.9-20). Compared to the straight crack, at the centre, the SIF value was same.

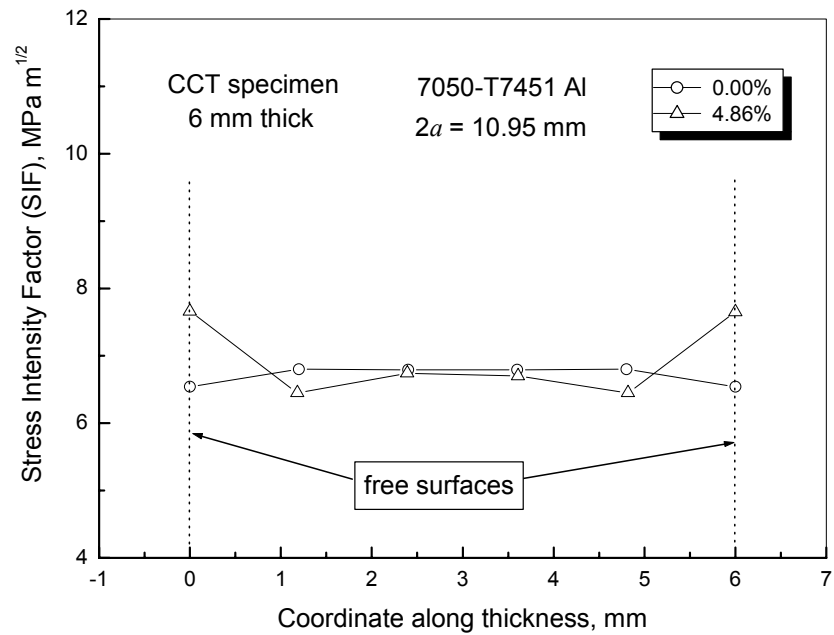


Fig.9-19 Distribution of stress intensity factor along the crack front in a 6 mm CCT specimen for a given initial crack length, $a = 10.95$ mm. The curvature is 4.86%.

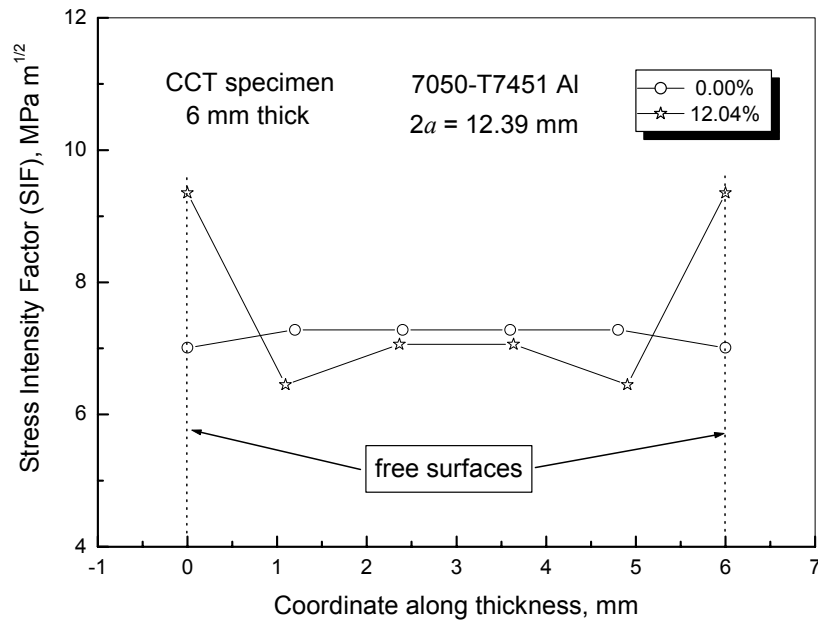


Fig.9-20 Distribution of stress intensity factor along the crack front in a 6 mm CCT specimen for a given initial crack length, $a = 12.39$ mm. The curvature is 12.04%.

9.3.3 A CCT Specimen with 9 mm Thickness

Two analyses were undertaken for the 9 mm model. Crack curvatures of 7.13% and 11.5% were generated. The SIF distributions for both curvatures are similar to those in thickness of 3 and 6 mm cases, as shown in Fig.9-21 and Fig.9-22.

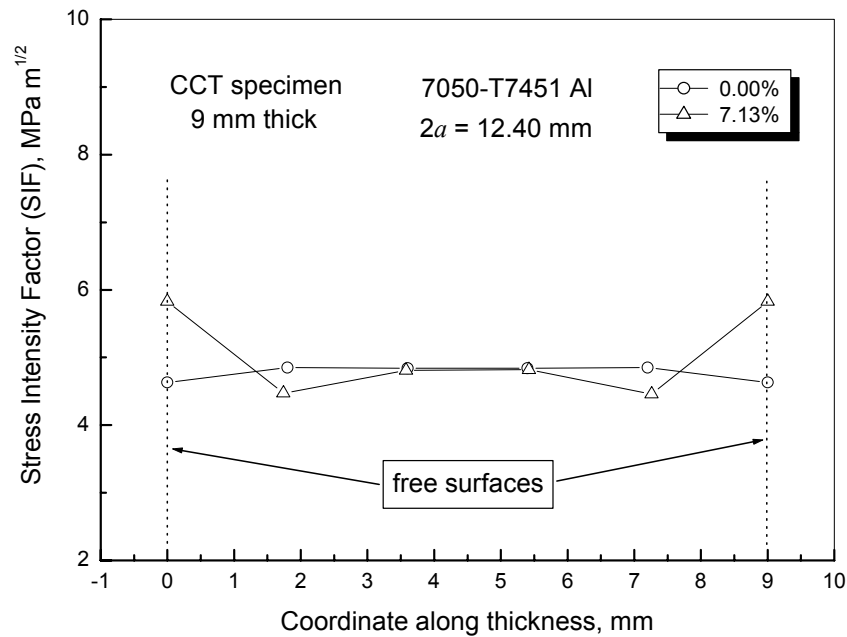


Fig.9-21 Distribution of stress intensity factor along the crack front in a 9 mm CCT specimen for a given initial crack length, $a = 12.40$ mm. The curvature is 7.13%.

Fig.9-23 shows the SIF variations for other crack front profiles during crack growth in a CCT specimen with 9 mm thickness. The trend in the SIF with crack growth is shown by arrows in Fig.9-23. The SIF on the surface of the specimen reduces as the crack grows, until the crack front at the surface has 'caught up' to the centre crack front position, so that the crack front resembles a crack front of normal curvature at which point the SIF at the surface increases due to the increasing crack length.

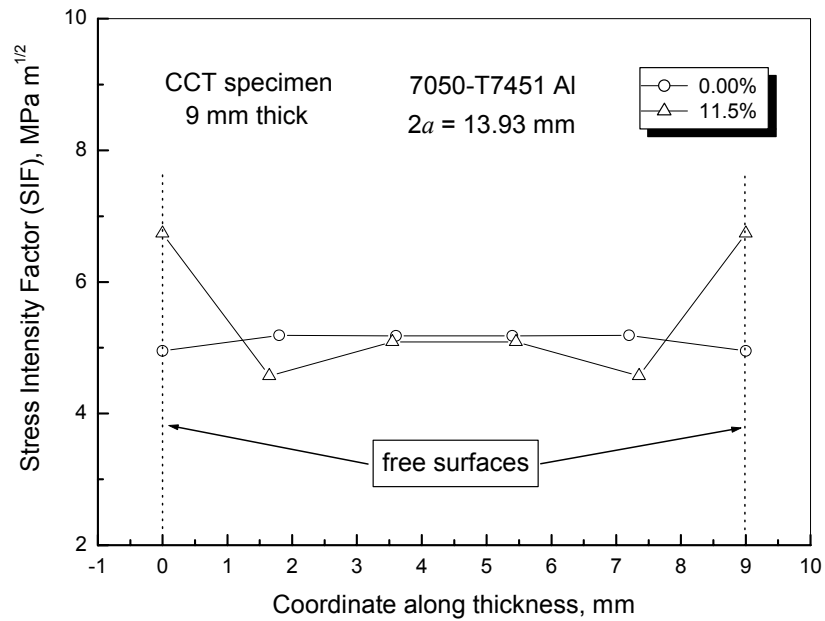


Fig.9-22 Distribution of stress intensity factor along the crack front in a 9 mm CCT specimen for a given initial crack length, $a = 13.93$ mm. The curvature is 11.5%.

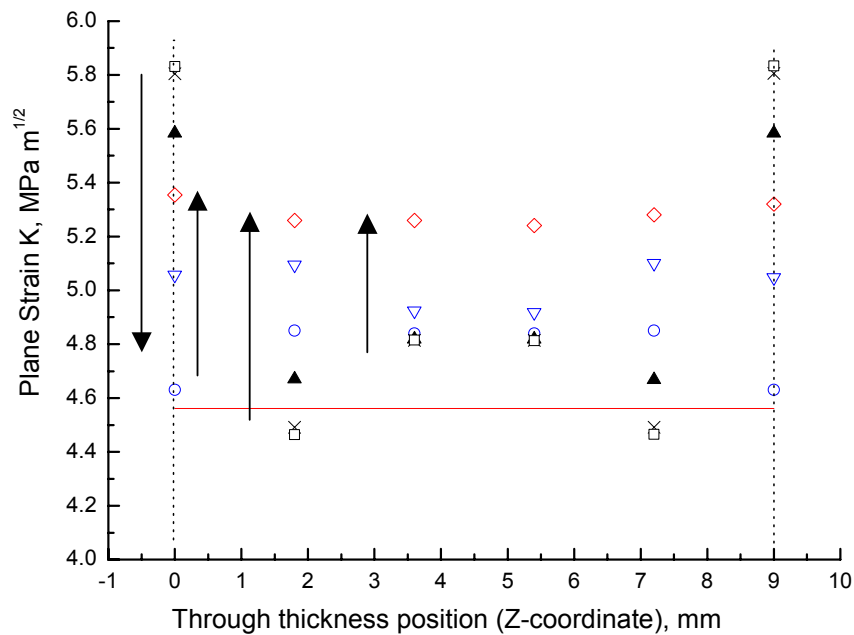


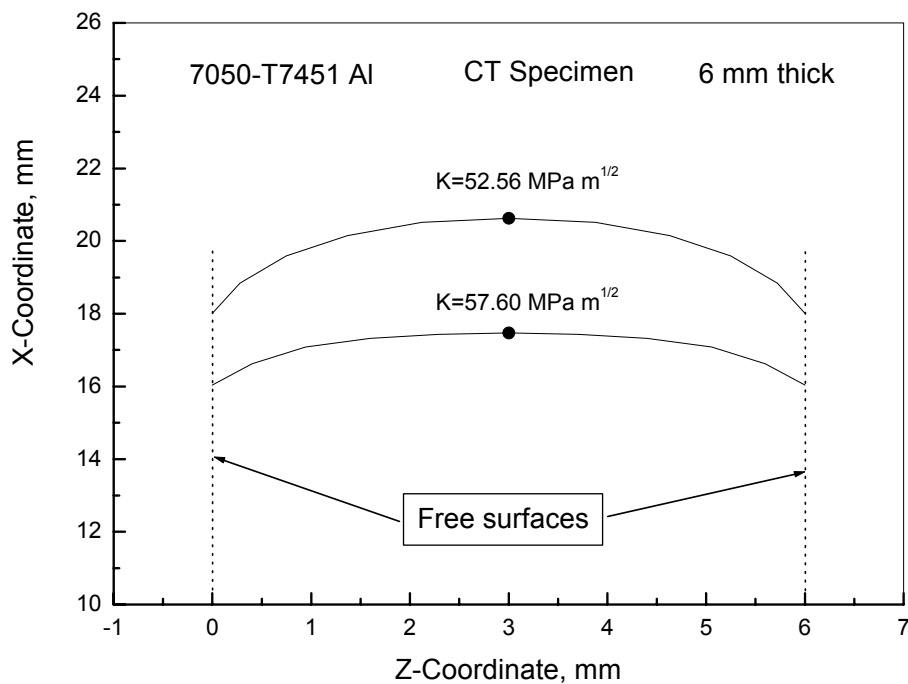
Fig.9-23 SIF variations in a 9 mm CCT specimen started with 7.13% curvature during crack growth (0% curvature is for straight crack front case as reference). Symbol — is the theoretical K value; ◇ with 1.74%; ▽ with 2.38%; ▲ with 5.38%; × with 6.90%; □ with 7.13% and ○ with 0% curvature.

9.4 Effect of Crack Tip Front Shape by ZENCRACK

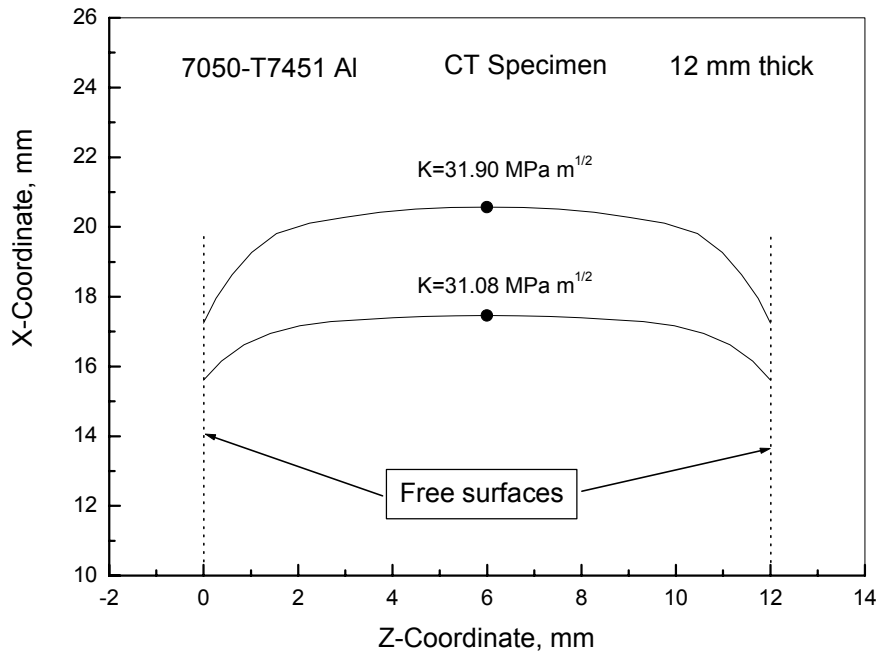
9.4.1 Under Elastic Condition

The numerical results show that the stress distribution is strongly dependent on the crack front shape. However, the SIFs variations at the middle-section of a specimen thickness remain small for the same thickness of a CT specimen and different curvatures, as shown in Fig. 9-24. With an increase in thickness, the SIF at the middle-section is reduced.

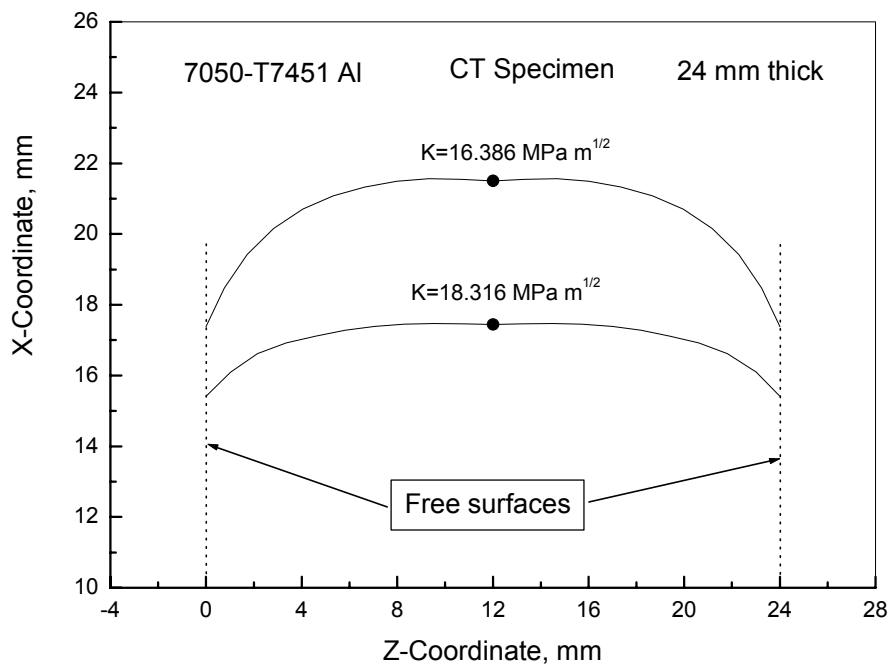
Similar result was also found in a CCT specimen, as shown in Fig. 9-25. But, the variations are smaller in the CCT specimen (refer to Fig.9-21), compared to the CT specimen. This may imply that SIFs may remain roughly constant at the onset and end of the stable tearing. Also, the thickness had a small effect on the values of SIFs at the middle-section.



(a)

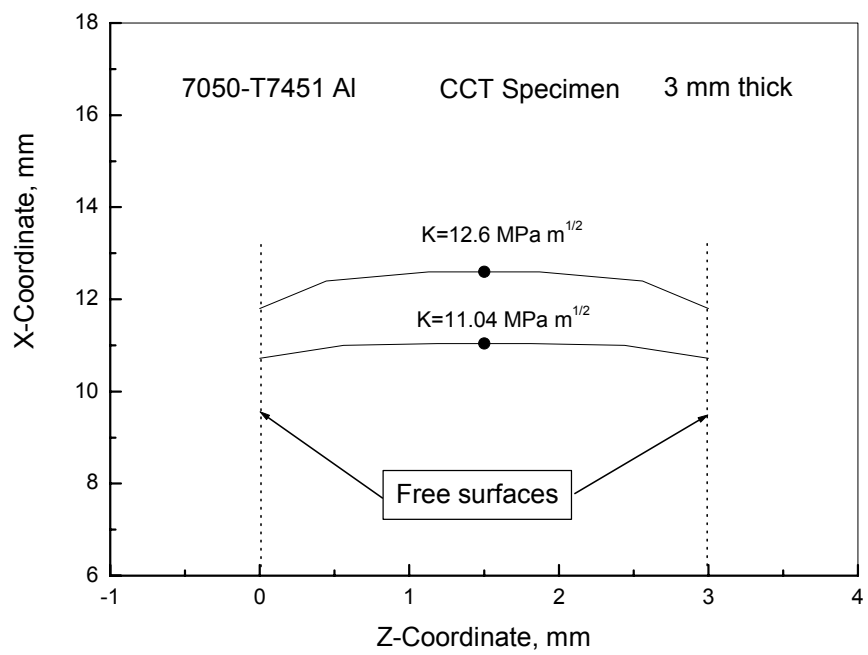


(b)

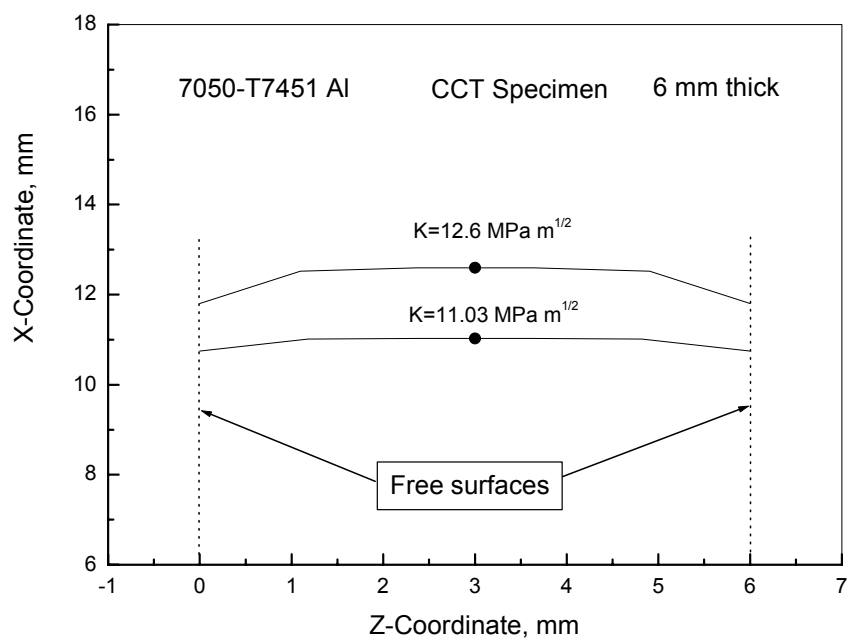


(c)

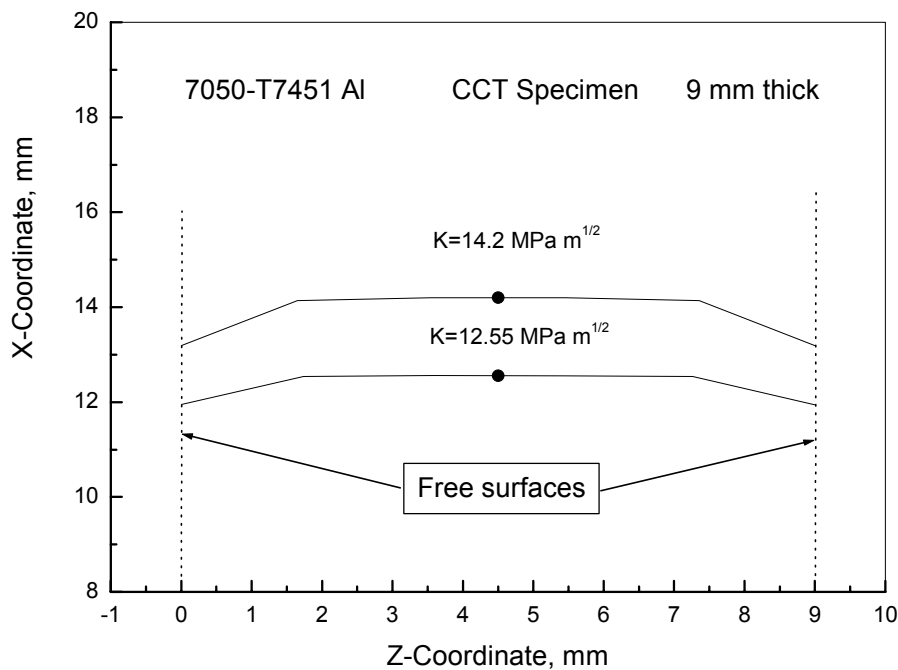
Fig.9-24 Crack front positions at mid-sections and corresponding SIFs at different curvatures and thicknesses in CT specimens. (a) 6 mm; (b) 12 mm and (c) 24 mm.



(a)



(b)



(c)

Fig.9-25 Crack front positions at mid-sections and corresponding SIFs at different curvatures and thicknesses in CCT specimens. (a) 3 mm; (b) 6 mm and (c) 9 mm.

However, although two crack curvatures were plotted together, it does not automatically mean that these are the crack front shapes at the onset and end of the stable tearing. At the moment, ZENCRACK cannot give reasonable changes of crack shapes at the onset and end of the stable tearing, because of lack of suitable criteria for the “jump” (onset) and “arrest” (end).

Except for the application of ZENCRACK code, ABAQUS code alone was also used to directly build a 3D model for calculating stress distributions along crack tip fronts in the initial stage of this study. Fig.9-26 shows the numerical results under different crack curvatures. Similar results to those from ZENCRACK (refer to Secs.9.2 and 9.3) can be seen, that is, the highest SIFs exist at free surfaces and the lowest SIFs are at a mid-section. However, the numerical results from ABAQUS alone did not give the “W” shape of SIF distribution by ZENCRACK. It is not clear why the differences occur. It could be related to both numerical calculation methods. In ZENCRACK, the crack block is used while ABAQUS does not use it.

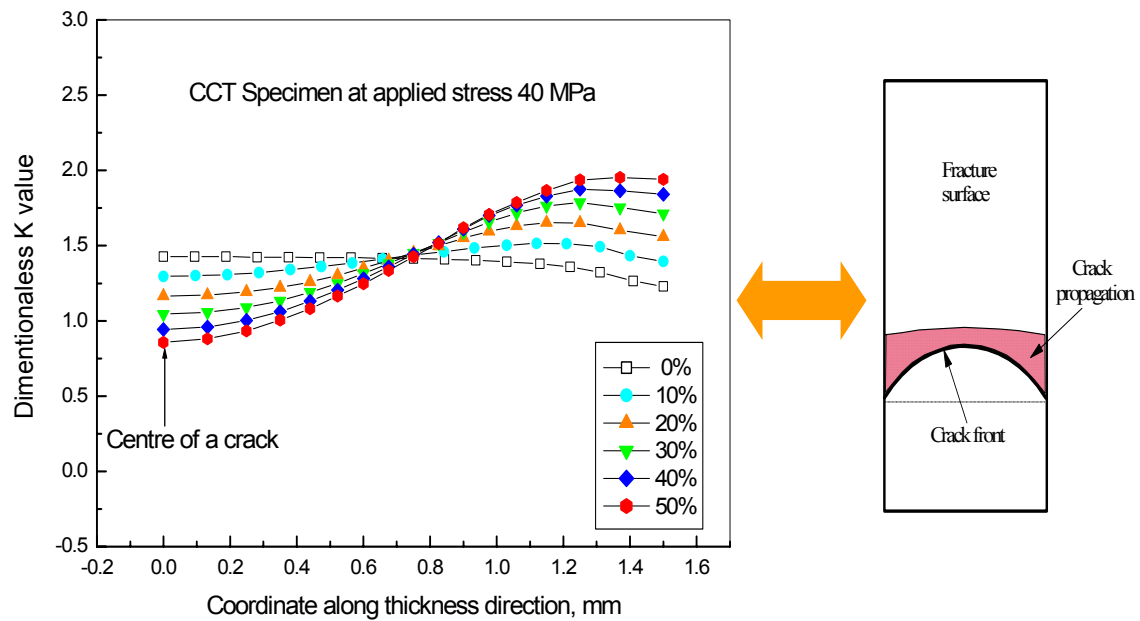


Fig.9-26 Dimensional stress intensity factors as a function of the curvature along the crack tip front at the applied stress 40 MPa (elastic state) by using ABAQUS.

9.4.2 Under Elastic-Plastic Condition

Fig.9-27 shows the stress distributions at Z-direction (crack opening) along the crack tip front at the applied stress of 400 MPa for different crack curvatures. At the 0% curvature, the high stress is dominant at the mid-section of a specimen and lower stress appeared at free surfaces. With increasing the curvature, higher stress spread into the subsurface areas. At the 50% curvature, the plane strain stress was almost along the whole crack front and its distribution also became relatively uniform.

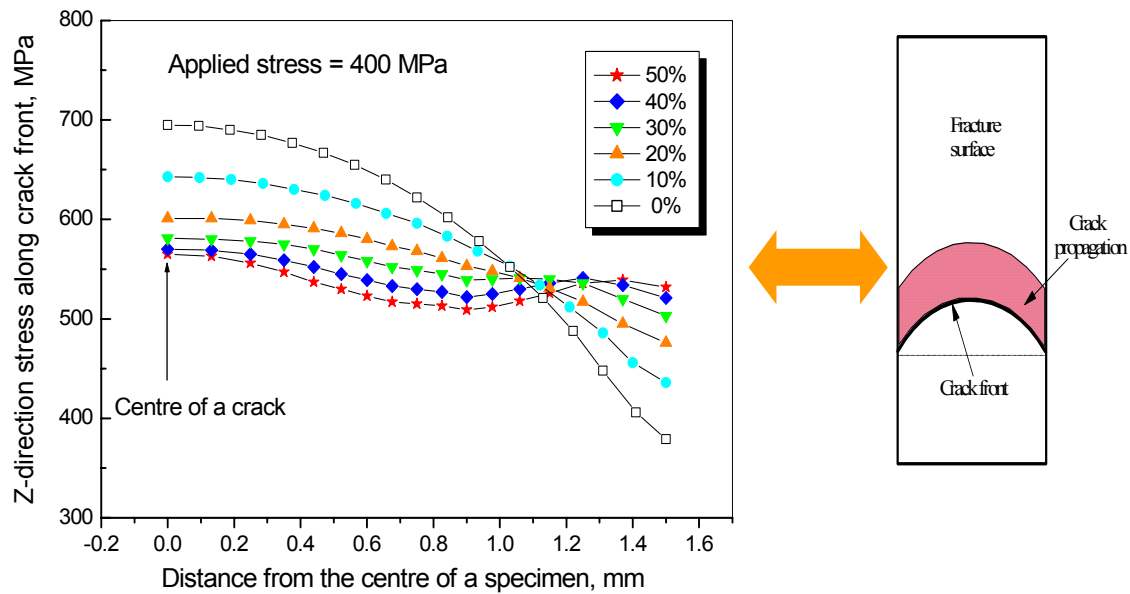


Fig.9-27 Stress distributions at Z-direction (crack opening) as a function of the curvature along the crack tip front at the applied stress of 400 MPa (elastic-plastic state).

9.5 Preliminary Numerical Results by CZM

The cohesive zone model (CZM) was used to simulate stable tearing in order to avoid the lack of a local criterion. At the moment, the simulation was carried out only under static loading conditions.

To examine the through-thickness crack growth behaviour, we define two lines or nodes in the crack plane, the 'centre line' and the 'surface line', which are the projections of the z-symmetric plane and the surface, respectively, on the crack plane. In the following, the crack front is defined by the point where the vertical displacement (separation) reaches $v = 5.7\delta_c/2$, as suggested in (Gullerud, et al, 2002). The factor 2 was necessary because the vertical displacement only represents half of the separation between the upper and the lower crack faces. Spline curve-fitting was initially used to determine the crack front, but calculation shows that a linear interpolation gives almost the same results.

Evidently, the crack propagation first started at the centre line where the stress state is closer to that of the plane strain, as shown in Fig. 9-28 in which the crack extension at the centre line and the surface line are plotted against the load-point displacement. With respect to the load-point displacement, the crack on the centre line has a much higher initial rate of propagation than that on the surface line where the stress state approaches that of plane strain. This difference in the initial rate of propagation results in the experimentally observed tunnelling effect. It is worth noting that after some

propagation, the cracks on the two lines attained similar growth rates, indicating the stabilization of the shape of the crack front. Disregarding the plastic stress state during fatigue crack growth, these results may serve as an approximate prediction of the change in the shape of the crack front that would occur under fatigue loading.

Fig.9-29 and Fig.9-30 show contour plots of the crack face displacement for the CT6 (6 mm thick) specimens, demonstrating stable tearing-like behaviour (i.e. tunnelling). Similar behaviour was observed for the CT12 (12 mm thick) specimens, as shown in Fig.9-31. Indeed, these contour plots do correlate well with the experimental data, for example, as shown in Figs.1-1 and 3-4, albeit qualitatively.

In Fig.9-29, the crack face separation was plotted at load increment 500, with a crack extension of approximately 7.8 mm, where z is thickness direction and x crack propagation direction. The shape of the contour indicates the variation of curvature of the crack face along the crack length. The contours in Fig.9-30 show the shape of the crack front at different stages of crack extension. The dashed line represents the shape of the crack front when the crack has just started to propagate, showing the least tunnelling effect. This is because at crack initiation there is little plastic deformation. In the subsequent stages of crack extension, the tunnelling effect intensifies because of the rapid development of a plastic zone at the surface layer, as indicated by the dash-dotted line and the long-dashed lines (representing the crack front at $\Delta a_c = 3.75$ mm and 6.96 mm, respectively). The solid line shows the crack front when $\Delta a_c = 7.8$ mm.

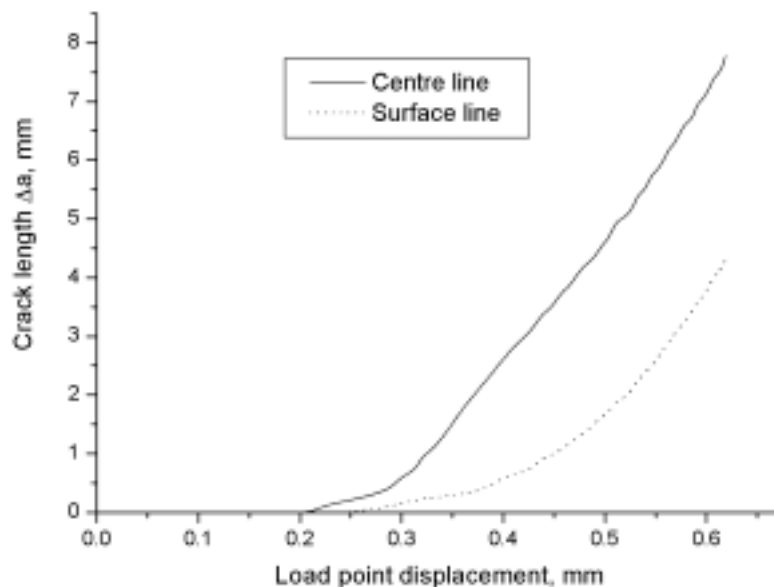


Fig. 9-28 Crack length versus load-point displacements on the surface and the centre of a CT specimen.

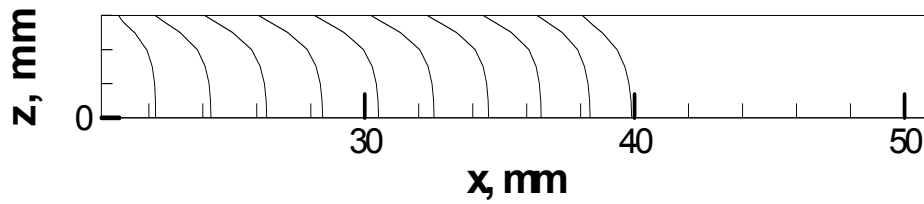


Fig.9-29 Contour plot showing the crack face displacement at load step 500 for a CT specimen with 6 mm thick (CT6).

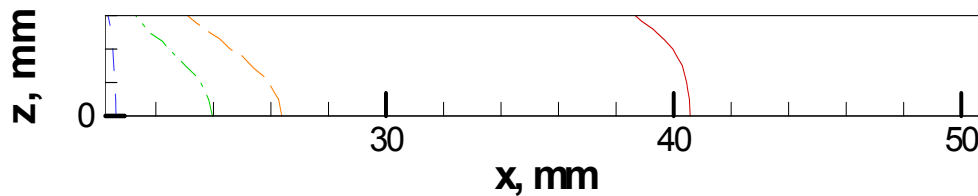


Fig.9-30 Contour plot of crack front displacement at different load stages (CT6). The dashed line: load step 26; dash-dot line: load step 250; long dashed line: load step 400; solid line: load step 500.

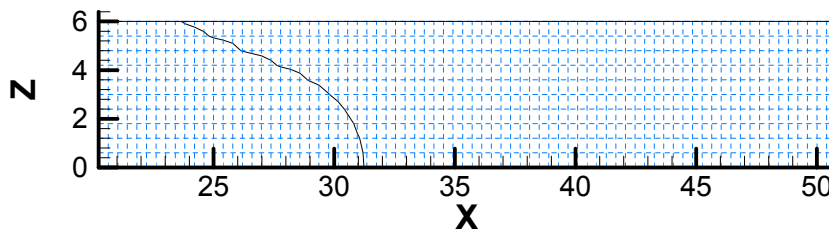


Fig.9-31 Contour plot of crack face displacement for a CT specimen with 12 mm thick (CT12). The line represents the front where the separation has occurred.

Fig. 9-32 shows the crack face profile for CT6 specimen, after 500 steps of loading. It is clear that near the crack tip the crack face is more curved while away from it, the face tends to flatten out, due to the release of plastic constraint by the surface layer of material. A similar profile was also observed for the CT12 specimen. Fig. 9-33 and Fig.9-34 show crack profiles (opening displacement) at a given external load and crack length for CT specimens with 6 and 12 mm thickness, respectively.

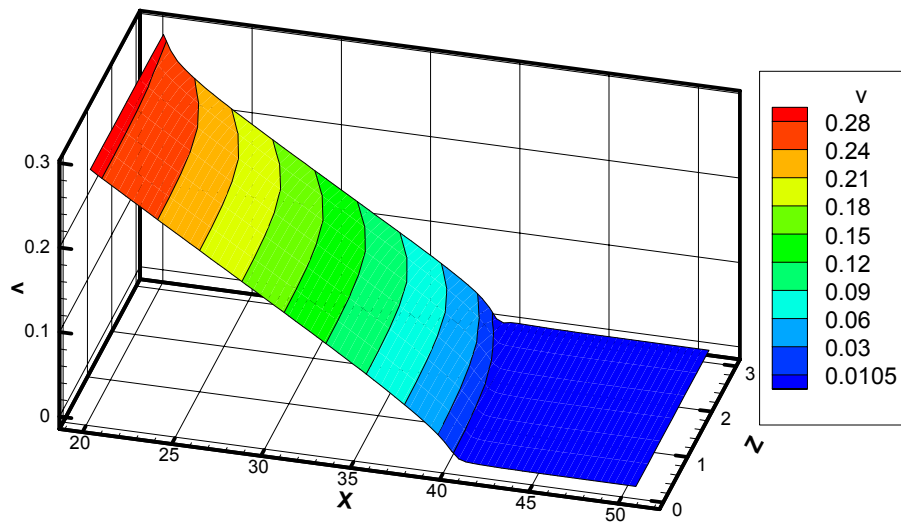


Fig. 9-32 Crack profile for CT6 specimen. The iso-displacement line 0.0105 indicates the current crack front when the crack extension is about 8 mm.

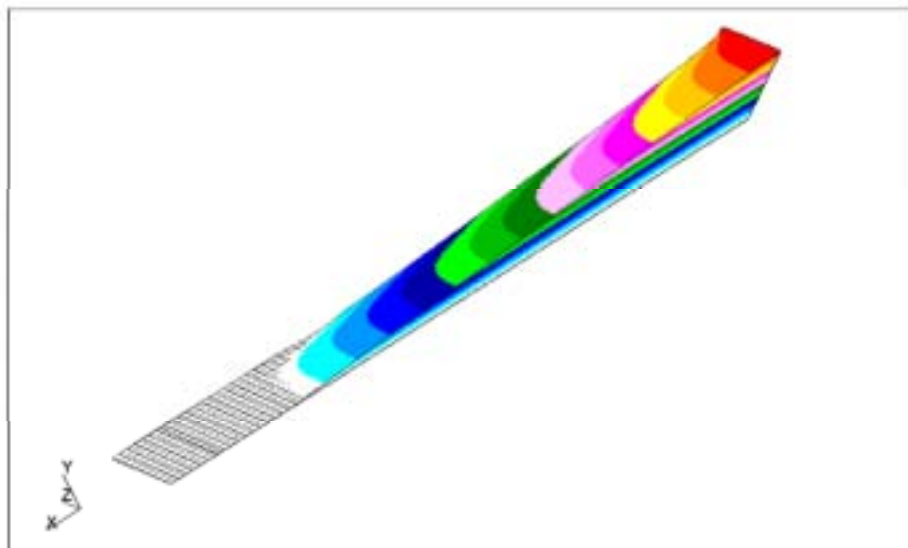


Fig. 9-33 Crack profile (opening displacement) at a given external load and crack length (CT specimen with 6 mm thickness-CT6).

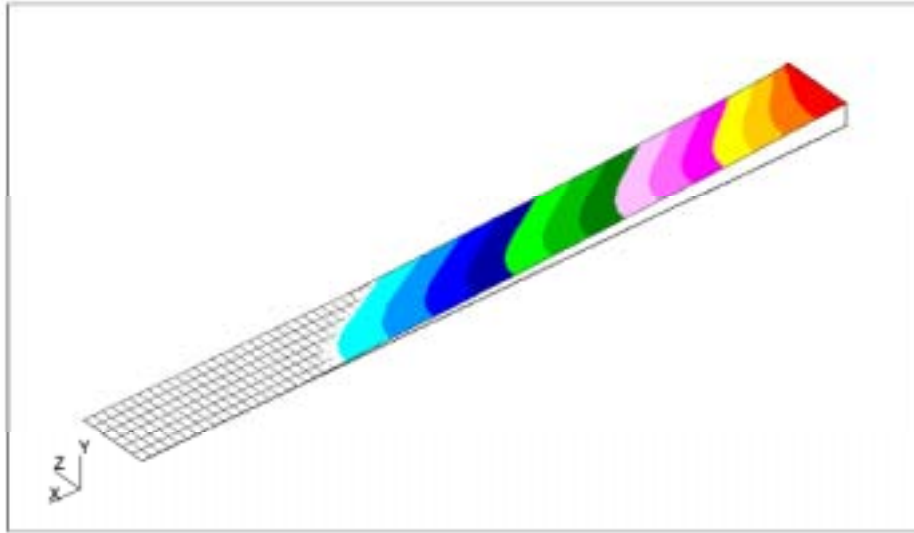


Fig. 9-34 Crack profile (opening displacement) at a given external load and crack length (CT specimen with 12 mm thickness-CT12)

10. Discussions

10.1 Simulation of Stable Tearing

As stated in Sec.9.1, at different levels of applied loads a variety of specific cases under pure plane strain, plane stress and intermediate conditions were investigated. The numerical results show that crack front profiles under plane strain condition were successfully reproduced using ZENCRACK. The general agreement between the numerical and observed experimental results was reached (Refer to Fig.3-5 and Fig.9-5). But it should be pointed out that the agreement is only qualitative.

The crack front profiles were produced for representative plane stress and intermediate stress state. These profiles reasonably agree with experimental observation from CT specimens (refer to Fig.3-4, Fig.9-7 and Fig.9-8). Profiles generated by ZENCRACK under these conditions were similar in shape to those experiencing plane stress caused by a reduction in specimen width. In ZENCRACK, only phase two of the crack growth is modelled (Paris equation). ZENCRACK does not model crack growth above or below this region. Any crack growth rates occurring outside the bound of the Paris region will be extrapolated from the given data by ZENCRACK. As a result, the total crack growth values may not be accurate. In addition, the large distortion often

observed in crack front profile under plane stress and intermediate loading were not reproduced by ZENCRACK.

Stable tearing could be simulated approximately using ZENCRACK, provided careful control was exerted over the whole process of modelling. Stable tearing was produced by a single overload following fatigue crack growth. In other words, reliable application of ZENCRACK would require that the fatigue crack growth fall within the bounds of the Paris equation. Secondly, the single overload stage should ideally be a separate static analysis and not a fatigue growth calculation – although fatigue growth can essentially be eliminated by careful choice of tolerances it is not strictly correct. The problem with a separate static analysis is that all previous crack front information must be input manually. This may be possible but time consuming. If these steps are followed the accuracy of the results may improve.

Two types of loads were used (Refer to Fig.9-4). However, ZENCRACK does not actually model a fatigue load spectrum. Although the user defines such a spectrum in the input file, the program averages the data. It uses the characteristic K method for fatigue crack growth predictions in linear elastic analyses – a relatively straightforward approach to crack growth prediction compared with other software. The characteristic K method predicts fatigue crack growth for constant amplitude loading with a short recurrence and assumes the crack will always grow through residual stresses induced by peak loads. The crack growth is subsequently assumed to be regular and is hence correlated to a characteristic K value said to be representative of the complete load history. This single K value therefore represents the entire spectrum, thus any effects caused by a variable loading are lost.

10.2 Effect of Crack Front Shape

The FE results show that when a crack front is curved, the SIFs at the surfaces are higher than those at the interior, compared to the straight crack front (i.e., 0% curvature), regardless of specimen thickness and geometry (CT or CCT). Compared to a straight crack front, there is a sharp corner near the specimen surfaces, i.e., a crack intersects a free surface, where high SIF exists, see Fig.6-5. As a result, a high opening stress occurs near the surface, leading to a high SIF.

Normally, after a tear band has formed, the fatigue crack grows faster at the surfaces than in the centre, until the crack front is almost straight. For example, in a CT specimen of 6 mm thickness, a crack growth starts with 43.66% curvature. After about 6.25 mm crack extension, the shape of the crack front approaches that of a straight crack, as shown in Fig.10-1.

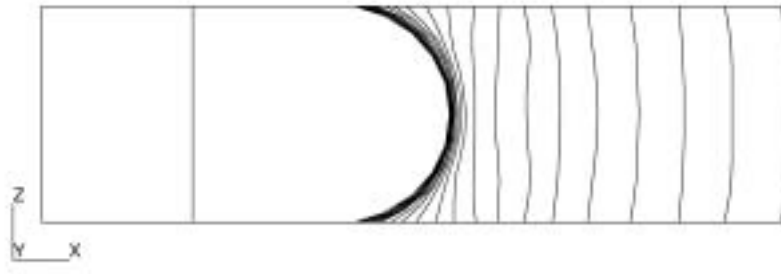


Fig.10-1 Change of crack front during crack propagation, which starts from 43.66% curvature in a CT specimen with 6 mm thick.

The key question is then what are the conditions when tearing starts and ends. It is assumed that the onset of stable tearing is due to an overload, i.e., the fatigue-to-tearing transition. This process can be briefly described in Fig.10-2. When the SIF at a point on the crack front, for example, at point B, reaches the critical value (K_{Ic}), the crack starts to jump. If SIF remains higher than the critical value during overload, the stable tearing will continue until the SIF value falls below the critical value, for example, at point A. The length of stable tearing or "jump" is determined by the SIF and specimen thickness during the overload for a given material.

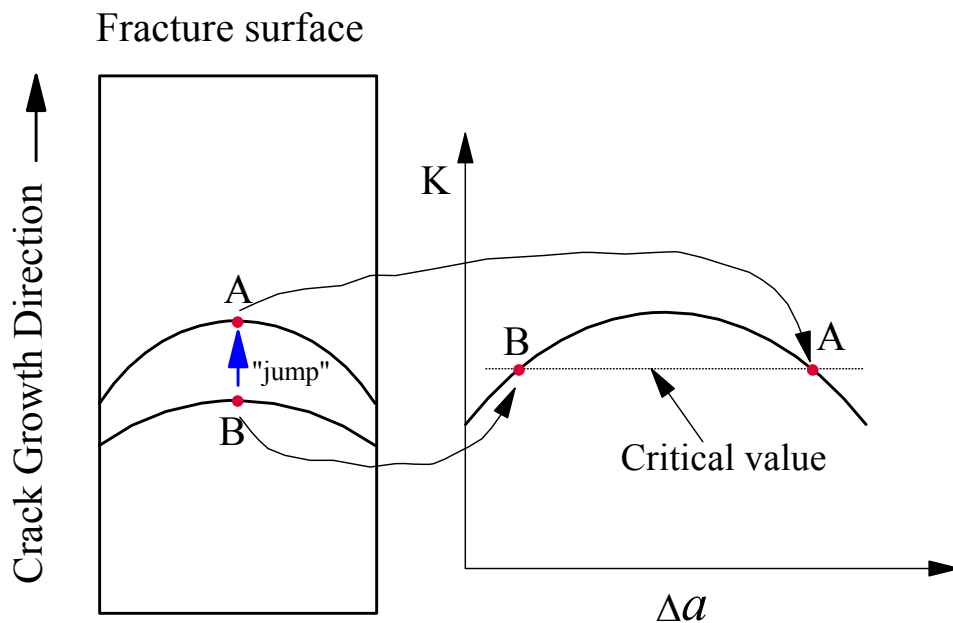


Fig.10-2 Schematic of relationship between crack front position at a mid-section and stress intensity factor, K .

The main features of CCT specimens are similar to those of CT specimens, except that there exists a U-shape in the SIF distribution at the middle part of the specimen. It may be related to the lower constraint in a CCT specimen, compared to a CT specimen.

10.3 Stress Distributions Along Crack Tip Front

Although ZENCRACK has the above limitations, it is useful for developing cracked finite element models of complex 3D shapes (Timbrell & Cook, 1997; Browning, et al, 2001; Hou, et al, 2001). The concept of crack blocks, which allow the user to control mesh density and distribution, makes this program applicable to any cracked structure in principle.

10.4 Applications of Cohesive Zone Model (CZM)

The stable tearing of aluminium plate was studied using the cohesive zone approach. The numerical results show that with the appropriate model parameters, the cohesive zone approach was able to qualitatively predict the shape of the crack front and the crack face profile. The predicted tunnelling effect correlates qualitatively with the published experimental data. Further experimental work needs to be carried out to validate the model prediction. The plastic dissipation rate demonstrates a steady state after the initial increment, and this information may be useful for the development of a tool to predict the occasional tearing that occurs in aircraft structures under fatigue loading. Further work needs to be done under cyclic loading condition.

10.5 Experiments from CCT Specimen Testing

The experiments on CCT specimens at CEAT showed the capability of the R-curve concept in predicting crack tearing propagation Δa_{phys} and the stress intensity (K_{final}), which causes stable tearing. But the accuracy relies on an R-curve (same material and thickness) and a specific correction factor, dependent on the thickness and the material (refer to Sec.6.1). So, this model cannot be readily used as a predictive model, but it can be effectively used for post fracture analyses.

11. Concluding Remarks and Recommendations

Stable tearing during fatigue is an important feature of crack growth and by nature a three-dimensional problem. However, because of the difficult theoretical nature of stable tearing (i.e. “crack jump”), the FE modelling work is complex. Based on numerical results using ZENCRACK coupled with ABAQUS packages and by the cohesive zone model, the following conclusions can be drawn.

(1) Stable tearing was successfully reproduced on a CCT specimen with different specimen thickness by experiments.

(2) ZENCRACK could be used to simulate 3-D crack behaviour. However, ZENCRACK can only be used to implement crack growth based on the linear region of the Paris equation. So ZENCRACK is useful for qualitatively investigating crack front behaviour under cyclic fatigue conditions for plane strain. But it could not be used to predict whether stable tearing would occur or arrest under cyclic loading due to lack of appropriate local failure criteria.

(3) Crack front profiles under plane stress and mixed loading were successfully produced. The numerical results agreed reasonably well with experimental observation. However, large growth is limited by both the application of the Paris equation and the ability of ABAQUS to distort the mesh. Therefore, large distortions, often observed in crack front profile under plane stress and intermediate stress state, were not reproduced by ZENCRACK. Reducing specimen width did not help capture this effect. ZENCRACK therefore appears to be useful for modeling such phenomena for indicative purposes only.

(4) The phenomenon of stable tearing was also modelled using ZENCRACK. Although careful control over the analysis was required it was possible to emulate the behaviour of materials undergoing crack jumping due to an excessive single load. However, the crack growth recorded for the test was outside of the region governed by the Paris equation, and the extrapolation applied severely affects the accuracy of the results.

(5) Fatigue crack growth for a variable load spectrum is not accurately modeled due to the implementation of the characteristic K method, which effectively averages the fatigue load spectrum.

(6) The SIF results along a crack front using ZENCRACK for the cracks with a curvature are reasonably consistent with the expected results based upon observation of fatigue crack growth following tearing fracture.

(7) The shape of the SIF distributions for a similar curvature showed similarities between the CT and CCT specimens. The W shaped SIF distribution was common for

a number of specimens, while the two specimens with the highest curvature for the CT and CCT specimens displayed U shape SIF distributions.

(8) The FE results using ZENCRACK coupled with ABAQUS package show that the crack shape has a great influence on SIF distribution. The SIFs near free surfaces increased with increased crack curvature but remain almost constant at the mid-section, except for the 6 mm CT specimen. The FE results also demonstrate that the onset and the end of the stable tearing behaviour are closely related to the change of the crack front shape. However, due to the lack of a suitable criterion for the problem of stable tearing, ZENCRACK cannot simulate a whole stable tearing process, i.e., from the onset (onset of “crack jump”) to the end of the tear. Therefore, more research is needed.

(9) Crack closure cannot be modelled using ZENCRACK – again this limitation affects the applied load spectrum. Therefore, the spectrum has not only been averaged but also truncated to above zero.

(10) A new 3D model using cohesive zone model (CZM) was established. The numerical results show that with the appropriate model parameters, the cohesive zone approach was able to qualitatively predict the shape of the crack front and the crack face profile. The predicted stable tearing-like (e.g., tunnelling) effect correlates qualitatively with the published experimental data.

(11) The results, obtained by the tearing models of Forsyth and Schijve on CCT specimens, confirm previous DSTO results on CT specimens, i.e., they are good predictors of the stress intensity K_{final} but only valid for the post fracture analysis.

(12) The R-Curve method is a viable alternative to Schijve’s model for post failure analyses only.

In future, more research will be carried out to explore the capability of ZENCRACK or other FE packages to establish an appropriate model. In addition, to develop a predictive capability of stable tearing behaviour the appropriate model with local criteria for stable tearing is obviously the key.

The cohesive zone approach implemented in WARP 3D package is promising and the results are encouraging. In future, more experimental work needs to be carried out to validate the model’s prediction. A model under cyclic loading condition for stable tearing needs to be developed.

12. Acknowledgments

The authors would like to thank Mr. M.W. Goldstraw and Mr. M. Stoessiger from Aerostructure Technologies Pty Ltd for some numerical work. The authors also express thanks Mr. B. Donis for conducting fatigue testing of CCT specimens at CEAT.

13. References

ABAQUS Version 6.3, Hibbitt, Karlsson & Sorensen, Inc, 2002.

ASTM E399-90, Standard Test Method for Plane-Strain Fracture Toughness of Metallic Materials, Annual Book of ASTM Standards, Vol.03.01, 2002, The American Society of Testing Materials.

ASTM E647-00, Standard Test Method for Measurement of Fatigue Crack Growth Rates, Annual Book of ASTM Standards, Vol.03.01, 2002, The American Society of Testing Materials.

Athinotis, N., Barter, S.A. and Clark, G., Summary of fatigue cracking in RAAF Macchi MB326H wing spars, DSTO Technical Report, DSTO-TR-0757, 1999, Limited release, Defence Science and Technology Organisation, Australia.

Australian and French Technical Agreement on TA4/00, Modelling of Stable Tearing in Fatigue Crack Growth, Aug. 2000. The final approval was Aug.2003.

Barenblatt, G, The mathematical theory of equilibrium cracks in brittle fracture, Advances in Applied Mechanics, Vol.7, pp.55-129, 1962.

Barter, S.A., Callinan, R.J. and Keppert, J., Investigation of the accident to Macchi MB326H A7-076, DSTO AMRL, Applied Technical Memorandum 035, Restricted released, May 1991.

Bowen, A. W. and Forsyth, P. J. E., On the Mechanism of Mixed Fatigue-Tensile Crack Growth, Mat. Sci. and Engng., Vol.49, pp. 141-154, 1981.

Browning, B., Cook, G. and Timbrell, C., Predicting large scale crack growth in 3D finite element methods, ABAQUS Users' Conference, Maastricht, The Netherlands, May 30-June 1, 2001.

Byrnes, R., Sharp, K.S., Goldsmith, N. and Clark, G., Modelling of stable tearing during fatigue of 7050 aluminium alloy, DSTO Report, DSTO-TR-1032, 2000, Defence Science and Technology Organisation, Australia.

Camacho, G. T., and Ortiz, M., Computational modelling of impact damage in brittle materials, *International journal of solids and structures*, Vol. 33, 2899-2938, 1996.

Dugdale, D.S., Yielding of steel sheet containing slits, *J. Mech. Phys. Solids*, Vol.8, pp.100-104, 1960.

Forsyth, P. J. E., Some Observations and Measurements on Mixed Fatigue/Tensile Crack Growth in Aluminium Alloys, *Scr. Metall.*, Vol.10, pp. 383-386, 1976.

Fühling, H., and Seeger, T., Dugdale crack closure analysis of fatigue cracks under constant amplitude loading, *Engineer Fracture Mechanics*, Vol.11, pp.99-172, 1979.

Goldsmith, N. T., Clarke, G., and Barter, S. A., A growth model for catastrophic cracking in an RAAF aircraft, *Engineering Failure Analysis*, Vol.3, pp.191-201, 1996.

Goldstraw, M.W., Investigation of the 3D crack modelling capability of ZENCRACK and ABAQUS, *AeroStructures Report*, 1999.

Gullerud, A.S., Koppenhoefer, K.C., Roy, A., Chowdhury, S., Walters, M. and Dodds, R.H., Jr., WARP3D-Release 14.1: 3-D Dynamic Nonlinear Fracture Analysis of Solids Using Parallel Computers and Workstations, *Structural Research Series (SRS) No 607*, UILU-ENG-95-2012, University of Illinois at Urbana-Champaign, April 2003.

Gurson, A.L., Continuum theories of ductile rupture by void nucleation and growth: Part I – yield criteria and flow rules for porous ductile media, *J. Engg. Mater. Tech.*, Vol.99, pp.2-15, 1977.

Hamel, P, Etude et modélisation de sauts statiques lors de la propagation de fissures dans un alliage d'aluminium 7050, internal CEAT report n°S-00/5969000-A, 2004.

Hou, J., Goldstraw, M., Maan, S. and Knop, M., An evaluation of 3D crack growth using ZENCRACK, *DSTO Technical Report*, DSTO-TR-1158, 2001, Defence Science and Technology Organisation, Australia.

Hu, W.P., Wang, C.H. and Barter, S.A., Analysis of cyclic mean stress relaxation and strain ratchetting behaviour of aluminium 7050, *DSTO Research Report*, DSTO-RR-0153, 1999, Defence Science and Technology Organisation, Australia.

Hu, W.P. and Liu, Q., Modelling of stable tearing of 7050-T7451 plate using a cohesive zone approach, *Worley Australasian Finite Element Conference*, Melbourne, 23-26 September, 2003.

Koppenhoefer, K.C., Gullerud, A.S., Ruggieri, C. and Dodds, R.H., Jr., WARP3D: Dynamic nonlinear analysis of solids using a preconditioned conjugate gradient

software architecture, Structural Research Series (SRS) 596, UILU-ENG-94-2017, University of Illinois at Urbana-Champaign, 1994.

Liu, Q. and Tran, D., Modelling of stable tearing in a CT specimen, unpublished report, 2001.

Military Handbook, Metallic Materials and Elements for Aerospace Vehicle Structures, MIL-HDBK-5H, 1 Dec. 1998, Department of Defense, USA.

Needleman, A., A continuum model for void nucleation by inclusion debonding, J. Appl. Mech., Vol.54, pp.525-531, 1987.

Needleman, A., An analysis of decohesion along an imperfect interface, Inter. J. Fracture, Vol.42, pp.21-40, 1990.

Ortiz, M., and Pandolfi, A., A finite deformation irreversible cohesive elements for three-dimensional crack propagation analysis, Int. J. Numer. Methods Eng., Vol.44, 1267-1282, 1999.

Schwable, K.-H. and Cornec, A., Modelling crack growth using local process zones, Technical Report, GKSS Research Center, Geesthacht, Germany, 1994.

Stoessiger, M., CT and CCT crack front stress intensity factor investigation using ZenCrack, AeroStructures Report, ER-FEA-51-APM168, Dec. 2002.

Timbrell, C. and Cook, G., 3D FE fracture mechanics analysis for industrial applications, Seminar on Inelastic Finite Element Analysis, Institute of Mechanical Engineers, London, Oct 14, 1997.

Tvergaard, V., Material failure by void growth to coalescence, Advances in Applied Mechanics, Vol.27, pp. 83-151, 1990, Academic Press.

Tvergaard, V. and Hutchinson, J.W., The relation between crack growth resistance and fracture process parameters in elastic-plastic solids, J. Mech. Phys. Solids, Vol.40, pp.1377-1397. 1992.

Vlasveld, J. A. and Schijve, J., "Tongue-Shaped Crack Extension During Fatigue of High Strength Aluminium Alloys", Department of Aerospace Engineering, Delft University of Technology, Report No. LR-279, April 1979.

ZENCRACK User Manual – Issue 6, December 1998, Zentech International Ltd.

ZENCRACK User manual for ZenCrack 7.0 – Issue 7, July 2002, Zentech International Ltd.

DISTRIBUTION LIST

Modelling of Stable Tearing in Aircraft Structures

Q. Liu, P. Hamel, W. Hu, P.K. Sharp, A. Lahousse and G. Clark

AUSTRALIA

DEFENCE ORGANISATION

No. of copies

Task Sponsor

S&T Program

Chief Defence Scientist	}	Shared
FAS Science Policy		
AS Science Corporate Management		
Director General Science Policy Development		
Counsellor Defence Science, London		Doc Data Sheet
Counsellor Defence Science, Washington		Doc Data Sheet
Scientific Adviser to MRDC, Thailand		Doc Data Sheet
Scientific Adviser Joint		1
Navy Scientific Adviser		Doc Data Sht & Dist List
Scientific Adviser – Army		Doc Data Sht & Dist List
Air Force Scientific Adviser		1
Scientific Adviser to the DMO M&A		Doc Data Sht & Dist List
Scientific Adviser to the DMO ELL		Doc Data Sht & Dist List

Platforms Sciences Laboratory

Director of PSL (Corporate Leader Air)	Doc Data Sht & Exec Summ
Chief of Air Vehicles Division	Doc Data Sht & Dist List
Research Leader: AVD RL-AM	Doc Data Sht & Dist List
Head: L. Davidson	1
Task Manager	1
Q. Liu	2
P. Hamel	1
W. Hu	1
P.K. Sharp	1
A. Lahousse	1
G. Clark	1

DSTO Library and Archives

Library Fishermans Bend	Doc Data Sheet
Library Edinburgh	1
Defence Archives	1

Capability Development Group

Director General Maritime Development	Doc Data Sheet
Director General Land Development	Doc Data Sheet
Director General Capability and Plans	Doc Data Sheet
Assistant Secretary Investment Analysis	Doc Data Sheet
Director Capability Plans and Programming	Doc Data Sheet
Director Trials	Doc Data Sheet

Chief Information Officer Group

Deputy CIO	Doc Data Sheet
Director General Information Policy and Plans	Doc Data Sheet
AS Information Strategy and Futures	Doc Data Sheet
AS Information Architecture and Management	Doc Data Sheet
Director General Australian Defence Simulation Office	Doc Data Sheet
Director General Information Services	Doc Data Sheet

Strategy Group

Director General Military Strategy	Doc Data Sheet
Director General Preparedness (delete "Doc Data Sheet" if a copy should be sent)	Doc Data Sheet
Assistant Secretary Governance and Counter-Proliferation	Doc Data Sheet

Air Force

SO (Science) - Headquarters Air Combat Group, RAAF Base, Williamtown NSW 2314	Doc Data Sht & Exec Summ
---	--------------------------

Army

ABCA National Standardisation Officer

Land Warfare Development Sector, Puckapunyal	e-mailed Doc Data Sheet
SO (Science) - Land Headquarters (LHQ), Victoria Barracks NSW	Doc Data & Exec Summary
SO (Science), Deployable Joint Force Headquarters (DJFHQ) (L), Enoggera QLD	Doc Data Sheet

Joint Operations Command

Director General Joint Operations	Doc Data Sheet
Chief of Staff Headquarters Joint Operations Command	Doc Data Sheet
Commandant ADF Warfare Centre	Doc Data Sheet
Director General Strategic Logistics	Doc Data Sheet

Intelligence and Security Group

DGSTA Defence Intelligence Organisation	1
Manager, Information Centre, Defence Intelligence Organisation	1 (PDF)
Assistant Secretary Capability Provisioning	Doc Data Sheet
Assistant Secretary Capability and Systems	Doc Data Sheet
Assistant Secretary Corporate, Defence Imagery and Geospatial Organisation	Doc Data Sheet

Defence Materiel Organisation

Deputy CEO	Doc Data Sheet
Head Aerospace Systems Division	Doc Data Sheet

Head Maritime Systems Division	Doc Data Sheet
Chief Joint Logistics Command	Doc Data Sheet

Defence Libraries

Library Manager, DLS-Canberra	Doc Data Sheet
-------------------------------	----------------

OTHER ORGANISATIONS

National Library of Australia	1
NASA (Canberra)	Doc Data Sheet
Library of New South Wales	Doc Data Sheet
State Library of South Australia	Doc Data Sheet

UNIVERSITIES AND COLLEGES

Australian Defence Force Academy

Library	1
Head of Aerospace and Mechanical Engineering	Doc Data Sheet
Serials Section (M list), Deakin University Library, Geelong, VIC	Doc Data Sheet
Hargrave Library, Monash University	Doc Data Sheet
Librarian, Flinders University	Doc Data Sheet

OUTSIDE AUSTRALIA

SPAe\ST\CEA\SM

Eric Pellegrini	1
-----------------	---

INTERNATIONAL DEFENCE INFORMATION CENTRES

US Defense Technical Information Center	1
UK Dstl Knowledge Services	1
Canada Defence Research Directorate R&D Knowledge & Information Management (DRDKIM)	1
NZ Defence Information Centre	1

ABSTRACTING AND INFORMATION ORGANISATIONS

Library, Chemical Abstracts Reference Service	1
Engineering Societies Library, US	1
Materials Information, Cambridge Scientific Abstracts, US	1
Documents Librarian, The Center for Research Libraries, US	1

SPARES	5
--------	---

Total number of copies: 32 Printed: 31 PDF: 1

DEFENCE SCIENCE AND TECHNOLOGY ORGANISATION DOCUMENT CONTROL DATA					
				1. PRIVACY MARKING/CAVEAT (OF DOCUMENT)	
2. TITLE Modelling of Stable Tearing in Aircraft Structures			3. SECURITY CLASSIFICATION (FOR UNCLASSIFIED REPORTS THAT ARE LIMITED RELEASE USE (L) NEXT TO DOCUMENT CLASSIFICATION) <div> <div>Document</div> <div>(U)</div> </div> <div> <div>Title</div> <div>(U)</div> </div> <div> <div>Abstract</div> <div>(U)</div> </div>		
4. AUTHOR(S) Q. Liu, P. Hamel, W. Hu, P.K. Sharp, A. Lahousse and G. Clark			5. CORPORATE AUTHOR Platforms Sciences Laboratory 506 Lorimer St Fishermans Bend Victoria 3207 Australia		
6a. DSTO NUMBER DSTO-TR-1657		6b. AR NUMBER AR-013-350		6c. TYPE OF REPORT Technical Report	
7. DOCUMENT DATE March 2005					
8. FILE NUMBER 2005/1017344/1		9. TASK NUMBER AIR 03/120		10. TASK SPONSOR DGTA	
				11. NO. OF PAGES 84	
				12. NO. OF REFERENCES 35	
13. URL on the World Wide Web http://www.dsto.defence.gov.au/corporate/reports/DSTO-TR-1657.pdf				14. RELEASE AUTHORITY Chief, Air Vehicles Division	
15. SECONDARY RELEASE STATEMENT OF THIS DOCUMENT <div> <div>Approved for public release</div> </div>					
OVERSEAS ENQUIRIES OUTSIDE STATED LIMITATIONS SHOULD BE REFERRED THROUGH DOCUMENT EXCHANGE, PO BOX 1500, EDINBURGH, SA 5111					
16. DELIBERATE ANNOUNCEMENT No Limitations					
17. CITATION IN OTHER DOCUMENTS Yes					
18. DEFTEST DESCRIPTORS Aircraft structures, Fractures (materials), Tearing, Cracks, Numerical methods and procedures, Finite element analysis					
19. ABSTRACT This report summarises the cooperative research program on stable tearing between DSTO and CEAT. The main objective was to study the conditions under which aircraft materials fracture by stable tearing and to develop a predictive capability for the process under operational conditions. The experiments on both CCT and CT specimens were to assist in validation of numerical modelling. Tear bands were successfully reproduced on CCT specimens with different specimen thickness by experiments at CEAT. The results were used to assess empirical models – Schijve’s and Forsyth’s models, and R-curve methods as well. Stable tearing feature was successfully simulated by a commercial finite element package ZENCRACK. Due to lack of local failure criteria, ZENCRACK cannot be used to predict whether stable tearing would occur or arrest under cyclic loading. But it appears to be useful for modelling such phenomena for indicative purpose only. A new 3D numerical model was proposed using a cohesive zone approach. This model can predict features similar to stable tearing and agrees well with the published experimental data. However, more research work needs to be done.					